MECHANISMS OF MYOSIN-7B FUNCTION IN BRUSH BORDER ASSEMBLY

By

Meredith L. Weck

Dissertation

Submitted to the Faculty of the

Graduate School of Vanderbilt University

in partial fulfillment of the requirements

for the degree of

DOCTOR OF PHILOSOPHY

in

Cell and Developmental Biology

May 11, 2018

Nashville, Tennessee

Approved:

Robert J. Coffey, M.D.

Dylan T. Burnette, Ph.D.

Matthew J. Lang, Ph.D.

Ryoma Ohi, Ph.D.

Matthew J. Tyska, Ph.D

ACKNOWLEDGEMENTS

First and foremost, I would like to greatly thank my mentor, Dr. Matthew J. Tyska, for his support and guidance over the past five years. I am grateful for everything that he does for the lab to provide us with the resources we need. Matt is a tremendous teacher, and his passion and enthusiasm for science is contagious. It has been a privilege to have trained with such an amazing scientist and mentor, whom I deeply respect and admire.

I would like to thank my committee members, Drs. Bob Coffey, Dylan Burnette, Matt Lang, and Puck Ohi, for their advice and support through the years. I have to thank Dr. Chris Wright and the Program in Developmental Biology for providing an incredibly supportive and fun community for graduate students. Thank you to the Vanderbilt Microtubules and Motors Club and Epithelial Biology Center for thoughtful discussions. I would also like to acknowledge the Electron Microscopy Core and Nikon Center of Excellence for their assistance with experiments. Also, thank you to the CDB staff members who work thanklessly to help students in almost every way.

I am fortunate to have worked with amazing people over the years who I am honored to call my friends. I have to thank past lab members Scott, Nathan, David, and Jessi for recruiting me to the lab and encouraging me through my first couple years in the lab. I particularly need to thank Scott and Nathan for their advice and guidance. They were always willing to teach and help me whenever I needed it. I would like to thank current lab members Meagan, Bryan, Suli, Colbie, Julia, Bella, Leslie, Angelo, and Bo. They have all supported me through this journey and I look forward to seeing their future successes. I also must acknowledge my friends in the department and IGP program for helping to keep me sane through this crazy thing called grad school.

Finally, I must thank my family who has always been there for me. My sister and brother-in-law, Allyson and Stephen, have encouraged and helped me along the way. My parents, Candy and Phil, have been extremely supportive, understanding, and reassuring through this entire process. My boyfriend, Alex, has also supported and encouraged me these last two years of my graduate school career. I greatly appreciate everything they have done for me and cannot begin to express my gratitude.

TABLE OF CONTENTS

LIST OF FIGURES

LIST OF ABBREVIATIONS

^{o}C	degrees Celsius
Δ	delta, deletion
aa	amino acids
ADP	adenosine diphosphate
ALK6	activin receptor-like kinase 6
ANKS4B	ankyrin repeat and SAM domain-containing protein 4B
Anti-CC	anti-parallel coiled coil
ATP	adenosine triphosphate
BAPTA	1,2-bis(2-aminophenoxy)ethane-*N,N,N',N'*-tetraacetic acid
BB	brush border
BMP	bone morphogenetic protein
BSA	bovine serum albumin
Bt	*Bos taurus*
CACO-2_{BBE}	colonic adenocarcinoma cells 2 brush border expressing
CBC	crypt base columnar
CDH23	cadherin-23
CL4	LLC-PK1-CL4 cells
CO_2	carbon dioxide
CRISPR	clustered regularly interspaced short palindromic repeats
C-terminal	carboxy-terminal
DAPI	4',6-diamidino-2-phenylindole

DCC	deleted in colorectal carcinoma
Dd	*Dictyostelium discoideum*
DFNA11	autosomal dominant non-syndromic deafness
DFNB2	autosomal recessive non-syndromic deafness
DFNB3	autosomal recessive non-syndromic deafness
Dlg1	disc large homolog 1
DPC	days post confluency
EC	extracellular
EC	extracellular cadherin
EGFP	enhanced green fluorescent protein
EGTA	ethylene glycol-bis(2-aminoethylether)-*N,N,N',N'*-tetraacetic acid
Eps8	epidermal growth factor receptor pathway substrate 8
FERM	protein 4.1, ezrin, radixin, and moesin
FL	full-length
FRAP	fluorescence recovery after photobleaching
FRET	Förster resonance energy transfer
GAPDH	glyceraldehyde 3-phosphate dehydrogenase
GCN4	general control nonderepressible 4
Hs	*Homo sapiens*
HT	HaloTag
IC	intracellular
IMAC	intermicrovillar adhesion complex

IQs	IQ calmodulin- or light chain-binding motifs
I.U.	intensity units
KD	knockdown
kDa	kilodaltons
KO	knockout
LLC-PK1-CL4	Lilly Laboratories cell - porcine kidney - clone 4
L_{pi}	length at peak intensity
MD	motor domain
Mena	mammalian enabled
MET	mechanotransduction
MF	MyTH4-FERM
min	minute
MLPCDH/CDHR5	mucin-like protocadherin
Myo	myosin
MyRip	myosin-7a and Rab-interacting protein
MyTH4	myosin tail homology 4
N-cadherin	neural cadherin
NIH	National Institutes of Health
Norm.	normalized
N-terminal	amino-terminal
ON	overnight
PBS	phosphate buffered saline
PC	Paneth cells

PCDH24/CDHR2	protocadherin-24
PCDH15	protocadherin-15
PCR	polymerase chain reaction
PDZ	PSD95, Dlg1, ZO-1
PDZD7	PDZ domain containing protein 7
PEST	proline, glutamate, serine, threonine peptide sequence for protein degradation
PH	pleckstrin homology
PM	plasma membrane
PSD95	post synaptic density protein 95
RT	room temperature
SAH	single α-helix
SAM	sterile α-motif
SANS	scaffold protein containing ankyrin repeats and SAM domain/Usher syndrome type-1G protein
Scr	scramble
SD	standard deviation
sec	second
SEM	scanning electron microscopy
SH3	SRC homology 3
shRNA	short hairpin ribonucleic acid
t	time
TEM	transmission electron microscopy

TIRF	total internal reflection fluorescence
TMC	transmembrane channel-like
USH1B	Usher syndrome type-1B
USH1C	harmonin/Usher syndrome type-1C protein
VASP	vasodilator-stimulated phosphoprotein
VE-cadherin	vascular endothelial cadherin
WT	wild-type
ZO-1	zona occludens-1

CHAPTER I
INTRODUCTION

Myosin motor proteins

Myosins comprise a large superfamily of ATPases that interact with actin filaments to power motility or generate force for a broad range of subcellular applications. Myosins perform diverse functions with tissue and cell specific expression and activities. In general, myosins share three structural features that support their specific functions. On the N-terminus, they have a highly conserved motor (or head) domain, where ATP hydrolysis and actin binding occur. A defining characteristic of their ATPase activity is its activation by actin binding. Myosins contain a central neck region that binds one or more light chains and acts as a lever arm for force transduction. Light chain binding occurs through IQ motifs with a consensus sequence of IQXXXRGXXXRK (McNally et al., 1991; Mooseker and Cheney, 1995). Depending on the myosin, these motifs typically bind essential or regulatory light chains and calmodulin (CaM) or CaM-like molecules (Houdusse and Cohen, 1995). Many of these light chains are calcium sensitive and act as signaling molecules to stimulate myosin activity. Coiled coil domains that mediate dimerization are also found in this region. Finally, the C-terminal tail contains domains that mediate cargo interactions and, in some cases, auto-inhibition. These domains often regulate the activity, localization, and function of the myosin by dictating which cargo molecules it can bind.

The myosin superfamily is separated into 35 classes, each consisting of multiple isoforms (Odronitz and Kollmar, 2007). This introduction will focus on a particular

subgroup of myosin classes called the MyTH4-FERM myosins, consisting of class 7, 10 and 15. First, we will discuss the actin cytoskeleton, the track for myosin motors, and its role in controlling cell shape. Here, we will introduce actin-based finger-like protrusions and how they support cell and tissue function. We will then discuss one type of protrusion, the microvillus, in more detail, focusing on its role in the intestinal brush border. This will lead us into brush border formation during cell differentiation and proteins that promote this process. Next, we will introduce the different myosins found in the brush border and what is known about their functions. Finally, we will focus on MyTH4-FERM mysoins and review data from biophysical, biochemical, and cell biological studies, which implicate these myosins as central players in the assembly, maintenance and function of actin-based protrusions. The goal of this introduction is to provide context for how our studies on myosin-7b (Myo7b), a MyTH4-FERM myosin, have contributed to the myosin motor and actin cytoskeleton fields, and advanced our understanding of brush border assembly.

Actin-based finger-like membrane protrusions

The physiological role of a differentiated cell is dictated in large part by its morphology, which in turn is controlled by the cytoskeleton. Although actin, microtubule, and intermediate filament networks each contribute to global cell shape control, this introduction will focus on how cells employ the actin cytoskeleton and its associated motor proteins to create fine surface features, specifically the finger-like protrusions that enable biochemical and physical interactions with the external environment. Three general classes of such protrusions exist: filopodia, microvilli, and stereocilia (Figure 1-

1). We use the word ‘protrusion’ herein to refer specifically to these finger-like features. These protrusions will be reviewed in the following sections.

The structures of the finger-like protrusions are supported by a core bundle of actin filaments. These filaments are all oriented in the same direction with their fast-growing plus-ends, also referred to as barbed ends, at the distal tips. This generates a parallel actin bundle that is ideal to serve as a track for myosins, as all known motors are unidirectional and can only walk towards one end, either plus or minus depending on the motor. Despite this similarity, how each protrusion is built and maintained varies greatly. For instance, the lifetimes of each structure are vastly different with filopodia being regenerated within minutes, microvilli maintained for the lifetime of the cell (usually days), and stereocilia preserved for the entire lifespan of the organism. Therefore, the proteins involved in filament nucleation, elongation, bundling, and turnover, and their regulation are highly specific to each structure.

Although significant distinctions between filopodia, microvilli, and stereocilia can be made in terms of the density of the protrusions (i.e. number of structures per cell), the shape of the supporting actin bundle (i.e. length, number of bundled filaments), and its mode of anchoring in the cell, these three systems also share some common features. For example, in each case a parallel bundle of actin filaments provides the mechanical rigidity needed for membrane deformation and protrusion. Additionally, all of these structures localize adhesion factors to their distal tips, allowing them to make physical attachments with either the substrate (as is the case of filopodia) or with adjacent protrusions (as is the case for stereocilia and microvilli); such attachments are critical for the organization of these structures. Another theme common to all three

classes, which is the focus of this introduction, is the use of actin-based motors, i.e. myosins, for their formation, maintenance, and function. These characteristics will be discussed in further detail.

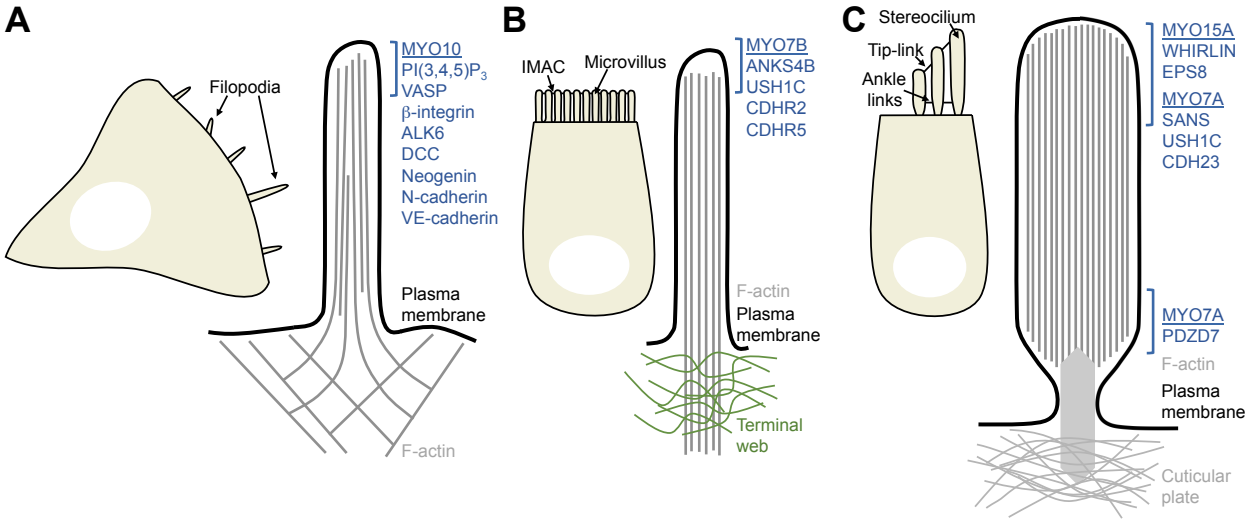

Figure 1-1. Actin-based, finger-like membrane protrusions. **(A)** filopodia, **(B)** microvilli, and **(C)** stereocilia. The relevant MyTH4-FERM myosins and their cargoes are listed in each case.

Filopodia

Filopodia are highly dynamic and typically substrate-attached features that form on the ventral/basolateral cell surface of migrating cells (Figure 1-1 A). They function in detecting and responding to environmental cues, both physical and chemical. These protrusions can reach up to 10 microns in length and are comprised of 10-30 bundled actin filaments (Mogilner and Rubinstein, 2005; Svitkina et al., 2003). Filopodia formation has been proposed to occur by two different but not mutually exclusive mechanisms: convergent elongation and tip nucleation. The convergent elongation model suggests filopodia are formed by the reorganization of the branched actin network in the lamellipodium, formed by the Arp2/3 complex (Svitkina et al., 2003; Yang

and Svitkina, 2011). This reorganization is mainly driven by elongation factors, such as formins and Ena/VASP, which act to protect actin filaments from capping and cluster filament ends (Applewhite et al., 2007; Hansen and Mullins, 2010; Lebrand et al., 2004; Pellegrin and Mellor, 2005; Schirenbeck et al., 2005a; Schirenbeck et al., 2005b). In contrast, the tip nucleation model suggests that filopodial initiation occurs through the clustering of formins on the plasma membrane, leading to filament nucleation and elongation (Schirenbeck et al., 2005b). In both models, fascin plays an important role in crosslinking the newly made bundle to enable protrusion formation (Vignjevic et al., 2006). Additionally, actin monomer incorporation occurs at the tips with treadmilling through the filopodial bundle occurring at a rate of a few microns per minute (Mallavarapu and Mitchison, 1999).

Stereocilia

Stereocilia are microvillus-derived features found on the surface of sensory epithelial cells in the cochlear and vestibular systems (Figure 1-1 C). They are organized into rows of graded height known as ‘hair bundles’ and play a direct role in the mechanotransduction process responsible for hearing and balance. These protrusions have a tapered base that creates the flexural rigidity required for deflection of the hair bundle and its role in mechanotransduction. Unlike the other actin-based protrusions discussed here, stereocilia vary greatly in length, ranging from 1 to 100 microns, depending on the location within the inner ear (Prost et al., 2007). Due to their increased length, stereocilia bundles are composed of hundreds of actin filaments. To anchor these structures in the cell, the base of the actin bundle is embedded in the

cuticular plate, a dense meshwork of actin filaments and crosslinkers. Proteins involved in crosslinking actin filaments within the cuticular plate include tropomyosin, α-actinin, and XIRP2 (Francis et al., 2015; Scheffer et al., 2015; Slepecky and Chamberlain, 1985). Additionally, Myo6 has been suggested to link the proteins in the plasma membrane to the cuticular plate at the base of stereocilia (Self et al., 1999), and ACF7 connects the actin and microtubule cytoskeletons (Antonellis et al., 2014).

Detailed analyses of hair cell differentiation showed that stereocilia actin bundles go through distinct phases of widening and elongation (Tilney et al., 1992; Tilney and DeRosier, 1986; Tilney et al., 1983; Tilney and Saunders, 1983; Tilney et al., 1988; Tilney et al., 1986). Several bundling proteins have been shown to regulate the elongation (EPS8 and epsin-1) and maintenance (fascin-2 and fimbrin) of normal stereocilia height and width (Chou et al., 2011; Manor et al., 2011; Perrin et al., 2013; Salles et al., 2009; Shin et al., 2010; Taylor et al., 2015; Zampini et al., 2011). Additionally, the proteins taperin, TRIOBP, and Fam65b play specific roles in tapering the actin core at the base of stereocilia (Kitajiri et al., 2010; Zhao et al., 2016). However, nucleators that would be responsible for initiating actin filament growth have yet to be identified.

Initial reports suggested that stereocilia actin bundles undergo continuous turnover (Rzadzinska et al., 2004; Schneider et al., 2002). However, subsequent studies have demonstrated that stereocilia actin cores are stable, incorporating actin only at the distal tip (Drummond et al., 2015; Narayanan et al., 2015). This model supports the idea of a dynamic but limited zone of protein turnover, requiring the presence of molecules that block actin monomer dissociation from both the plus- and minus-ends. Indeed, actin

capping proteins twinfilin-2, gelsolin, and heterodimeric capping protein (CAPZ) localize to stereocilia tips and restrict the length (Avenarius et al., 2017; Mburu et al., 2010; Peng et al., 2009).

Mechanotransduction results when deflections of the hair bundles put tension on a structure known as the 'tip-link', which physically connects the tip of one stereocilium to the side of its taller neighbor (Assad et al., 1991; Kachar et al., 2000; Pickles et al., 1984; Zhao et al., 1996). Tip-links are *trans* heterophilic complexes composed of cadherin-23 (CDH23) and protocadherin-15 (PCDH15) (Kazmierczak et al., 2007). PCDH15 localizes to the lower tip-link where it interacts with TMC1 and TMC2, which have been implicated as components of the mechanotransduction (MET) channel (Beurg et al., 2015; Kazmierczak et al., 2007; Kurima et al., 2015; Maeda et al., 2014; Pan et al., 2013). CDH23 localizes to the upper portion of the tip-link (Kazmierczak et al., 2007). Other components of the upper tip-link density include USH1C, SANS, and Myo7a where they form a complex that is thought to maintain tension on the tip-link (Grati and Kachar, 2011). Loss-of-function mutations in any of the tip-link components causes type-1 Usher-syndrome, a major form of inherited deaf-blindness (Bitner-Glindzicz et al., 2000; Bolz et al., 2001; Bork et al., 2001; Riazuddin et al., 2012; Verpy et al., 2000; Weil et al., 1995; Weil et al., 2003).

Microvilli

Microvilli are found on the apical surface of diverse epithelia, where they function to increase membrane area and thus, solute transport capacity (Figure 1-1 B). These protrusions are typically found in great numbers and are packed into highly ordered

ensembles. They are relatively short, ranging from 0.5 to 3 microns depending on the cell and tissue. Microvillar cores are comprised of about 20-30 bundled filaments that are anchored in a dense subapical network of intermediate filaments called the terminal web (Hirokawa et al., 1982). Electron tomography studies have shown that there is a slight twist of the actin bundle, oriented in the clockwise direction when viewed from the top (Ohta et al., 2012). Within microvilli, actin filaments are bundled by villin (Bretscher and Weber, 1979), espin (Bartles et al., 1998), and fimbrin (Bretscher and Weber, 1980). Villin and espin localize throughout the microvillar actin bundle and have been suggested to induce and elongate microvilli, respectively (Franck et al., 1990; Loomis et al., 2003). In addition to bundling, fimbrin is enriched at the base of the brush border where it is thought to help stabilize microvilli by physically linking the actin bundle to cytokeratin filaments in the terminal web (Grimm-Gunter et al., 2009). However, other proteins are likely involved as loss of all three bundlers does not prevent the formation of microvilli, although they have reduced length and transverse area (Revenu et al., 2012).

Data from cultured cells suggest that microvillar actin filaments treadmill, turning over actin monomers by incorporating them at the tips and disassembling them at the base (Loomis et al., 2003; Tyska and Mooseker, 2002). However, actin dynamics and treadmilling *in vivo* have yet to be explored, and are currently ongoing in our laboratory. Despite these data, actin nucleators, elongation factors, and severing proteins in these protrusions have remained largely unexplored until recently. Papers from our laboratory and others show that a WH2 domain-containing protein, cordon bleu (COBL), along with the F-BAR domain-containing protein, syndapin-2, may initiate growth and regulate the

length of microvilli (Grega-Larson et al., 2015; Grega-Larson et al., 2016; Wayt and Bretscher, 2014). The most elaborate mirovillar structure in the human body is built by the intestinal tract, and is the model system our laboratory used to study microvilli. Details about intestinal structure and function will be introduced in the following sections.

Intestinal epithelium and brush border function

The intestine is the main site of nutrient absorption in the body. It also serves as the first line of defense against toxins and pathogens found in the lumen. The intestine is separated into two subdomains: villi and crypts of Lieberkühn (Figure 1-2). Villi are finger-like folds of tissue that project into the lumen and increase the surface area for nutrient absorption (Helander and Fandriks, 2014). They range in size from about 0.5 - 1 mm. Crypts are invaginations into the underlying submucosa that surround the base of each villus. They house and protect intestinal stem cells that undergo asymmetric division to replenish the epithelium. There are slow-cycling and quiescent stem cells that will proliferate following injury (Montgomery et al., 2011; Powell et al., 2012; Sangiorgi and Capecchi, 2008; Takeda et al., 2011). Additionally, there are highly proliferative stems cells known as the crypt base columnar (CBC) cells (Barker et al., 2007). Their daughter cells, referred to as transit amplifying cells, migrate up the crypt while undergoing more rounds of cell division and differentiation. Cells that emerge from the crypt are fully differentiated and continue migrating up the villus axis until they reach the top and are sloughed off into the lumen, about 3-5 days later. These cells mainly include goblet cells, enteroendocrine cells, and enterocytes. Goblet cells secrete mucins

that create a protective layer of mucus, which acts as a physical barrier against microbes. Enteroendocrine cells secrete hormones to regulate digestive function. Enterocytes make up the main population of intestinal epithelial cells, accounting for up to 95% of the villus cells. These are the only cells responsible for nutrient absorption. Additional cells present in the intestinal epithelium include tuft and M cells, both which function in the immune system. There is one additional fully differentiated cell type called Paneth cells. These cells remain in the base of the crypt where they function in secretion of defensins and other anti-microbial factors, and maintaining the stem cell niche through EGF, Notch, and Wnt signaling (Sato et al., 2011).

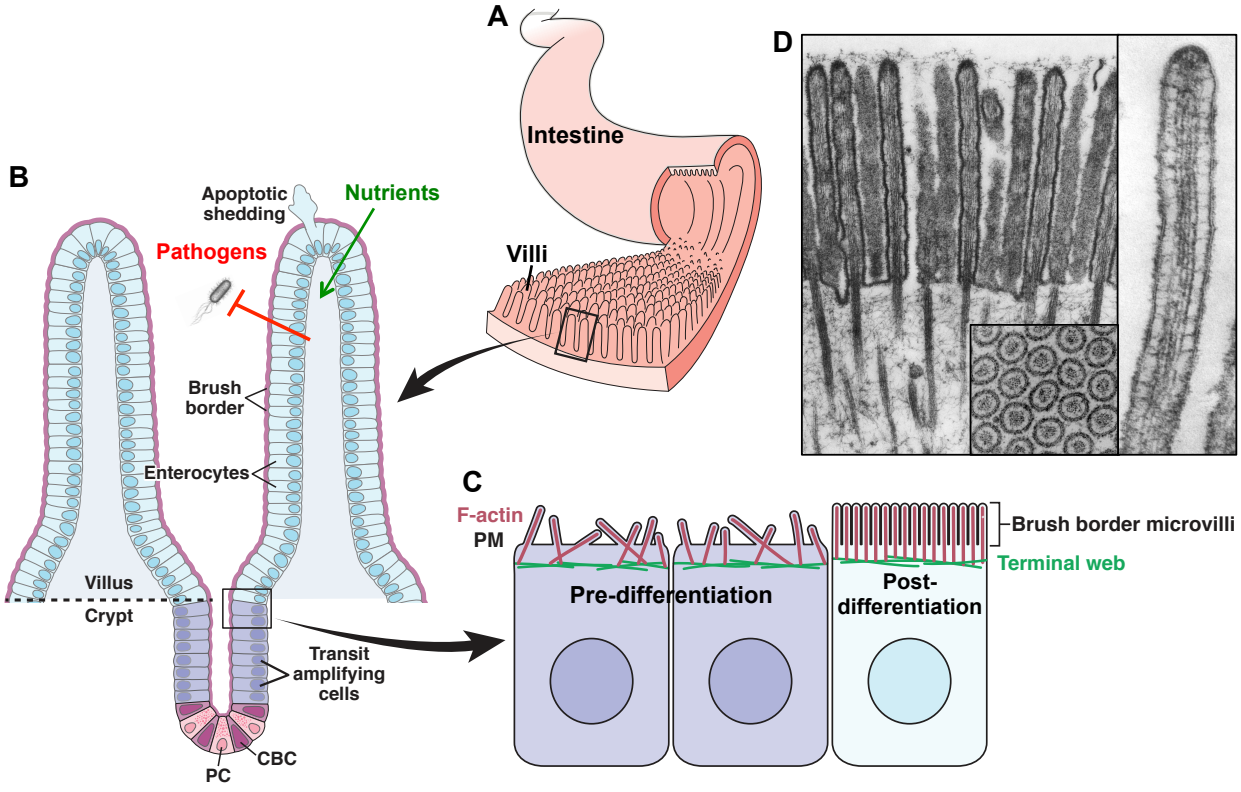

Figure 1-2. Architecture of the intestinal epithelium and brush border. Schematic representation of **(A)** the intestine and finger-like folds of tissue called villi, **(B)** a cross section through the intestinal epithelium along the crypt-villus axis, and **(C)** the differentiation of an enterocyte with the associated formation and organization of the brush border. Paneth cells (PC), crypt base columnar cells (CBC), plasma membrane

(PM). **(D)** Transmission electron micrographs of microvilli from chicken small intestine, originally published in (Mooseker and Tilney, 1975). Inset is a cross section to show the hexagonal packing. Zoom shows a single microvillus with the core actin bundle linked to the plasma membrane by lateral bridges and an electron dense plaque at the tip. Adapted from (Crawley et al., 2014a).

To aid in its function, enterocytes produce hundreds of microvilli on the apical surface of the cell to increase the absorptive capacity. These microvilli are tightly packed into hexagonal arrays, and are remarkably uniform in diameter (~100 nm) and length (~1-3 um depending on the place along the intestinal tract). Collectively, this structure is known as the brush border (BB). It is estimated that the brush border amplifies the surface area of the small intestine by 9-16-fold (Helander and Fandriks, 2014). This allows for the apical membrane of enterocytes to be highly enriched in transporters and enzymes required for nutrient uptake (Maroux et al., 1988). The brush border is also actively involved in host defenses against microbes. Microvilli shed microvesicles from their tips into the lumen (McConnell et al., 2009). These vesicles contain anti-microbial molecules including the enzyme intestinal alkaline phosphatase that inactivates lipopolysaccharide, a component of bacterial cell membranes (Shifrin et al., 2012). Through this role, it helps regulate the host immune response and the relationship with commensal microorganisms that make up the intestinal microbiome (Fawley and Gourlay, 2016).

Brush border assembly and the intermicrovillar adhesion complex

During differentiation, a single enterocyte undergoes extensive apical remodeling to generate hundreds of microvilli on its surface. Recent studies from our laboratory have begun to elucidate how the brush border is built and organized. Microvilli begin to

cluster early during differentiation (Crawley et al., 2014b). As differentiation continues, these clusters grow larger and coalesce until the apical surface contains a fully mature brush border (Figure 1-3). Using scanning electron microscopy (SEM) and quick-freeze deep-etch electron microscopy, extracellular thread-like linkages between adjacent microvilli were observed in both CACO-2_{BBE} intestinal epithelial cells and mouse small intestinal tissue (Figure 1-3). Analysis of these structures revealed they were calcium-dependent, protein-based linkages formed between two members of the cadherin superfamily, protocadhein-24 (PCDH24/CDHR2) and mucin-like protocadherin (MLPCDH/CDHR5). These two protocadherins mediate microvillar clustering by forming a *trans* heterophilic adhesion complex that physically links the tips of neighboring microvilli. Knockdown (KD) of either protocadherin results in a loss of microvillar clustering and formation of a disorganized brush border with decreased microvillar density and variable microvillar length (Crawley et al., 2014b).

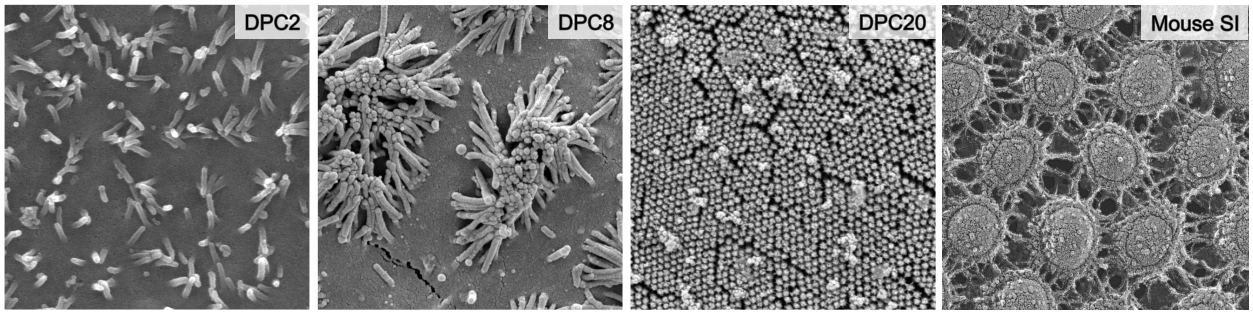

Figure 1-3. Microvilli cluster through distal tip adhesion. Left three images: SEM micrographs of CACO-2_{BBE} cell differentiation showing tip adhesion and growth of microvillar clusters; days post confluency (DPC). Right image: freeze-etch EM of mouse small intestine showing the microvillar protocadherins highly crosslinking adjacent protrusions together Adapted from (Crawley et al., 2014b).

CDHR2 and CDHR5 are highly enriched at the distal tips of microvilli in the intestine (Crawley et al., 2014b). To achieve such polarized localization, these

transmembrane proteins must be anchored to the underlying cytoskeleton and selectively localized to the plus-ends of microvillar actin bundles. Indeed, deletion of the cytoplasmic domain of the protocadherins results in a loss of distal tip targeting and more diffuse microvillar localization (Crawley et al., 2014b). Loss of tip targeting causes defects in microvillar clustering, indicating that the localization of these proteins to the distal ends of microvilli is key for their function. This also demonstrates that interactions with cytoplasmic binding partners are responsible for the tip targeting of the protocadherins and necessary for their proper function.

The microvillar protocadherins can interact with two scaffolding proteins: ANKS4B and USH1C (Crawley et al., 2014b; Crawley et al., 2016; Li et al., 2016). ANKS4B is an ankyrin repeat protein originally identified in a screen for USH1C interacting proteins (Johnston et al., 2004). USH1C is a PDZ domain-containing protein that also functions as an adaptor for stereocilia tip-links (Siemens et al., 2002; Verpy et al., 2000). Both ANKS4B and USH1C localize to the distal tips of microvilli in CACO-2_{BBE} cells and mouse intestinal tissue (Crawley et al., 2014b; Crawley et al., 2016). ANKS4B is required for microvillar clustering and normal brush border assembly, as shown by KD in CACO-2_{BBE} cells (Crawley et al., 2016). Interestingly, type 1 Usher syndrome patients with large deletions in USH1C, the only shared component of the tip-link and IMAC, also suffer from enteropathies (Bitner-Glindzicz et al., 2000). Analysis of intestinal tissue from USH1C knockout (KO) mice (Tian et al., 2010) also revealed defects in brush border morphology (Crawley et al., 2014b). Additionally, these scaffolding proteins directly interact with each other (Li et al., 2016; Li et al., 2017; Yu et

al., 2017). These data suggest that the scaffolding proteins within the IMAC play key roles in complex formation and function in brush border assembly.

Myosins in the brush border

Given the extreme localization of the IMAC to the distal tips of microvilli, there is likely an active mechanism responsible for this targeting. As discussed above, microvilli are supported by a parallel actin bundle with the plus-ends oriented at the distal tips. All myosins, with the exception of myosin-6 (Myo6) (Wells et al., 1999), are plus-end directed. Therefore, an unconventional myosin motor could play a role in either transporting or anchoring the IMAC at microvillar tips. Several myosins are found in the brush border and will be considered in this section.

Class 1 myosins have been well studied, with some localizing within microvilli and stereocilia. These myosins are monomeric and mainly function to link the plasma membrane to the actin cytoskeleton. Numerous cell processes involve class 1 myosins including endo- and exocytosis (Bose et al., 2004; Novak et al., 1995), maintaining cortical rigidity and membrane tension (Dai et al., 1999; Nambiar et al., 2009), and shedding of microvesicles (McConnell and Tyska, 2007). Several class 1 myosins are found in the brush border, with Myo1a being the most abundant by far (Benesh et al., 2010; McConnell et al., 2011). Myo1a forms the lateral bridges, originally described by Mooseker and Tilney (Mooseker and Tilney, 1975), along the entire length of the microvillus, linking the plasma membrane to the actin core. Mice lacking Myo1a had significant perturbations to microvillar membrane morphology and brush border organization (Tyska et al., 2005). Myo1d is the next most abundant in the brush border,

and normally localizes to the terminal web and microvillar tips (Benesh et al., 2010). Loss of Myo1a results in the relocalization of Myo1d and Myo1c, normally associated with the basolateral membrane, to the entire length of the brush border (Benesh et al., 2010; Tyska et al., 2005). Within stereocilia, Myo1c has also been suggested to act as the adaption motor, localizing to the upper tip-link density where it responds to both mechanical load and calcium concentration (Adamek et al., 2008; Batters et al., 2004a; Batters et al., 2004b; Holt et al., 2002; Stauffer et al., 2005). Taking into consideration their localization under normal conditions, monomeric state, and main role in crosslinking membranes to actin, class 1 myosins likely do not play a role in targeting the IMAC.

Myo6 is also present in the brush border, and has been shown to act as either a monomeric tether (Altman et al., 2004) or a dimeric transporter (Buss and Kendrick-Jones, 2011). However, it is the only minus-end directed myosin motor (Wells et al., 1999), and localizes to the terminal web in enterocytes (Heintzelman et al., 1994). Here, it is thought to tether the plasma membrane to the actin cytoskeleton and regulate clathrin-dependent endocytosis (Ameen and Apodaca, 2007; Hegan et al., 2012). Indeed, similar to stereocilia, loss of Myo6 results in plasma membrane lifting and microvillar fusions (Hegan et al., 2012). Myo6 has also been shown to mediate the movement of the Na+/H+ exchanger NHE3 down the microvillus in intestinal epithelial cells (Chen et al., 2014). Taken together, these data suggest Myo6 is likely not responsible for localizing the IMAC, as it is localized and transports cargo to the base of microvilli.

A proteomic analysis of the brush border revealed additional myosins present in microvilli (McConnell et al., 2011). This list included 10 unconventional myosins, including and listed in order of abundance: Myo1a, Myo7b, Myo1d, Myo6, Myo5b, Myo1c, Myo15-like, Myo1e, Myo18a, and Myo7a. Given the abundance, significant homology of the IMAC to the stereocilia tip-link complex, and role of other MyTH4-FERM domain-containing myosins in protrusions, we decided to focus on Myo7b. Myo7b is expressed primarily in the kidney and intestine, where it is enriched at the distal tips of microvilli (Chen et al., 2001; Crawley et al., 2014b). The specific localization of this myosin to the plus-ends of microvillar actin bundles is unique and suggests that it may be a processive motor capable of plus-end directed transport. Myo7b is a MyTH4-FERM domain-containing myosin closely related to a stereocilia myosin, Myo7a (Chen et al., 2001). Interestingly, Myo7a has been linked to the directed transport of cargo molecules to stereocilia tips (Boeda et al., 2002; Senften et al., 2006). Additional MyTH4-FERM domain-containing myosins, Myo10 and Myo15, target to the tips of filopodia (Berg and Cheney, 2002; Berg et al., 2000) and stereocilia (Belyantseva et al., 2003; Delprat et al., 2005), respectively, and have also been shown to directly bind and transport cargo proteins (Belyantseva et al., 2005; Manor et al., 2011; Tokuo and Ikebe, 2004; Zhang et al., 2004). These shared characteristics between Myo7b and proposed transporters in other actin-based protrusions support the hypothesis that Myo7b may play a direct role in the localization of the IMAC.

MyTH4-FERM myosins as protrusion motors

Consisting of Myo7a, Myo7b, Myo10, and Myo15a, the MyTH4-FERM myosins are implicated in the assembly, maintenance, and function of actin-based finger-like protrusions. Myo7a and Myo15a are found in hair cell stereocilia (Hasson et al., 1995; Liang et al., 1999), Myo7b is found in microvilli on the surface of transporting epithelial cells in the kidney and gut (Chen et al., 2001), and Myo10 is found in filopodia on the surface of diverse cell types (Berg et al., 2000). These barbed-end directed motors are grouped together because they contain at least one MyTH4-FERM (MF; myosin tail homology 4 - protein 4.1, ezrin, radixin, and moesin) domain in their cargo-binding tail (Figure 1-4). The distinct MyTH4 and FERM domains form a structural and functional supramodule (Wei et al., 2011; Wu et al., 2011); the FERM domain mediates binding to distinct cargo proteins, whereas the MyTH4 domain functions in microtubule binding (Hirano et al., 2011; Planelles-Herrero et al., 2016; Wei et al., 2011; Wu et al., 2011). Class 7 and 15 myosins have tandem MF domains separated by a SRC homology 3 (SH3) domain. Myo10 contains Pleckstrin homology (PH) domains followed by a single MF domain. None of these myosins are constitutive dimers; instead they form folded, monomeric structures in solution, as demonstrated with Myo7a and Myo10 (Sakai et al., 2015; Umeki et al., 2011; Yang et al., 2009). All MyTH4-FERM myosins exhibit a high duty ratio (Bird et al., 2014; Haithcock et al., 2011; Henn and De La Cruz, 2005; Homma and Ikebe, 2005; Inoue and Ikebe, 2003; Watanabe et al., 2006; Yang et al., 2005), which is consistent with proposed functions in cargo transport, although other roles such as anchoring or channel gating have also been postulated. Below we discuss in more

detail how MyTH4-FERM myosins contribute to the assembly and function of finger-like protrusions.

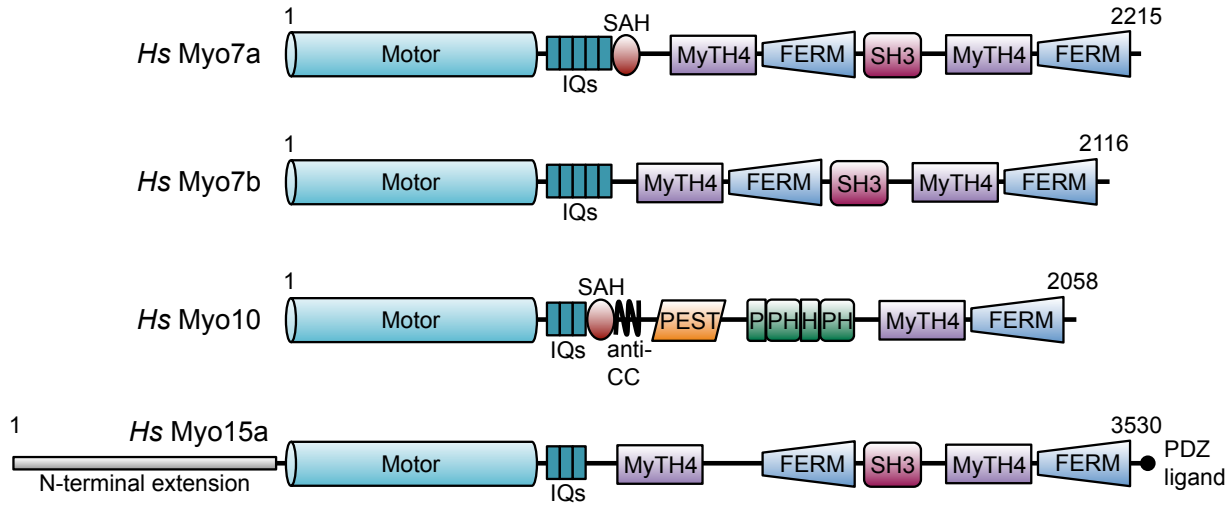

Figure 1-4. Domain diagram of the MyTH4-FERM myosins. Numbers indicate amino acids. Figure depicts isoform 1 for Myo15a; isoform 2 (2307 amino acids) does not include the N-terminal extension. *Hs*, *Homo sapiens*; IQs, IQ calmodulin- or light chain-binding motifs; SAH, single alpha helix; anti-CC, anti-parallel coiled coil; PEST, proline, glutamate, serine, threonine peptide sequence for protein degradation; PDZ, post synaptic density protein (PSD95), Disc large homolog 1 (Dlg1), and zonula occludens-1 (ZO-1).

Movement and localization of MyTH4-FERM myosins in protrusions

The most intuitive function for a myosin motor operating within a protrusion would be transport of materials necessary for assembly and maintenance to the distal tips of these structures, where the dynamic barbed-ends of actin filaments are found. Myo10 is the only MyTH4-FERM myosin where clear evidence for processive motility has been demonstrated in cells, with a velocity of 600 nm/s (Berg and Cheney, 2002; Kerber et al., 2009). This is likely due to the fact that its native protrusion, the filopodium, is amenable to time-lapse imaging with high spatial and temporal resolution. Although parallel actin bundles support all the protrusions discussed in this introduction, each

system contains its own unique complement of actin nucleators, elongators, and bundlers. These distinctions may represent important regulatory factors that serve to guide specific myosins to the proper actin networks *in vivo* (Brawley and Rock, 2009). Indeed, *in vitro* assays have demonstrated that Myo10 prefers actin bundles as compared to single actin filaments (Nagy et al., 2008; Ricca and Rock, 2010; Ropars et al., 2016). Track selectivity of Myo10 is also likely mediated by its anti-parallel coiled coil, which is required for its function in filopodial induction (Lu et al., 2012). This structural feature enables a wider range of step sizes (Ricca and Rock, 2010; Ropars et al., 2016; Sun et al., 2010), which provides access to multiple actin binding sites within the bundle; this in turn might allow Myo10 to navigate around obstacles posed by other actin binding proteins found within the filopodium. Through its PH domains, Myo10 binds to and is regulated by its interaction with phosphatidylinositol-3,4,5-triphosphate (Plantard et al., 2010; Umeki et al., 2011), which may act as a method of localized activation since this lipid is enriched in the leading edge of migrating cells, the site of filopodial formation (Chen et al., 2003; Insall and Weiner, 2001; Nishio et al., 2007). This interaction is thought to relieve auto-inhibition, which in turn, enables dimerization, cargo binding, and motor-driven transport.

In the case of tandem MyTH4-FERM myosins, direct evidence for processive motility has yet to be visualized in cells, although existing evidence does support the idea that at least one aspect of function is a role in transport. Myo15a and Myo7b target to the distal tips of stereocilia and microvilli, respectively, while Myo7a localizes to the upper tip-link density and ankle links of stereocilia (Belyantseva et al., 2003; Chen et al., 2001; Grati and Kachar, 2011). Although monomeric head-neck constructs that lack

cargo-binding domains are unable to tip target, forced dimers of Myo7a motor domains do exhibit tip localization in filopodia, demonstrating the potential for processive movement when multimerized (Sakai et al., 2015; Sakai et al., 2011). Motor activity is required for tip enrichment, further suggesting that this is an active process (Sakai et al., 2011). Additionally, a forced dimer of Myo7a is processive *in vitro* (Yang et al., 2006). In the case of Myo15a, a full-length construct also moves toward filopodial tips in a manner that requires a functional motor domain (Belyantseva et al., 2005). Collectively, these studies implicate motor activity as being critical for the enrichment of MyTH4-FERM myosins at the distal tips of protrusions.

In contrast to Myo10, tandem MyTH4-FERM myosins do not possess well-defined coiled coil domains. To move processively along parallel actin bundles, these myosins would need to undergo some form of dimerization or oligomerization, which could be regulated by cargo binding. In exogenous cell culture models (e.g. Cos-7 cells), dimerization and localization of full-length Myo7a at filopodial tips is dependent on co-expression with its cargo, suggesting that cargo binding plays a key role in activating transporter function (Sakai et al., 2011). Additionally, co-expression of Myo15a with its cargo proteins results in tip localization or increased enrichment of the cargo at protrusion tips in both heterologous culture models and endogenous hair cells (Belyantseva et al., 2005; Delprat et al., 2005; Manor et al., 2011; Sakai et al., 2011). Translocation of Myo15a with its cargoes was also visualized in live Cos-7 cells (Belyantseva et al., 2005; Manor et al., 2011). Together these findings point to a motor-dependent targeting mechanism that requires cargo binding for activation, likely through release of auto-inhibition, induction of dimerization/oligomerization, or both. Moreover,

while all of these studies implicate motor activity in tip targeting of tandem MyTH4-FERM myosins, they do not rule out a role in cargo anchoring or retention.

MyTH4-FERM myosin cargoes and physiological functions

Given the immediate functional insight provided by the identification of binding partners, the search for MyTH4-FERM domain interacting cargoes has been an area of extensive investigation. In the case of Myo10, numerous cargoes have already been uncovered and their physiological functions defined. Overexpression of Myo10 has been shown to induce filopodia formation and elongation (Berg and Cheney, 2002; Bohil et al., 2006). Its ability to initiate filopodia formation is intrinsic to Myo10 itself, as a forced dimer construct lacking any cargo-binding tail domains was sufficient to increase the number of protrusions (Tokuo et al., 2007). However, elongation and stabilization of filopodia are linked to molecules that Myo10 transports to the tips. One such factor is Mena/VASP (Tokuo and Ikebe, 2004), which promotes actin filament elongation by preventing barbed-end capping (Bear et al., 2002). Additionally, Myo10 interacts with and transports β-integrins to filpodial tips to mediate cell-substrate adhesion and stabilize protrusions (Zhang et al., 2004). Myo10 also binds to transmembrane netrin receptors DCC and neogenin, and disruption of these interactions results in defects of axonal projection and path finding (Hirano et al., 2011; Wei et al., 2011; Zhu et al., 2007). These cargoes have been shown to differentially regulate Myo10 activity and induction of filopodia formation, with DCC enhancing basal filopodia elongation and neogenin promoting dorsal filopodia growth (Liu et al., 2012). VE-cadherin and N-cadherin are Myo10 cargoes that function in the formation of early endothelial cell-cell contacts and

neuronal radial migration, respectively (Almagro et al., 2010; Lai et al., 2015). Myo10 also plays a role in endothelial cell migration by transporting BMP6 receptor ALK6 and inducing filopodia formation in a BMP-dependent manner (Pi et al., 2007). The fundamental role that this myosin plays in filopodial formation and elongation is conserved in lower eukaryotes; in the social amoeba *Dictyostelium*, MyTH4-FERM myosin, Myo7, targets to and promotes the growth of filopods (Tuxworth et al., 2001). Apart from its role in filopodia formation, Myo10 also interacts with tubulin in the context of nuclear anchoring, centrosome positioning, and spindle assembly (Kwon et al., 2015; Weber et al., 2004; Woolner et al., 2008). Upregulation of Myo10 is associated with increased breast cancer cell invasion and metastasis, as well as poor prognosis (Arjonen et al., 2014; Cao et al., 2014).

Myo7a cargo binding interactions are critical for the normal mechanosensory function of stereocilia that extend from the apex of inner ear hair cells. Some studies have localized this MyTH4-FERM myosin to the upper end of the tip-link structure (Grati and Kachar, 2011). At upper tip-link densities, Myo7a uses its N-terminal MyTH4-FERM domain to interact directly with the ankyrin repeat protein, SANS (Adato et al., 2005; Wu et al., 2011), which in turn interacts with the actin-bundling PDZ scaffolding protein, harmonin/USH1C (isoform b) (Adato et al., 2005; Yan et al., 2010). The Myo7a/SANS/USH1C complex interacts with the cytoplasmic domain of CDH23 through the N-terminal PDZ domains of USH1C (Adato et al., 2005; Bahloul et al., 2010; Boeda et al., 2002; Pan et al., 2009; Siemens et al., 2002; Wu et al., 2012b). Although the only direct cargo binding interaction in this case is with SANS, Myo7a is indirectly responsible for the localization of USH1C (Boeda et al., 2002). Mutations in Myo7a are

responsible for several genetic hearing impairments, including Usher syndrome type 1B (USH1B) (Weil et al., 1995), autosomal dominant non-syndromic deafness (DFNA11) (Liu et al., 1997b), and autosomal recessive non-syndromic deafness (DFNB2) (Liu et al., 1997a). Type 1 Usher syndrome patients also develop retinitis pigmentosa and progressive vision loss. Expression of mutant variants of Myo7a in mouse models result in a range of morphological and physiological defects with abnormal inner ear function (Kros et al., 2002; Mburu et al., 1997; Self et al., 1998). Mutations that have profound effects on protein stability and expression result in structural and organizational defects of the hair bundle. Although stereocilia still grow and form rows of graded height, they become increasingly disordered after birth, with abnormalities in orientation and position (Self et al., 1998). This eventually leads to the degeneration and reabsorption of some or all of the stereocilia. Additionally, without Myo7a, hair bundles must be deflected beyond their physiological operating range to open the MET channel (Kros et al., 2002). More recently, it was shown that Myo7a interacts and colocalizes with PDZD7 at the ankle-link region of stereocilia (Morgan et al., 2016). This structure couples stereocilia at their base to maintain hair bundle morphology during development (McGee et al., 2006; Michalski et al., 2007). Together, these data suggest that the primary role of Myo7a is not in the formation or elongation of stereocilia per se, but rather in the positioning and maintenance of functional tip-links and ankle links. Although not discussed in depth in this introduction, Myo7a also regulates cargo transport in photoreceptors (Liu et al., 1999; Maerker et al., 2008) and melanosome transport in retinal pigmented epithelium through complex formation with adaptor molecules MyRip and Rab27a (Gibbs et al., 2004; Kuroda and Fukuda, 2005; Liu et al., 1998; Lopes et al., 2007; Sakai et al., 2011).

Myo15a localizes to the tips of stereocilia and is required for stereocilia elongation and staircase formation (Belyantseva et al., 2003). The expression and targeting of Myo15a coincides with the onset of staircase development in the hair bundle, suggesting a potential role in regulation of actin polymerization. Whirlin, a PDZ scaffolding protein, also localizes to stereocilia tips (Belyantseva et al., 2005; Delprat et al., 2005) and colocalizes with Myo15a (Belyantseva et al., 2005). Myo15a directly binds to and translocates whirlin to filopodial tips in cultured cells (Belyantseva et al., 2005; Delprat et al., 2005). Additionally, epidermal growth factor receptor pathway substrate 8 (Eps8) localizes to stereocilia tips and directly interacts with both Myo15a and whirlin (Manor et al., 2011). In mice lacking Myo15a, both whirlin and Eps8 are absent from stereocilia (Belyantseva et al., 2005; Manor et al., 2011). Because Eps8 is an actin bundling and capping protein (Disanza et al., 2004), these findings might offer a molecular rationale for how Myo15a modulates the actin dynamics. Indeed, Myo15a enhances Eps8 tip accumulation and protrusion elongation in both filopodia and stereocilia (Manor et al., 2011). These data suggest that Myo15a forms a complex with whirlin and Eps8 to transport these cargoes to the distal tips and promote stereocilia growth. Myo15a was originally identified as the causative gene for human autosomal recessive non-syndromic deafness, DFNB3 (Friedman et al., 1995; Wang et al., 1998). In mouse models, mutations in the motor or tail domain of Myo15a results in short hair bundles and profound hearing loss (Anderson et al., 2000; Probst et al., 1998). Consistent with its potential function in localizing the proteins whirlin and Eps8, knockout of either cargo phenocopies the Myo15a knockout with decreased stereocilia length and function (Belyantseva et al., 2005; Manor et al., 2011; Mburu et al., 2003;

Zampini et al., 2011). Mutations in these cargo proteins also lead to autosomal recessive non-syndromic deafness (Behlouli et al., 2014; Mburu et al., 2003). These data support a role for Myo15a in building stereocilia by localizing actin-regulatory proteins to the tips.

Myo15a also plays a major role in differential length regulation of stereocilia in different hair bundle rows. More recently, two Myo15a isoforms have been identified to serve differential roles in hair bundle morphology (Fang et al., 2015). Isoform 1 contains a long N-terminal extension and targets to the tips of the shorter stereocilia rows (Fang et al., 2015). Conversely, the isoform lacking this extension, isoform 2, localizes to the longest stereocilia row and is sufficient to target the cargo proteins Eps8 and whirlin (Fang et al., 2015). Specific knockout of isoform 1 unexpectedly resulted in normal hair bundle development (Fang et al., 2015). However, shortly after birth, mutant mice developed severe hearing loss, resulting from the degeneration of the mechanosensing shorter rows (Fang et al., 2015). This study revealed distinct isoform functions for building the hair bundle: initial development of stereocilia that is isoform 2 dependent and maintenance of the mature structure which requires isoform 1 (Fang et al., 2015). What determines the differential localization and cargo binding remains unknown, and is an intriguing question for further investigation.

Remaining questions about MyTH4-FERM myosins

Although significant advances have been made in understanding how MyTH4-FERM myosins function within finger-like protrusions, many unanswered questions still remain. For example, Myo10 seems to be the only mammalian MyTH4-FERM myosin that

functions in protrusion formation *per se*. Existing models suggest that the two motor domains of Myo10 might function as a bundle initiator, by bringing actin filaments together for anti-capping and stable bundling by fascin (Tokuo et al., 2007). This type of bundle initiating activity may be specific to Myo10 given the mechanism of filopodial bundle formation, where filaments originate from a dense meshwork of branched actin (Figure 1-1). The tandem MyTH4-FERM myosins (class 7 and 15) appear to function only in protrusion elongation and organization. Whether this is related to the fact that stereocilia and microvilli emerge from the cell using very different mechanisms than filopodia remains an open question. Apart from Myo10, how do the tandem MyTH4-FERM motors come together to form units capable of processive motility? Although evidence suggests that dimerization is sufficient, the number of motors within a functional unit or complex *in vivo* remains unknown. Other models suggest that directed processive motion might not be the whole story. For example, Myo10 might use motor activity to bias diffusion and promote tip ward movement along parallel actin bundles, as suggested in recent studies (Baboolal et al., 2016). A final question relates to the apparent selectivity that MyTH4/FERM myosins demonstrate toward specific actin populations within the cell. Does this selectivity result from binding to pre-localized cargoes (lipids or proteins) and thus localized activation, or the inherent capacity for these motors to recognize actin tracks with specific features? The latter possibility finds support in previous studies on Myo10, which selectively targets fascin-bundled actin filaments like those that support filopodia (Nagy et al., 2008). The extent to which class 7 and 15 myosins are structurally tuned to move within microvilli and stereocilia remains to be determined. New approaches that combine CRISPR-based endogenous-tagging

of these motors with state-of-the-art super-resolution imaging systems should enable investigators to tackle questions along these lines in live cells.

Myo7b as an intramicrovillar transporter

Myo7b is an unconventional MyTH4-FERM myosin motor protein expressed primarily in the intestine and kidney (Chen et al., 2001). It was shown to localize to the distal tips of microvilli where it co-localizes with several IMAC components (Crawley et al., 2014b). The Myo7b cargo-binding tail was shown to interact with the cytoplasmic domains of the IMAC protocadherins, as well as both scaffolding proteins (Crawley et al., 2014b; Crawley et al., 2016). USH1C was also shown to bind Myo7b via yeast two-hybrid (unpublished data). Indeed, crystal structures of Myo7b interacting with ANKS4B through its MF1 domain and USH1C through its MF2 domain were recently published (Li et al., 2016; Li et al., 2017; Yu et al., 2017).

Staining of USH1C KO mouse intestinal tissue showed the mislocalization of Myo7b to a supra-nuclear compartment (Crawley et al., 2014b). Additionally, loss of USH1C results in the mislocalization of CDHR5 and disruption of normal brush border formation (Crawley et al., 2014b). Although CDHR5 is still trafficked to the brush border, distal tip targeting is lost, resulting in uniform localization along the microvillar axis. These KO mice also have significant defects in brush border organization and morphology including variable microvillar length and loss of tight microvillar packing, as seen by SEM. Linkages can still be visualized in perturbed brush borders. However, they are no longer specifically localized to the distal ends of microvilli, further indicating the importance of tip targeting. Therefore, the proper formation of the IMAC is

necessary for localization to microvillar tips, and loss of a functional adhesion complex causes perturbations to brush border organization and morphology.

Taken together, these data suggest that Myo7b may play a role in complex formation and localization. Since Myo7b is the only complex component that is capable of binding the actin cytoskeleton, Myo7b is likely responsible for the distal tip targeting of the IMAC. Additionally, given its close relation to proposed transporters in other actin-based protrusions, we hypothesized that Myo7b is actively transporting the IMAC to microvillar tips. However, similar to other MyTH4-FERM myosins, Myo7b lacks a coiled coil domain that would allow for independent dimerization (Chen et al., 2001). The multitude of interactions between IMAC components provides a potential mode for higher order oligomerization of Myo7b into transport competent ensembles. The goal of these studies is to elucidate the specific role of Myo7b in the localization of the intermicrovillar adhesion complex and function in brush border formation.

Summary

Unconventional myosins are actin-based molecular motors that serve a multitude of roles within the cell, contributing to cell shape and function. One group of myosin motors, MyTH4-FERM myosins, plays an integral part in building and maintaining finger-like protrusions, which allows cells to interact with their external environment. Suggested to act primarily as transporters, these motor proteins enrich adhesion molecules, actin-regulatory proteins and other factors at the tips of filopodia and stereocilia. One goal of this thesis is to explore the role of a MyTH4-FERM myosin, Myo7b, in transporting cargo molecules to microvillar tips.

We show that Myo7b plays a critical role in microvillar clustering and brush border assembly (Chapter III) (Weck et al., 2016). In the absence of Myo7b, IMAC components become diffusely localized along the microvillar axis, indicating that an important function of this motor is to enrich IMAC components at microvillar tips. We also found that although Myo7b motor domains are capable of supporting transport, motor activity is supplemented by other passive targeting mechanisms. These findings reveal that Myo7b drives the accumulation of the IMAC at the distal tips of microvilli.

To better understand protein interactions within the IMAC, we developed an in-cell reconstitution assay using Myo10-Myo7b chimeric motor proteins (Chapter IV). We demonstrated that these chimeras are capable of translocating Myo7b cargo molecules to the tips of filopodia. Additionally, we tried to establish this system to act a readout for Myo7b multimerization, to address questions about cargo-regulated transport.

Although previous studies provide clear evidence indicating that Myo7b plays a role in microvillar organization and packing, this motor might also play an indirect role in controlling the length of these protrusions by positioning CDHR2 at the distal tips. Here, we provide evidence for this using the in-cell reconstitution assay (Chapter V). Tip-enrichment of CDHR2 causes filopodial bending and bundling. Data suggests that this leads to the stabilization and length uniformity of protrusions.

Our studies are the first to identity a myosin motor protein that localizes cargo to the distal tips of microvilli. We also have developed an assay that can be used to address important questions about IMAC formation and turnover. Finally, our preliminary data suggest a role for tip-enriched adhesion in regulating the length of actin-based protrusions, which may be applied to other systems.

CHAPTER II

MATERIALS AND METHODS

Cloning and constructs

The human cDNA construct of Myo7b used in this study was GI: 122937511. Full-length (amino acids [aa] 1-2116), MD (aa 1-968), and tail (aa 960-2116) constructs were generated by PCR and TOPO cloned into the pCR8 Gateway entry vector (Invitrogen). The forced dimer (MD-GCN4) construct was created by introducing the GCN4 leucine zipper sequence after L968 using 5' ScaI and 3' HindIII sites. The subsequent amino acid sequence immediately follows L968: STMKQLEDKVEELLSKNYHLENEVARLKKLVGE. Restriction enzyme sites, point mutations, and refractory silent mutations were introduced using QuikChange site-directed mutagenesis (Agilent). All entry vectors were verified by DNA sequencing. The entry vectors were then shuttled into destination vectors pEGFP-C1 (Clontech) and pINDUCER20-EGFP-C1 (Crawley et al., 2016) that were Gateway-adapted using the Gateway vector conversion kit (Invitrogen). A non-targeting scramble control shRNA (Addgene; plasmid 1864) and Myo7b KD shRNA clones were expressed in pLKO.1, corresponding to TRC clones TRCN0000247713 and TRCN0000247715 (Sigma).

The full-length *Bt* Myo10 construct was a kind gift from Dr. Richard Cheney. Myo10-Myo7b chimeric motor constructs and FKBP/FRB fusion proteins were generated using Gibson assembly with the following amino acids: ΔSAH 1-814 aa, MD 1-855 aa, MD-CC 1-935 aa. All constructs were verified by DNA sequencing. ANKS4B,

USH1C, CDHR2, and CDHR5 vectors were previously made (Crawley et al., 2014b; Crawley et al., 2016).

Cell culture, lentivirus production, and transfections

All cell lines were cultured at 37°C and 5% CO_2 in DMEM with high glucose and 2 mM L-glutamine supplemented with 10% FBS or with 20% FBS for CACO-2_{BBE} cells. Lentiviral particles were generated by cotransfecting HEK293FT cells with overexpression (pINDUCER20-EGFP-C1) or KD (pLKO.1) plasmids along with the packaging psPAX2 and envelope pMD2.G plasmids using FuGENE 6 (Promega). Cells were incubated for 2 days to allow for lentivirus production before collecting the media containing lentiviral particles. Media was centrifuged at 500xg for 10 mins at 4°C to remove cells and concentrated using Lenti-X Concentrator (Clontech).

For generation of stable cell lines, CACO-2_{BBE} and LLC-PK1-CL4 cells were grown to 90% confluency in T25 flasks. For lentivirus transduction of CACO-2_{BBE} cells, the media was supplemented with 8 μg/ml polybrene and incubated with lentivirus overnight (ON). For stable transfections of LLC-PK1-CL4 cells, transfections were performed using Lipofectamine 2000 (Invitrogen) according to the manufacturer's instructions and the cells were allowed to recover ON. The following day, cells were reseeded into T75 flasks and grown for 3 days. Cells were then reseeded into T182 flasks with media containing 50 μg/ml of puromycin or 1 mg/ml of G418 and grown to select for stable integration.

For transient transfections of Cos-7 and HeLa cells, transfections were performed using Lipofectamine 2000 (Invitrogen) according to the manufacturer's

instructions and the cells were allowed to recover ON. The following day, cells were plated on glass-bottom dishes and/or coverslips coated with 25 μg/ml laminin (Sigma), and allowed to adhere for two hours (Cos-7) or ON (HeLa) before imaging or fixing.

Western blot analysis of cultured cells

CACO-2_{BBE} and LLC-PK1-CL4 stable cell lines were seeded into T25 flasks and grown until 14 DPC or 4 DPC, respectively. All other cell lines were isolated from a T75 flask at about 90% confluency. Cells were washed once with warm PBS and recovered in 5 mL of PBS using a cell scraper. Cells were pelleted at low speed and resuspended in RIPA buffer containing 1mM ATP, 1mM Pefabloc SC (Roche), and 1x cOmplete ULTRA protease inhibitor cocktail (Roche). Cells were lysed by needle aspiration and centrifuged at 16,000xg for 5 min at 4°C. The soluble fraction was recovered and SDS sample buffer was added to a 2x final concentration before being boiled for 3 min. Samples were then separated on 4-12% NuPAGE Bis-Tris gel (Novex) and transferred in Towbin buffer, pH 8.3, to nitrocellulose at 15 V ON. Membranes were blocked for 1 hr in 5% milk in PBS containing 0.1% Tween-20 (PBS-T), washed once with PBS-T, and then incubated with primary antibodies against Myo7b (1:100; Sigma cat. #HPA039131), CDHR2 (1:100; Sigma cat. #HPA012569), CDHR5 (1:500; Sigma cat. #HPA009081), ANKS4B (1:200; Sigma cat. #HPA043523), USH1C (1:250; Sigma cat. #HPA027398), GAPDH (1:1000; Cell Signaling cat. #2118L), actin (1:1000; Sigma cat. #A2066), or anti-GFP (1:1,000; Aves labs Cat#GFP1020) in 5% milk PBS-T for 2 hrs. Membranes were washed three times with PBS-T and incubated with goat anti-rabbit 800 IRdye (1:10,000; Li-Cor) or donkey anti-chicken 800 IRdye (1:10,000; Li-Cor) in 5%

milk PBS-T for 1 hr. Membranes were washed four times with PBS-T before being imaged using a Li-Cor Odyssey infrared imaging system. Images of membrane scans were contrast enhanced and quantified using ImageJ (NIH) with the signal from GAPDH used to normalize sample loading.

Light microscopy

CACO-2_{BBE} and HeLa cells were washed once with warm PBS and fixed with 4% paraformaldehyde in PBS for 15 min at 37°C. After fixation, cells were washed three times with PBS, permeabilized with 0.1% Triton X-100 in PBS for 15 min at room temperature (RT), and again washed three times with PBS. HeLa cells were then incubated with Alexa Fluor 568 or 647 phalloidin (1:200 or 1:100, respectively; Life Technologies), washed four times with PBS, and coverslips were mounted using ProLong Gold Antifade Mountant (Life Technologies). CACO-2_{BBE} cells were then blocked ON with 5% BSA in PBS at 4°C. Cells were washed once with PBS and immunostaining was performed using anti-CDHR2 (1:75; Sigma cat#HPA012569), anti-CDHR5 (1:250; Sigma cat#HPA009081), anti-USH1C (1:70; Sigma cat#HPA027398), and anti-Myo7b (1:25; Sigma cat#HPA039131) at RT for 2 hours. Coverslips were then washed three times with PBS and incubated with Alexa Fluor 488 goat anti-rabbit or Alexa Fluor 647 goat anti-rabbit and Alexa Fluor 568 phalloidin (Life Technologies) diluted 1:200 in PBS for 1 hour at 37°C. Cells were washed four times with PBS and coverslips were mounted using ProLong Gold Antifade Mountant. LLC-PK1-CL4 cells were washed once with warm PHEM buffer (60 mM PIPES, 25 mM HEPES, 5 mM EGTA, 3% sucrose, pH 7.0) and briefly live cell extracted with warm 0.02% saponin in

PHEM buffer. Following extraction, cells were fixed with 4% paraformaldehyde in PHEM buffer containing 0.1% Triton X-100 at 37°C for 10 min. Cells were then washed three times with PBS and stained with Alexa Fluor 568 phalloidin (1:200) in PBS for 30 min at 37°C. Coverslips were washed and mounted as above. For super-resolution microscopy, cells were live cell extracted as above. After fixation, cells were washed three times with PBS and blocked ON with 5% BSA in PBS at 4°C. Cells were washed once with PBS and stained with anti-GFP (1:200; Aves labs Cat#GFP1020) for 2 hours at RT. Coverslips were then washed three times with PBS and incubated with Alexa Fluor 488 goat anti-chicken and Alexa Fluor 568 phalloidin (1:200; Life Technologies) diluted 1:200 in PBS for 1 hour at 37°C. Cells were washed four times with PBS and coverslips were mounted using ProLong Gold Antifade Mountant. Tissue sections and fixed cells were imaged using a Leica TCS SP5 or Nikon A1R laser-scanning confocal microscope. TIRF live cell imaging was performed on a Nikon TiE inverted light microscope equipped with 488 and 561 excitation LASERS, a 100x/1.49 NA TIRF objective, and a Roper Evolve EM-CCD detector (Photometrics). Spinning disk confocal was performed on a Nikon TiE inverted light microscope equipped with 488 and 561 excitation LASERS, a 100x/1.49 NA TIRF objective, and a Prime 95B Scientific CMOS Camera (Photometrics). Structure illumination microscopy was performed using an Applied Precision DeltaVision OMX (GE Healthcare) equipped with a 60x Plan-Apochromat N/1.42 NA oil immersion objective (Olympus) and processed using softWorx software (GE Healthcare). For live cell imaging, cells were maintained in a humid environment at RT and 5% CO2 using a stage-top incubation system (Tokai Hit). Image acquisition was controlled with Nikon Elements software.

Immunohistofluorescence

Paraffin-embedded tissues sections of mouse kidney and intestinal Swiss roles were deparaffinized using Histo-clear solution (Fisher) and rehydrated in a descending graded ethanol series. The sample slides were then subjected to an antigen retrieval step, consisting of boiling for 1 hr in a solution of 10 mM Tris (pH 9.0) and 0.5 mM EGTA. Samples were washed three times with PBS and blocked ON at 4°C in 10% goat serum in PBS. Slides were then washed in PBS three times and stained ON at 4°C with anti-Myo7b (1:25; Sigma cat#HPA039131), anti-CDHR5 (1:200; Santa Cruz sc54112), or anti-USH1C (1:70 Sigma cat#HPA027398), and anti-villin (1:50; Santa Cruz cat. #sc58897) in 1% goat serum in PBS. After washing with PBS four times, samples were stained with Alexa Fluor 488 F(ab')2 goat anti-rabbit and Alexa Fluor 568 F(ab')2 goat anti-mouse (1:1,000; Life Technologies) in 1% goat serum in PBS for 1 hr at RT. Slides were then washed four times with PBS, dehydrated in an ascending graded ethanol series, and mounted in ProLong Gold Antifade Mountant with or without DAPI.

Electron microscopy

All SEM reagents were purchased from Electron Microscopy Sciences. CACO-2_{BBE} cells were seeded at a density of 200,000 cells/well into 0.4-mm 12-mm Transwell-COL inserts (Corning) and allowed to grow to 8 or 20 DPC. Samples were washed once with warm PBS and fixed overnight at 4°C with 3% glutaraldehyde in SEM buffer (0.1 M sucrose and 0.1 M Na-phosphate, pH 7.4). Samples were washed with SEM buffer, postfixed with 1% OsO_4 in SEM buffer on ice for 1 h, and washed with SEM buffer. Samples were dehydrated in a graded ethanol series, dried with hexamethyldisilazane,

mounted on aluminum stubs, coated with gold/platinum in a sputter coater. SEM was performed using a Quanta 250 Environmental scanning electron microscope operated in high vacuum mode with an accelerating voltage of 5-10 kV. Images were contrast enhanced and cropped using ImageJ software (NIH).

Image analysis

All image analysis was done using ImageJ. Using the phalloidin (CACO-2_{BBE} cells) or villin (tissue) signal, line scan analyses of tip enrichment were done by drawing lines parallel to the microvillar axis, starting at the base of the microvillus and extending to the end of the tip. For confocal stacks, measurements were taken using X-Z and Y-Z vertical sections. Intensities of Myo7b, CDHR2, CDHR5, or USH1C along the line were taken and normalized from 0 to 1, with 0 representing the lowest intensity measurement and 1 representing the highest. Microvillar length for each line was also normalized from 0 to 1, with 0 representing the base and 1 representing the tip. Normalized line scans were then plotted together and fitted to either a sum of two (Figure 3-1) or single Gaussian (Figure 3-5, 3-9, and 6-1) using non-linear regression (Prism v.7, GraphPad). The resulting fit revealed the position of peak intensity and distribution width (SD) relative to the microvillar axis. Line scan analysis of microvillar clustering was done by drawing lines along the long axis of five cells in inverted phalloidin images. 8-bit intensities of the phalloidin signal were plotted and stacked onto one graph. Individual cells were scored for microvillar clustering as described previously (Crawley et al., 2014b). Microvillar tip targeting measurements were taken by using X-Z and Y-Z vertical sections from confocal stacks. The intensity at the tip of an individual microvillus was

divided by the cytoplasmic intensity underneath that microvillus. For each cell, 5 microvillar tip to cytoplasmic ratios were averaged, and then binned into a category based on the averaged ratio: no targeting (ratio of <1), moderate targeting (ratio of 1-2.5), and robust targeting (ratio of >2.5). Results were graphed as a percentage of the total number of cells each category occupied. For each stable cell line, at least 20 cells were quantified. CDHR2 intensities were measured by outlining each EGFP-positive cell and recording the mean 8-bit intensity of the far-red channel.

Statistical analysis

For all figures, error bars indicate SD and n values are reported in the figure legends. All graphs were generated and statistical analyses performed in Prism v.6 or 7 (GraphPad). Unpaired t tests were used to determine statistical significance between reported values.

Animal Studies

Animal experiments were carried out in accordance with Vanderbilt University Medical Center Institutional Animal Care and Use Committee guidelines.

CHAPTER III

MYOSIN-7B PROMOTES DISTAL TIP LOCALIZAITON OF THE INTERMICROVILLAR ADHESION COMPLEX

Originally published as:

Weck, M.L., Crawley, S.W., Stone, C.R., and Tyska M.J. (2016). Myosin-7b promotes distal tip localization of the intermicrovillar adhesion complex. Current Biology *26*: 2717-2718.

ABSTRACT

Transporting epithelial cells interact with the luminal environment using a tightly packed array of microvilli known as the 'brush border'. During intestinal epithelial differentiation, microvillar packing and organization are driven by cadherin-dependent adhesion complexes, which localize to the distal tips of microvilli where they drive physical interactions between neighboring protrusions. Although enrichment of the "intermicrovillar adhesion complex" (IMAC) at distal tips is required for proper function, the mechanism driving tip accumulation of these factors remains unclear. Here, we report that the actin-based motor, Myo7b, promotes the accumulation of IMAC components at microvillar tips. Myo7b is highly enriched at the tips of microvilli in both kidney and intestinal brush borders, and loss of Myo7b in differentiating intestinal epithelial cells disrupts intermicrovillar adhesion and thus, brush border assembly. Analysis of cells lacking Myo7b revealed that IMAC components and the resulting intermicrovillar adhesion links are mislocalized along the microvillar axis rather than enriched at the distal tips. We also found that Myo7b motor domains are capable of

supporting tip-directed transport. However, motor activity is supplemented by other passive targeting mechanisms, which together drive highly efficient IMAC accumulation at the tips. These findings illuminate the molecular basis of IMAC enrichment at microvillar tips and hold important implications for understanding apical morphogenesis in transporting and sensory epithelial tissues.

INTRODUCTION

Transporting epithelia, like those that line the luminal surface of the intestine and kidney, build cylindrical actin-based protrusions called microvilli on their apical surface to increase capacity for solute uptake. A single microvillus is supported by a core actin bundle of about 20-30 parallel filaments 0.5 – 5 μm in length, with the barbed ends oriented toward the distal tips and the pointed ends anchored in a mesh of intermediate filaments and spectrin referred to as the terminal web (Mooseker and Tilney, 1975). Enterocytes, the transporting epithelial cells that line the intestinal tract, represent one of the most elaborate cases where thousands of microvilli extend from the surface in a tightly packed array referred to as the brush border (BB). In this context, the BB also serves as a barrier against harmful compounds and microbes in the lumen (Shifrin et al., 2012). The physiological role of the BB in normal gut function is underscored by the fact that numerous intestinal diseases are characterized by perturbation to or complete loss of apical microvilli, including microvillus inclusion disease (Khubchandani et al., 2011; Wilson et al., 2001), Type 1C Usher Syndrome (Bitner-Glindzicz et al., 2000), and infections with attaching/effacing microbes such as enterohemorrhagic and enteropathogenic *E. coli* (Vallance et al., 2002).

Recent studies have begun to explore the molecular mechanisms that promote microvillar growth and organization (Crawley et al., 2014b; Crawley et al., 2016). We previously reported that adhesion between the distal tips of microvilli plays an important role in driving and optimizing the packing of these protrusions during BB assembly (Crawley et al., 2014b). Such intermicrovillar adhesion is mediated by a trans-heterophilic complex formed by two tip-targeted protocadherins, protocadherin-24 (PCDH24/CDHR2) and mucin-like protocadherin (MLPCDH/CDHR5) (Crawley et al., 2014b). Both protocadherins interact with cytoplasmic factors including multi-PDZ domain protein, harmonin-a/USH1C, and ankyrin repeat protein, ANKS4B (Crawley et al., 2014b; Crawley et al., 2016; Li et al., 2016), which also localize to the distal tips of microvilli and together form the intermicrovillar adhesion complex (IMAC) (Crawley et al., 2014b; Crawley et al., 2016). Proper assembly of the IMAC and its enrichment at microvillar tips are critical for normal microvillar clustering and BB assembly (Crawley et al., 2014b; Crawley et al., 2016). Focusing adhesion activity at microvillar tips provides a mechanism for maximizing the packing density of these protrusions and may also contribute to microvillar length uniformity in this system. However, the mechanisms responsible for tip localization of the IMAC have not been elucidated.

A fifth component of the IMAC is the actin-based motor, myosin-7b (Myo7b). Myo7b was originally identified in a PCR screen for myosin-like genes in epithelial cells as a product with high sequence homology to myosin-7a (Bement et al., 1994). As a class VII myosin, Myo7b contains a highly conserved N-terminal motor domain with ATP and actin bindings sites, a central ‘neck’ region containing at least five recognizable IQ motifs, and a C-terminal tail that consists of tandem MyTH4-FERM domains separated

by an intervening SH3 domain (Figure 3-1 A)(Chen et al., 2001). Using its tail domain, Myo7b binds directly to other components of the IMAC; the N-terminal MyTH4-FERM domain binds specifically to ANKS4B, whereas the C-terminal MyTH4-FERM domain interacts with CDHR2, CDHR5, and USH1C (Crawley et al., 2014b; Crawley et al., 2016; Li et al., 2016). Binding partners for the SH3 domain have yet to be identified. Myo7b protein is highly expressed in epithelial tissues of the kidney and intestinal tract, where it localizes to the apical surface (Chen et al., 2001). More recent work revealed localization at the distal tips of microvilli on the surface of CACO-2_{BBE} intestinal epithelial cells (Crawley et al., 2014b). Although enrichment of Myo7b at the distal tips of microvillar actin bundles could reflect barbed-end-directed transporter activity, this possibility has yet to be investigated.

To date, no barbed-end directed transporters have been identified in microvilli. However, myosin-6 has been implicated in cargo retention and/or movement towards the pointed-ends of microvillar actin bundles, which are embedded in the terminal web at the base of the BB (Chen et al., 2014; Yang et al., 2005). Unconventional myosin motors have also been implicated in tipward transport in other actin-supported protrusions, playing roles in the formation and maintenance of these structures. Myosins-3 (Merritt et al., 2012; Salles et al., 2009), -7a (Grati and Kachar, 2011; Sakai et al., 2015; Sakai et al., 2011; Yang et al., 2006), and -15 (Belyantseva et al., 2003; Belyantseva et al., 2005; Manor et al., 2011), have all been implicated in cargo transport within stereocilia, the mechanosensory protrusions that extend from the apical surface of inner ear hair cells. Additionally, myosin-10 has been shown to processively transport

a variety of cargoes to the tips of filopodia in motile cells (Almagro et al., 2010; Berg and Cheney, 2002; Tokuo and Ikebe, 2004; Zhang et al., 2004).

Whether microvilli employ a barbed-end directed transport motor or use other mechanisms to position specific cargoes at their distal tips remains unknown, but Myo7b is an intriguing candidate in either case. Kinetic studies of mouse Myo7b showed ADP release is rate limiting, which leads to a long-lived actin bound state and correspondingly high duty ratio (~0.8) (Henn and De La Cruz, 2005). Myo7b from *Drosophila* also exhibits a very high duty ratio (Yang et al., 2005). Although these properties are consistent with a role in processive transport, Myo7b does not possess a coiled coil domain that would allow for robust dimerization. Previously characterized transporters deal with the same structural limitation using a mechanism in which oligomerization/dimerization is induced by cargo binding (Phichith et al., 2009; Sakai et al., 2011; Umeki et al., 2011; Yu et al., 2009).

Because Myo7b is the only component of the IMAC with a recognizable actin-binding domain, we hypothesized that this motor could function as a physical link to the actin cytoskeleton and play a role in localizing the IMAC at the distal ends of microvillar actin bundles. Here, we provide evidence in support of this hypothesis and show that Myo7b serves to enrich the IMAC at the distal tips of microvilli. By properly localizing the IMAC, Myo7b plays a crucial role in microvillar organization and BB formation, a role that requires functional motor and cargo-binding tail domains. Taken together, these findings provide a molecular mechanism underpinning the localization and thus function of the IMAC; this work also holds implications for understanding apical morphogenesis in a variety of epithelial contexts.

RESULTS

Myo7b localizes to the distal tips of microvilli

Components of the IMAC are enriched at the distal tips of microvilli in intestinal and kidney epithelia (Crawley et al., 2014b; Crawley et al., 2016). Additionally, all endogenous IMAC proteins and exogenous fluorescent protein-tagged constructs of ANKS4B, CDHR2, and CDHR5 also localize to microvillar tips in the CACO-2_{BBE} intestinal epithelial cell culture model (Crawley et al., 2014b; Crawley et al., 2016). Previous studies showed that Myo7b is expressed in kidney and intestinal tissue where it localizes to the BB in kidney, and the distal portion of microvilli in intestinal epithelial cells (Chen et al., 2001). To extend these results and determine the precise localization of Myo7b, we stained paraffin-embedded kidney and intestinal tissue sections using a newer Myo7b-specific antibody (*Sigma* HPA039131). In the intestine, tissue staining revealed distal tip enrichment of the motor within BB microvilli, along the length of the villus (Figure 3-1 B and E). Expression of Myo7b is decreased in the crypt compartments, with little detection in crypt microvilli (Figure 3-2 A, open arrowheads). Increased expression and tip enrichment of Myo7b appeared in cells transitioning out of the crypt and onto the base of the villus (Figure 3-2 A, filled arrowheads and arrows). Myo7b also showed striking enrichment at the distal tips of microvilli on the surface of tubule epithelial cells in cortical kidney sections (Figure 3-1 C and E). In both intestine and kidney, the position of the Myo7b intensity peak with respect to the microvillar axis was remarkably similar (L_{PI} = 0.83 ± 0.11 and 0.87 ± 0.11 respectively, where 0 = base and 1 = tip).

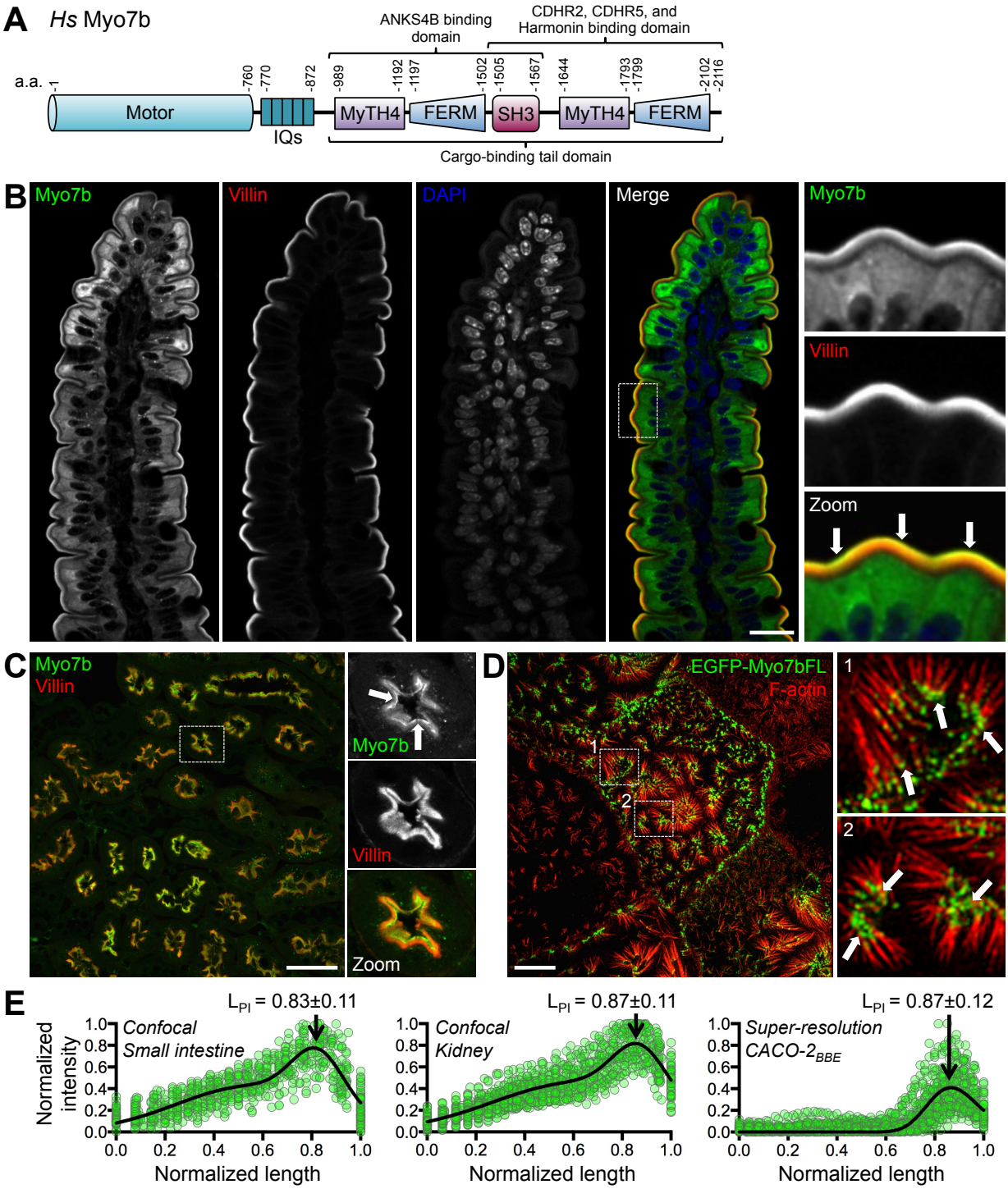

Figure 3-1. Myo7b localization in native tissue and CACO-2$_{BBE}$ cells. (A) Domain diagram of full-length Myo7b. Numbers indicate amino acids. **(B)** Confocal images of mouse small intestinal tissue stained for Myo7b (green), villin (red), and DAPI (blue). Boxed region indicates field shown in zoomed images. Arrows point to distal tip enrichment of Myo7b within the BB. Scale bar, 20 μm. **(C)** Confocal images of mouse kidney tissue stained for Myo7b (green) and villin (red). Boxed area indicates region in zoomed images. Arrows point to distal tip enrichment of Myo7b within the BB. Scale

bar, 50 μm. **(D)** Structure illumination microscopy of CACO-2_{BBE} cells overexpressing full-length Myo7b N-terminally tagged with EGFP (green) and stained for F-actin (red). Boxed areas indicate regions in zoomed images. Arrows highlight distal tip enrichment. Scale bar, 5 μm. **(E)** Line scans of Myo7b intensity parallel to the microvillar axis in tissue sections or CACO-2_{BBE} cells overexpressing EGFP-Myo7b; 0=base and 1=tip. N = 55 scans for SI, 53 scans for kidney, and 62 scans for CACO-2_{BBE}. Gaussian curve fits are marked with length at peak intensity (L_{PI}) ± distribution width (SD).

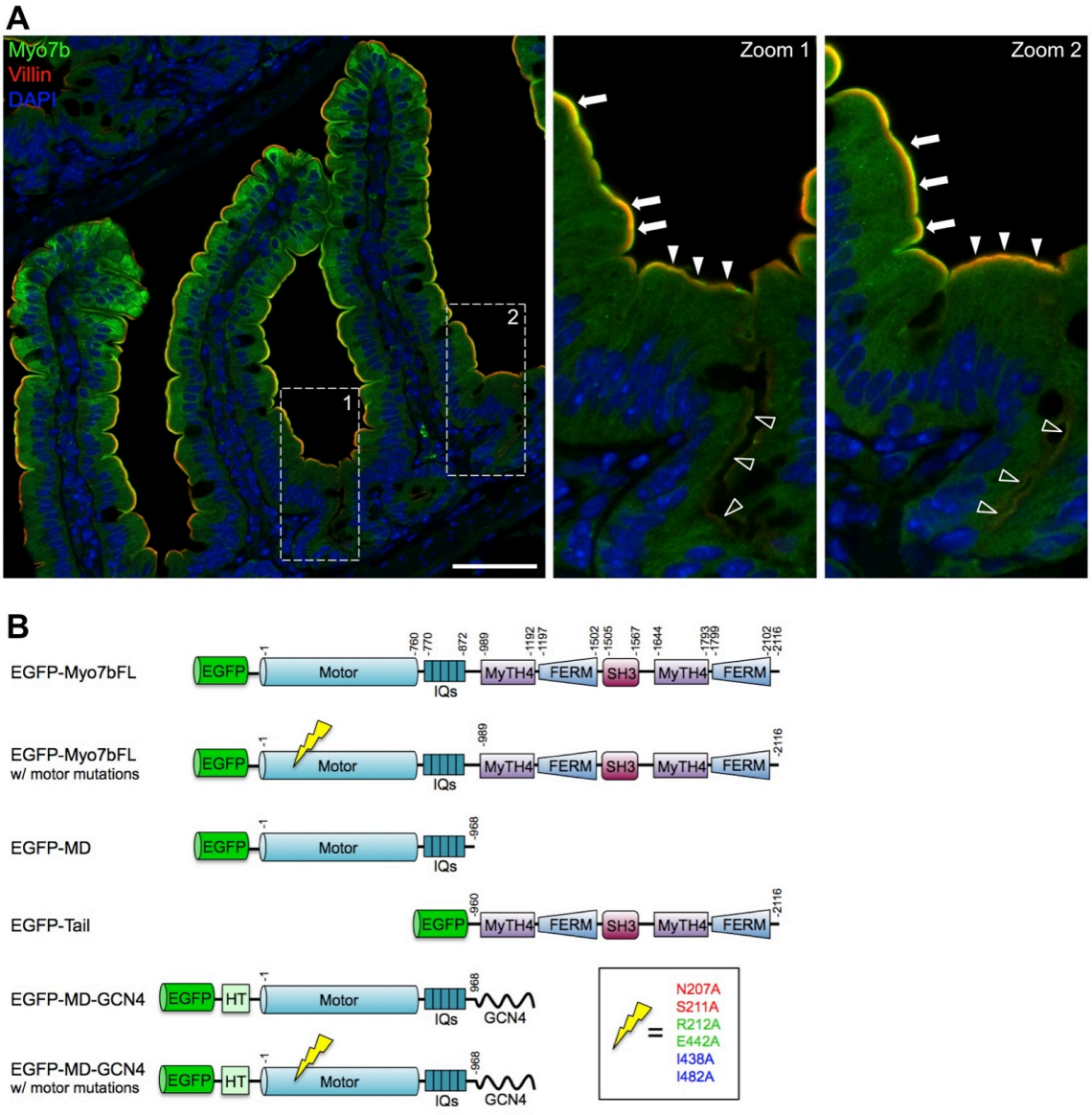

Figure 3-2. Myo7b localization along the crypt-villus axis in native tissue. (A) Confocal images of mouse intestinal tissue stained for Myo7b (green), villin (red), and DAPI (blue). Boxed areas indicate regions in zoomed images. Open arrowheads point to crypt microvilli with little expression of Myo7b and villin. Filled arrowheads point to the crypt-villus transition where Myo7b and villin expression begins to increase. Arrows point to robust distal tip enrichment of Myo7b within the brush border on the villus. Scale

bar, 50 μm. **(B)** Constructs of Myo7b used in this study. Numbers indicate amino acids; HaloTag (HT).

We previously showed that endogenous Myo7b enriches towards the distal tips of clustering microvilli in CACO-2_{BBE} cells after two weeks of differentiation (Crawley et al., 2014b). To determine if tagged variants of Myo7b also target to microvillar tips in this model, we stably expressed an N-terminally EGFP-tagged full-length construct of human Myo7b (Figure 3-2 B) in CACO-2_{BBE} cells. After two weeks of differentiation, this construct localizes to the distal tips of microvilli in a manner similar to endogenous Myo7b (L_{PI} = 0.87 ± 0.12, Figure 3-1 D and E). Thus, Myo7b is well positioned to play a role in localizing IMAC components to microvillar tips.

Myo7b is required for normal BB assembly

Previous studies showed that loss of IMAC components (CDHR2, CDHR5, USH1C, or ANKS4B) results in the disruption of microvillar clustering and BB formation (Crawley et al., 2014b; Crawley et al., 2016). Based on our observations using both light and scanning electron microscopy (SEM) (Crawley et al., 2014b; Crawley et al., 2016), differentiating CACO-2_{BBE} monolayers typically exhibit a heterogeneous surface morphology, although the majority of cells present prominent “tipi”-shaped clusters of microvilli interacting via their tips and surrounded by regions of free apical membrane space (Figure 3-3 B). Tipi-clustered microvilli represent an intermediate packing state that is critical for the progression to a mature BB (Crawley et al., 2014b; Crawley et al., 2016). Other cells exhibit immature microvillar growth, with a peripheral F-actin signal that is much higher than medial regions of the cell surface (Figure 3-3 B).

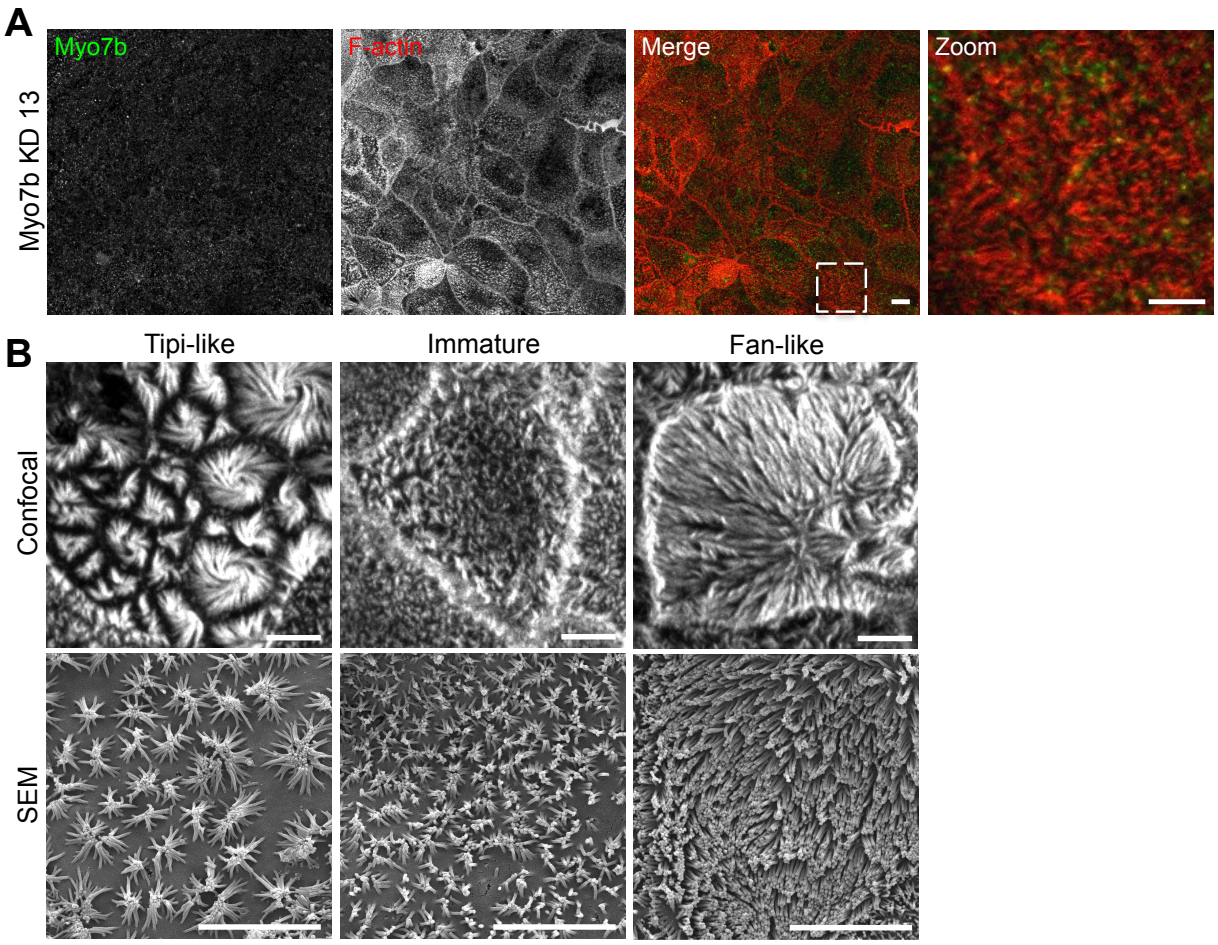

Figure 3-3. Loss of Myo7b in CACO-2_{BBE} cells decreases microvillar clustering. **(A)** Confocal images of Myo7b (green) and F-actin (red) of Myo7b KD13 CACO-2_{BBE} cells at 14 DPC. Boxed area indicates region in zoomed image. Scale bars, 10 μm; 5 μm in zoom. **(B)** Confocal images of F-actin (top row) and SEM images (bottom row) of the different BB morphologies observed in CACO-2_{BBE} cells. Only cells with tipi-like clusters were counted as cells with clustering microvilli in quantifications. Scale bars, 5 μm.

To determine if Myo7b also plays a role in organizing microvilli during BB assembly, we generated two independent, stable lentivirus-mediated knockdowns (KDs) of Myo7b in CACO-2_{BBE} cells, confirmed by western blot and immunostaining (Figure 3-3 A; Figure 3-4 A and B). Myo7b KD cells were still able to assemble microvilli, although cell surface morphology was perturbed. The presence of tipi-shaped clusters was scored as described previously (Crawley et al., 2014b; Crawley et al., 2016) after two

weeks of differentiation. Myo7b KD resulted in a significant decrease in clustering (Figure 3-4 C), which was evident in confocal images of phalloidin-stained monolayers. Line scans across the long axis of control cells revealed large variations in phalloidin-labeling intensity caused by the juxtaposition of free apical space (low intensity) with well-formed tipi clusters of microvilli (high intensity) (Figure 3-4 D). These large variations in phalloidin signal were absent in Myo7b KD cells. Moreover, in Myo7b KD cells that were able to build long microvilli, we noticed aberrant “fan”-like arrays (Figure 3-3 B), which indicated failure of these protrusions to extend away from the cell surface. SEM of 8 days post confluency (DPC) scramble control cells revealed large microvillar clusters surrounded by free apical space with almost exclusively tip-to-tip interactions (Figure 3-4 E, top row). Most observable linkages were localized to the tips of adjacent microvilli (Figure 3-4 E, green circles). In contrast, KD of Myo7b caused disorganization of microvilli with little free apical space, resulting in a disheveled BB (Figure 3-4 E, bottom row). Aberrant contacts between microvilli (e.g. tip-to-base and base-to-base interactions) were readily observed in KD cells. We also observed extracellular links along the full length of microvilli (Figure 3-4 E, red arrows) as well as aberrant links between microvilli and the cell surface (Figure 3-4 E, white outlined red arrows). Perturbations in Myo7b KD cell apical surface organization were also observed at 21 DPC, a time point by which microvillar packing is typically optimized in control cultures (Figure 3-4 F). Together, these findings allow us to conclude that Myo7b is required for normal BB assembly.

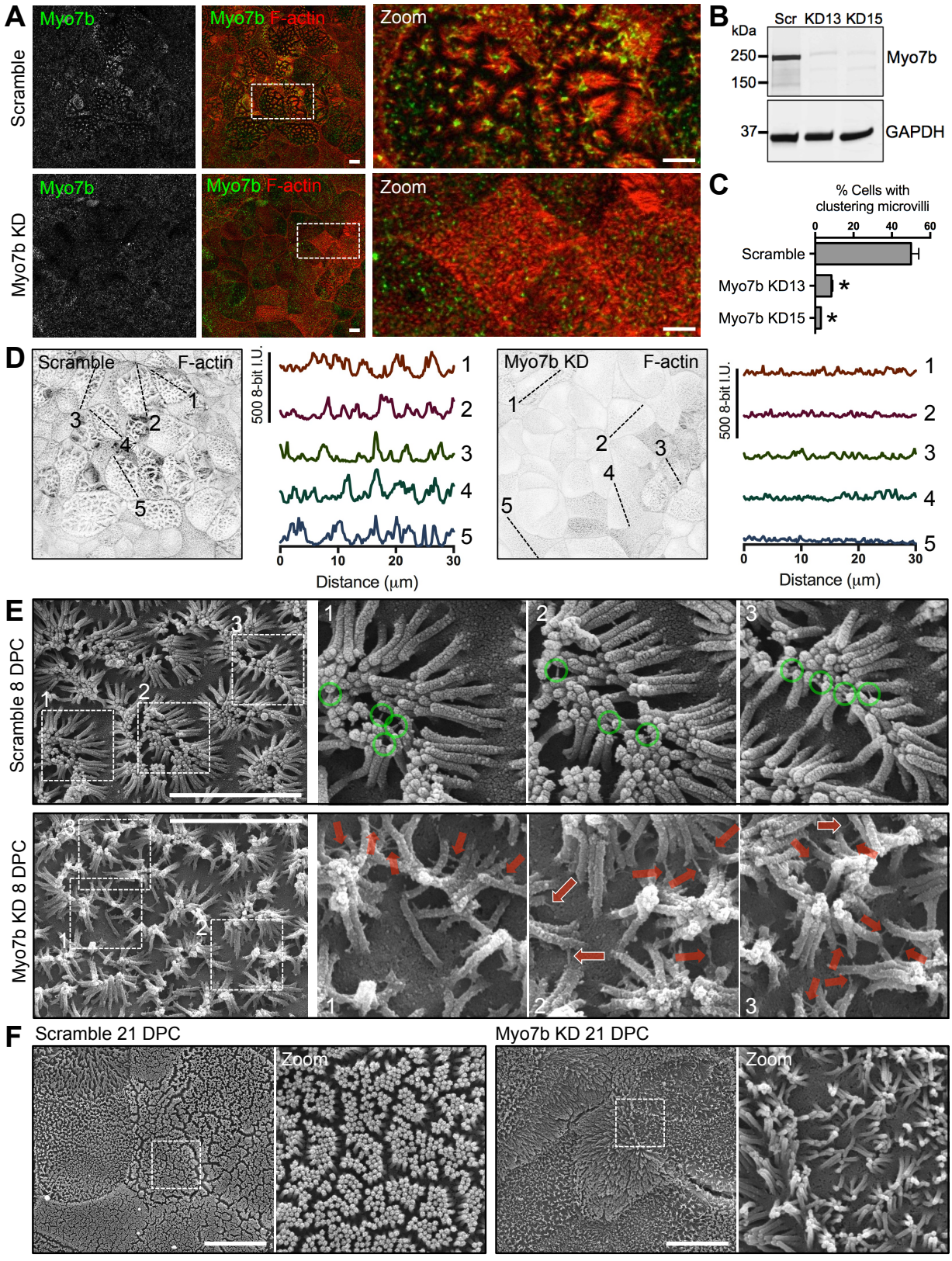

Figure 3-4. Myo7b KD in CACO-2$_{BBE}$ cells results in defects in BB assembly. (A) Confocal images of Myo7b (green) and F-actin (red) of scramble and Myo7b KD15

CACO-2_{BBE} cells at 14 DPC. Boxed area indicates region in zoomed images. Scale bars, 10 μm; 5 μm in zooms. **(B)** Western blots show near complete KD of Myo7b in CACO-2_{BBE} cells expressing two distinct shRNAs (KD13 or KD15). **(C)** Quantification of percentage of cells with clustering microvilli. Bars indicate mean ± SD. N = 1,313 cells for Scramble, 721 cells for KD13, and 1,451 cells for KD15. *p<0.0001, t test. **(D)** Line scan analysis of five cells (indicated with dashed line), derived from F-actin channel images from (A). **(E)** SEM images of scramble and Myo7b KD15 cells at 8 DPC. Boxed area indicates region in zoomed images. Green circles show IMAC links at the tips of clustering microvilli. Solid red arrows and outlined red arrows show IMAC links at the base of adjacent microvilli and between microvilli and the plasma membrane, respectively. Scale bars, 10 μm. **(F)** SEM images of scramble and Myo7b KD15 cells at 21 DPC. Boxed area indicates region in zoomed images. Scale bars, 10 μm.

Distal tip enrichment of the IMAC is dependent on Myo7b

Myo7b directly interacts with all other IMAC components (Crawley et al., 2014b; Crawley et al., 2016; Li et al., 2016). To examine the role of Myo7b in targeting the IMAC to microvillar tips, we stained Myo7b KD cells for individual components of the complex, including CDHR2, CDHR5, and USH1C. In each case, KD of Myo7b resulted in a striking loss of distal tip enrichment (Figure 3-5 and 3-6 A). Using z-axis confocal sections, we quantified the localization of each IMAC component by generating line scans along the length of individual microvilli (Figure 3-6 B). The resulting L_{PI} values for all IMAC components were significantly reduced, indicated loss of distal tip enrichment in Myo7b KD cells (Figure 3-5 B, D, and F). Immunofluorescence imaging and western blots revealed decreased expression levels of CDHR2 and USH1C in KD cells (Figure 3-5 A and E; Figure 3-6 C and D). Strikingly, in cells that were able to maintain higher levels of IMAC proteins, we observed diffuse localization along the microvillar axis (Figure 3-5 C and Figure 3-6 A). Therefore, the defects in microvillar organization observed in Myo7b KD cells are most likely due to loss of distal tip enrichment of IMAC cargoes.

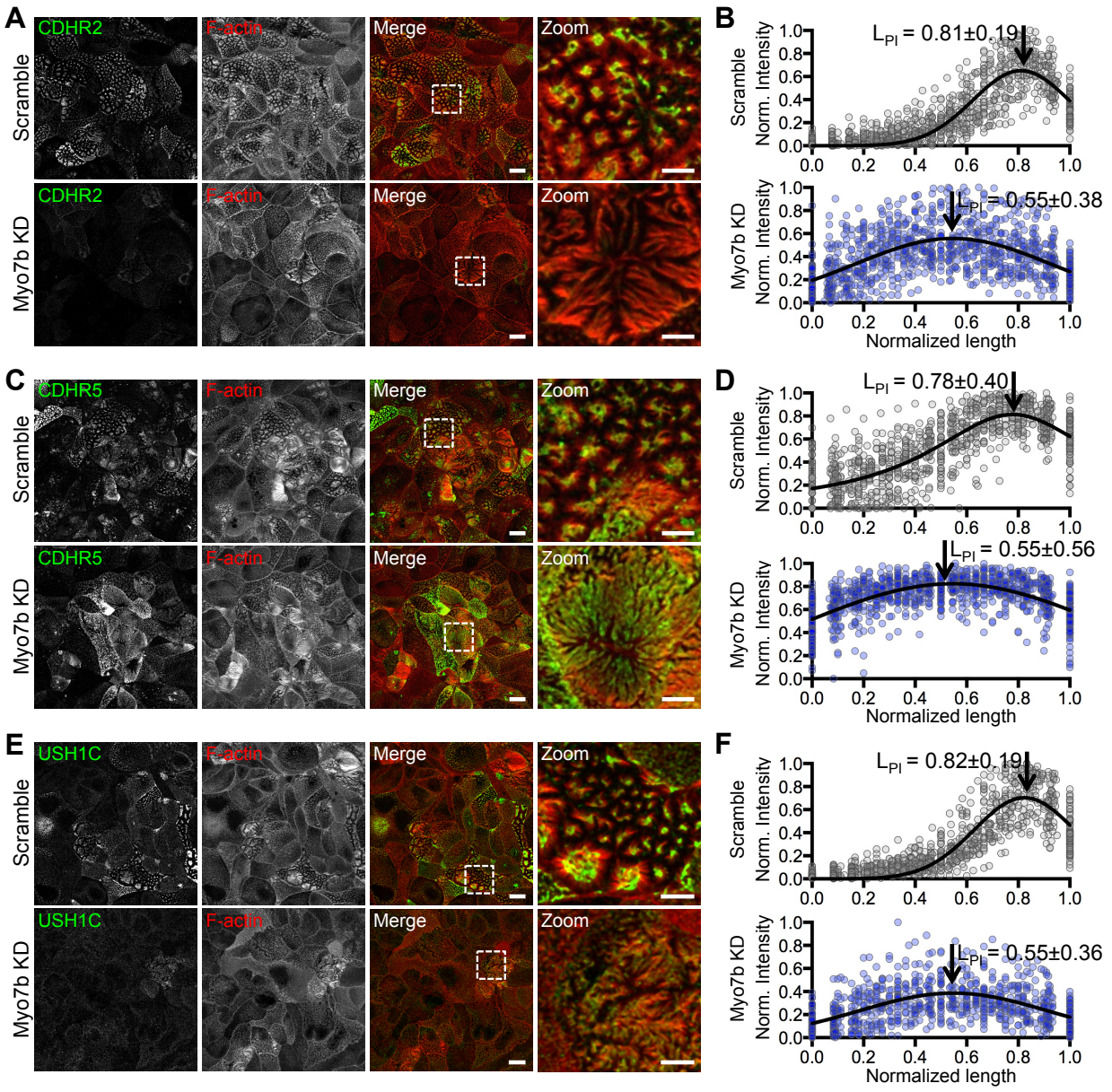

Figure 3-5. Myo7b KD results in loss of IMAC enrichment at microvillar tips. (A, C, E) Confocal images of CDHR2, CDHR5, and USH1C staining (green) and F-actin labeling (red) in Myo7b KD15 CACO-2_{BBE} cells at 14 DPC. Boxed area indicates region in zoomed images. Scale bars, 10 μm; 5 μm in zooms. **(B, D, F)** Line scan analysis of CDHR2, CDHR5, and USH1C staining intensity parallel to the microvillar axis. 0=base and 1=tip. N = 64 scans for each plot. Gaussian curve fits are marked with length at peak intensity (L_{PI}) ± distribution width (SD). See also Figure S3.

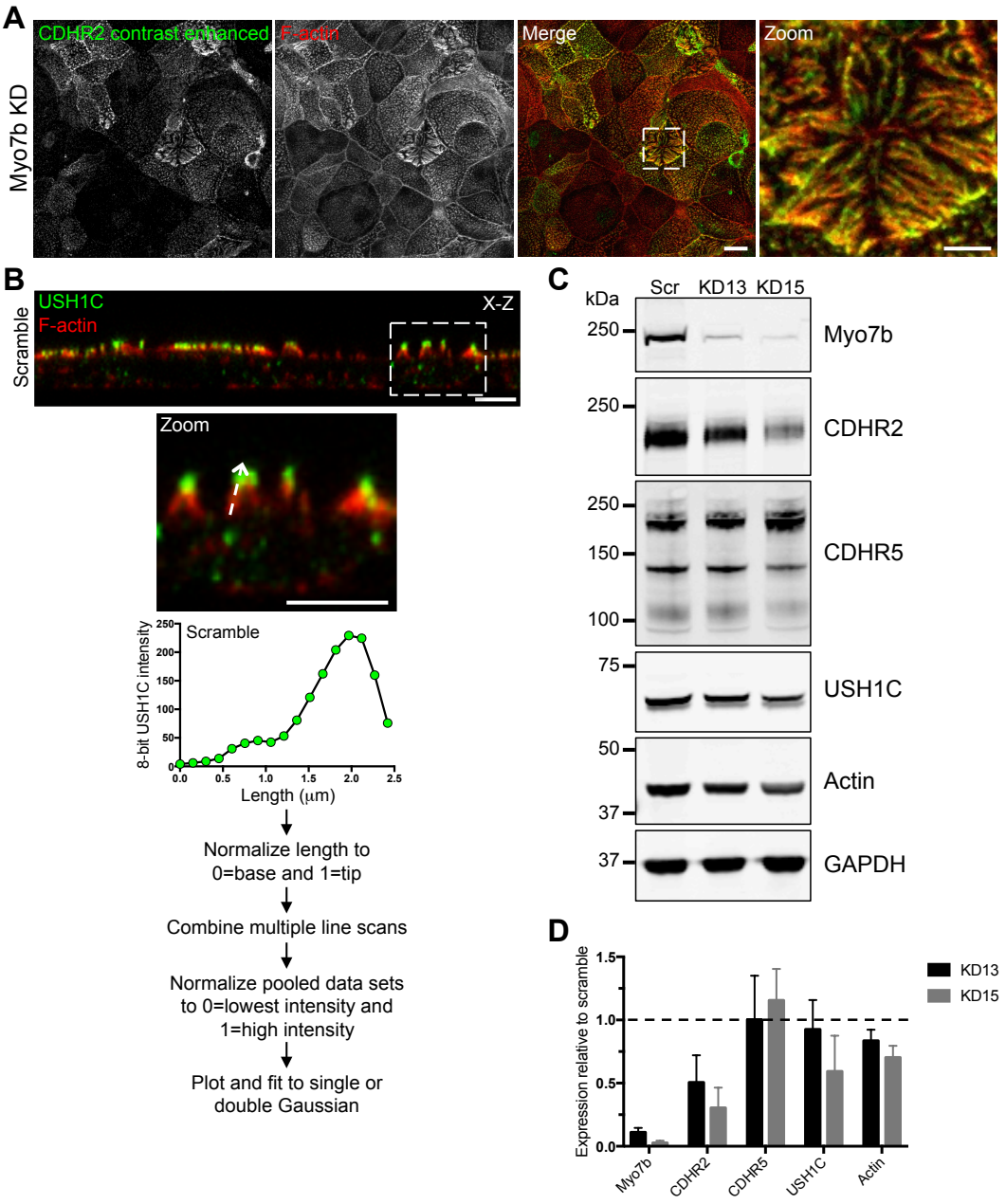

Figure 3-6. Myo7b KD in CACO-2$_{BBE}$ cells results in a decrease of IMAC expression. (A) Confocal images from Figure 3A that have been contrast enhanced to show the decreased expression and localization of CDHR2 (green) along the microvillar axis, F-actin (red), in Myo7b KD cells at 14 DPC. Boxed area indicates region in zoomed image. Scale bars, 10 μm; 5 μm in zoom. **(B)** Illustration of how line scans were acquired, combined, and normalized. Vertical section from confocal image of USH1C (green) and F-actin (red) of scramble CACO-2$_{BBE}$ cells at 14 DPC. Boxed area indicates region in zoomed image. Dashed arrow indicates line scan used to generate plot. Scale bars, 5 μm. **(C)** Western blot analysis of endogenous CDHR2, CDHR5, USH1C, and actin in lysates from 14 DPC scramble control and two independent Myo7b KD stable

cell lines. **(D)** Quantification of endogenous Myo7b, CDHR2, CDHR5, USH1C, and actin in lysates from 14 DPC scramble control and two independent Myo7b KD stable cell lines. Values are expressed relative to scramble.

Myo7b microvillar tip localization requires a functional motor domain

In studies of unconventional myosins that localize to actin-based protrusions in other systems, tip targeting is viewed as a telltale sign of processive barbed-end directed motility (Belyantseva et al., 2005; Berg and Cheney, 2002). To examine the role of the motor domain in Myo7b targeting, we used mutagenesis to create variants of Myo7b predicted to be deficient in motor activity, and then assessed their ability to target to microvillar tips. Many residues that are critical for myosin catalytic and mechanical function are perfectly conserved across eukaryotes. Thus, we used information from previous studies to generate variants of Myo7b deficient in specific aspects of motor function (Figure 3-7 A). A similar strategy has been used previously by others to assess the significance of myosin motor function in cells (Aschenbrenner et al., 2004; Belyantseva et al., 2005; Sakai et al., 2011). We introduced three classes of mutations into the Myo7b motor domain: (1) mutations expected to prevent nucleotide binding and lock the motor in a strong actin bound state (N207A and S211A) (Shimada et al., 1997), (2) mutations expected to block phosphate release and inhibit actin binding (R212A and E442A) (Sasaki et al., 1998; Shimada et al., 1997), and (3) mutations expected to ‘uncouple’ conformational changes in the nucleotide binding pocket from lever arm rotation, which would result in normal ATPase activity and actin binding, but no motor activity (I438A and I482A) (Kambara et al., 1999; Sasaki et al., 2003).

A

Dd Myo2	*Hs* Myo7b	Actin movement	Actin binding	ATPase activity
N233A	N207A	None	Strong	None
S237A	S211A	None	Strong	None
R238A	R212A	None	Weak	None
E459A	E442A	None	Weak	None
I455M	I438A	None	WT	WT
I499A	I482A	None	WT	WT

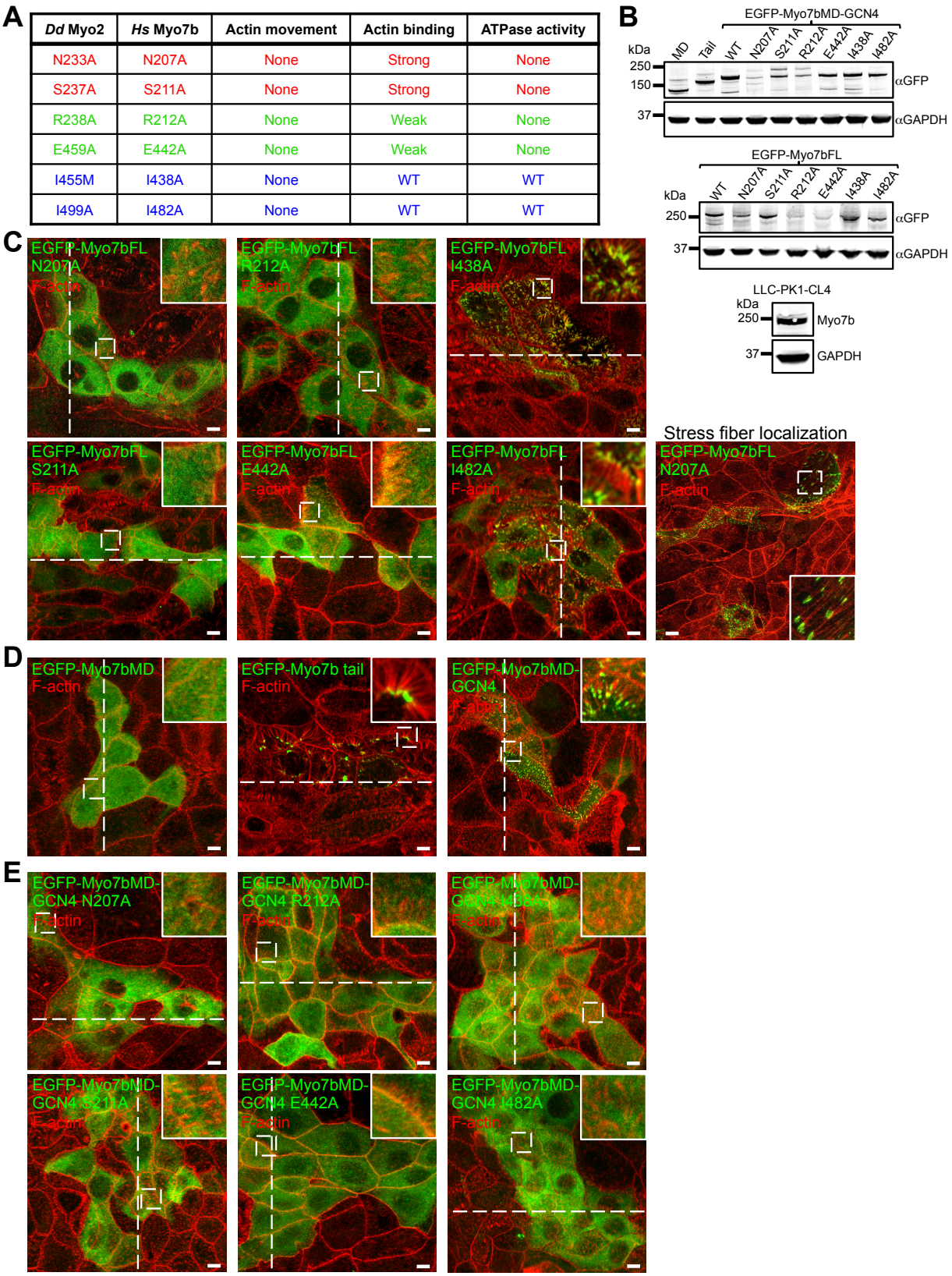

Figure 3-7. Structure-function analysis of Myo7b motor requirements for tip targeting. (A) Motor domain point mutations generated in human (*Hs*) Myo7b

compared to the mutational analyses done previously in *Dictyostelium discoideum* (*Dd*) myosin 2 (Kambara et al., 1999; Sasaki et al., 2003; Sasaki et al., 1998; Shimada et al., 1997). **(B)** Western blot analysis of construct expression in LLC-PK1-CL4 stable cell lines at 4 DPC and endogenous Myo7b from wild-type LLC-PK1-CL4 cells at 4 DPC. **(C)** Confocal images of motor domain mutations in the full-length Myo7b construct. Boxed areas indicate regions in zoomed insets. Dashed lines indicate X-Z vertical sections shown in Figure 3-8. Scale bars, 5 μm; 10 μm in stress fiber localization image. **(D)** Confocal images of deletion and forced dimer constructs of Myo7b. Boxed areas indicate regions in zoomed insets. Dashed lines indicate X-Z vertical sections shown in Figure 3-8. Scale bars, 5 μm. **(E)** Confocal images of motor domain mutations in the forced dimer Myo7b construct. Boxed areas indicate regions in zoomed insets. Dashed lines indicate X-Z vertical sections shown in Figure 3-8. Scale bars, 5 μm.

Mutant variants of Myo7b were tagged with EGFP and stably expressed in LLC-PK1-CL4 kidney epithelial cells to assay microvillar tip targeting. Construct expression was confirmed using western blot analysis (Figure 3-7 B). LLC-PK1-CL4 cells express endogenous Myo7b (Figure 3-7 B) and differentiate rapidly (~3-4 days), which allowed efficient production of the numerous stable lines required for these experiments. We used the ratio of microvillar tip intensity:cytoplasmic intensity to quantify the extent of tip targeting for each construct. Ratio values from single cells were binned into the three categories based on the efficiency of targeting: none (ratio of <1), moderate (ratio of 1-2.5), and robust (ratio of >2.5). Our positive control, EGFP-tagged WT full-length Myo7b (EGFP-Myo7bFL) localized as expected in this system (Figure 3-8 A); ~50% of cells expressing this WT construct exhibited robust tip targeting (Figure 3-8 B). Myo7b mutants expected to be locked in either strongly or weakly bound states were unable to target to microvillar tips (Figure 3-7 C and Figure 3-8 B). Thus, active ATPase cycling and normal actin binding contribute to the tip enrichment of full-length Myo7b. Mutants expected to strongly bind actin also demonstrated aberrant stress fiber localization (Figure 3-7 C). Interestingly, Myo7b mutants expected to exhibit uncoupling of catalytic

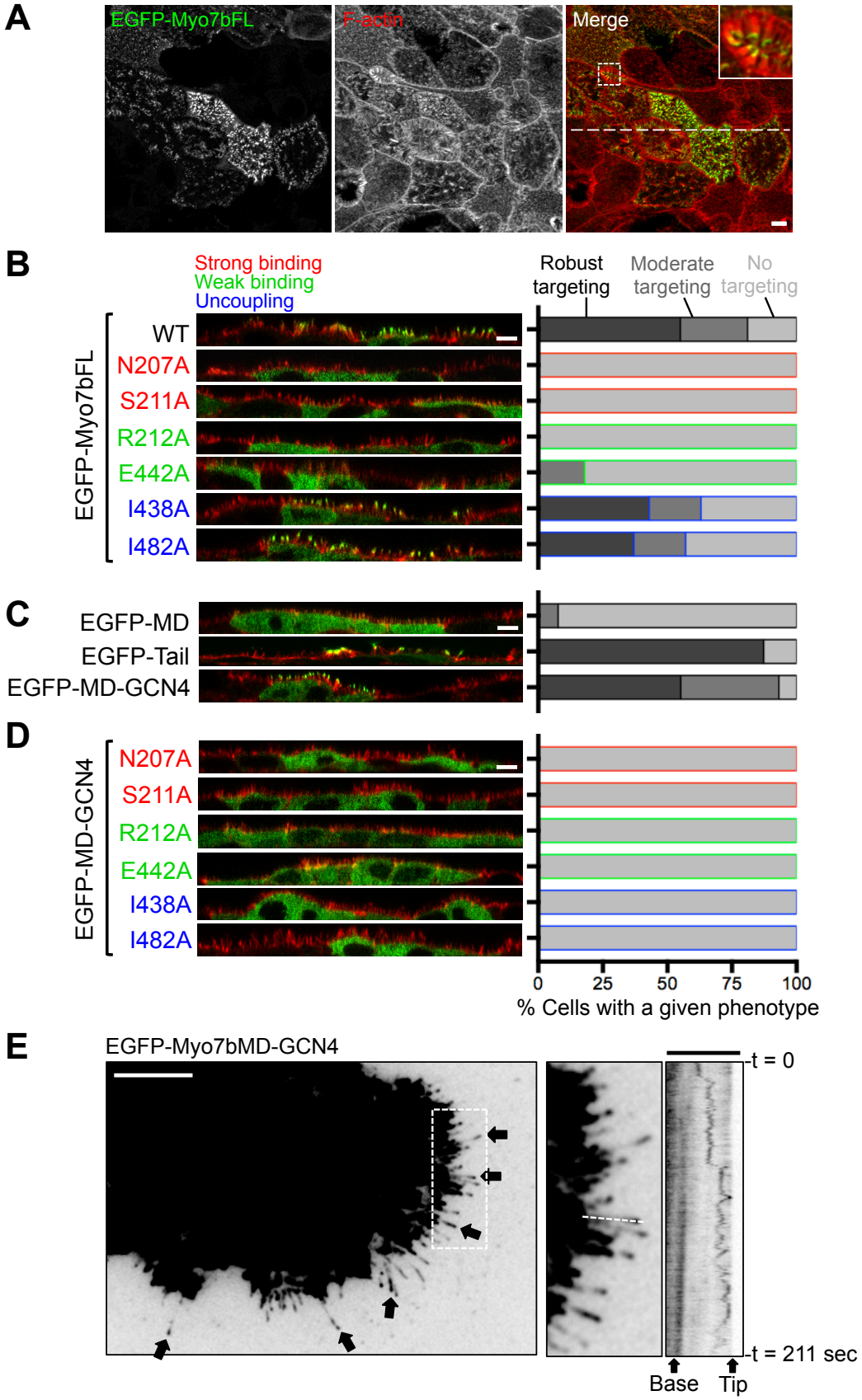
A
EGFP-Myo7bFL
F-actin
Merge
B
Strong binding
Weak binding
Uncoupling
Robust targeting
Moderate targeting
No targeting
EGFP-Myo7bFL
WT
N207A
S211A
R212A
E442A
I438A
I482A
C
EGFP-MD
EGFP-Tail
EGFP-MD-GCN4
D
EGFP-MD-GCN4
N207A
S211A
R212A
E442A
I438A
I482A
0
25
50
75
100
% Cells with a given phenotype
E
EGFP-Myo7bMD-GCN4
t = 0
t = 211 sec
Base
Tip

Figure 3-8. Structure-function analysis of Myo7b tip targeting. (A) Confocal images of full-length EGFP-tagged Myo7b (green) stable overexpression in LLC-PK1-CL4 cells stained for F-actin (red) at 4 DPC. Boxed area indicates region in zoomed inset. Dashed line indicates WT X-Z vertical section shown in (B). Scale bar, 5 μm. **(B)** Vertical sections from confocal images of cells expressing EGFP-tagged full-length Myo7b constructs (EGFP-Myo7bFL) with point mutations indicated. Quantification of tip targeting in each case was performed by binning tip:cytoplasmic intensity ratios into three categories as indicated. Scale bar, 5 μm. **(C)** Vertical sections from confocal images of cells expressing EGFP-tagged Myo7b motor domain (EGFP-MD), Myo7b tail domain (EGFP-Tail), or a forced dimer of Myo7b motor domains (EGFP-MD-GCN4), quantified as in (B). Scale bar, 5 μm. **(D)** Vertical sections from confocal images of cells expressing a forced dimer of Myo7b motor domains (EGFP-MD-GCN4) with point mutations indicated, quantified as in (B). Scale bar, 5 μm. **(E)** TIRF images of a Cos-7 cell co-transfected with mCherry-fascin (not shown) and the EGFP-tagged Myo7b forced dimer construct (EGFP-MD-GCN4). Black arrows point to filopodial tip enrichment. Boxed area indicates region in zoomed image. Dashed line indicates line used to generate accompanying kymograph. Scale bars, 10 μm; 3.5 μm in kymograph.

and mechanical activity showed only a moderate decrease in targeting when compared to WT (Figure 3-7 C and Figure 3-8 B), suggesting that motor activity *per se* may be at least partially dispensable for tip enrichment.

Myo7b cargo-binding tail domain also contributes to tip targeting

The fact that uncoupled Myo7b mutants exhibit near normal localization suggests that actin binding (predicted to be still active in these mutants) and binding partner interactions with the tail domain make significant contributions to tip targeting. To further dissect the relative contributions of motor and tail domains, we examined the targeting potential of truncated constructs consisting of only these regions (Figure 3-2 B). A construct containing only the motor and neck domains (EGFP-MD) was unable to enrich at microvillar tips (Figure 3-7 D and Figure 3-8 C), suggesting that actin binding alone is not sufficient for normal targeting. However, when the cargo-binding tail domain (EGFP-Tail) was expressed by itself, we observed robust tip localization, most likely due to

interactions with endogenous IMAC components or possibly other unidentified binding partners at microvillar tips (Figure 3-7 D and Figure 3-8 C). Thus, the Myo7b cargo-binding tail domain holds significant tip targeting potential.

A forced dimer of Myo7b motor domains uses motor activity to tip target

We next sought to further examine the role of Myo7b motor activity in the absence of potentially confounding effects due to tail domain interactions with endogenous factors. To this end, we fused Myo7b motor and neck domains in frame with a GCN4 dimerization motif (MD-GCN4, Figure 3-2 B) (O'Shea et al., 1991). This 'forced dimer' of Myo7b motor domains exhibited robust tip targeting to a level that was comparable to full-length Myo7b (Figure 3-8 C). Because the Myo7b motor domain exhibits a high duty ratio (Henn and De La Cruz, 2005; Yang et al., 2005), the tip targeting of MD-GCN4 likely reflects barbed-end directed movement along microvillar core actin bundles. Consistent with this conclusion, when we overexpressed EGFP-MD-GCN4 in Cos-7 cells, we observed accumulation at the tips of filopodia; in some cases, we also observed streaming of fluorescent puncta to and from the tips of these structures with tip-ward velocities in the range of ~200 nm/sec (Figure 3-8 E). We also introduced the mutations described above (Figure 3-7 A) into the EGFP-MD-GCN4 construct and generated stable cell lines. Similar to full-length Myo7b, mutations expected to prevent ATPase cycling impaired tip targeting of MD-GCN4 (Figure 3-7 E and Figure 3-8 D). In contrast to experiments with full-length Myo7b, mutations expected to uncouple catalytic and mechanical activity completely inhibited distal tip targeting of the forced dimer (Figure 3-7 E and Figure 3-8 D). Based on these results, we conclude that the Myo7b

motor domain is mechanically active in cells and the minimal unit of a motile complex is two Myo7b motor domains. In combination with the studies presented above, these results tell us that Myo7b motor activity can drive tip targeting, but enrichment at distal tips is likely reinforced by actin binding and binding partner (IMAC or other) interactions with the tail domain.

Complete rescue of Myo7b KD requires functional motor and cargo-binding domains

To further probe the interactions and functions of Myo7b required for IMAC component localization and microvillar clustering, we performed rescue experiments in Myo7b KD CACO-2_{BBE} cells. We were able to rescue expression and distal tip enrichment of IMAC components by stably expressing a full-length Myo7b construct designed to be refractory to KD (Figure 3-9 A and B, EGFP-Myo7bFL). Expression of this construct also rescued microvillar clustering (Figure 3-9 C). The cargo-binding tail construct failed to target to microvillar tips in the absence of endogenous Myo7b and instead accumulated in the cytoplasm (Figure 3-9 A and B, EGFP-Myo7b tail). The forced dimer construct allowed us to disconnect the tip targeting of Myo7b from its interactions with endogenous IMAC cargoes. This construct exhibited robust tip targeting in Myo7b KD cells, but was unable to rescue tip localization of IMAC components (Figure 3-9 A and B, EGFP-Myo7bMD-GCN4), and the level of microvillar clustering was comparable to the Myo7b KD alone (Figure 3-9 C). Finally, we used a variant of full-length Myo7b harboring the I482A mutation (expected to uncouple catalytic and mechanical activity) to analyze the role of motor activity in tip targeting of the IMAC and microvillar clustering.

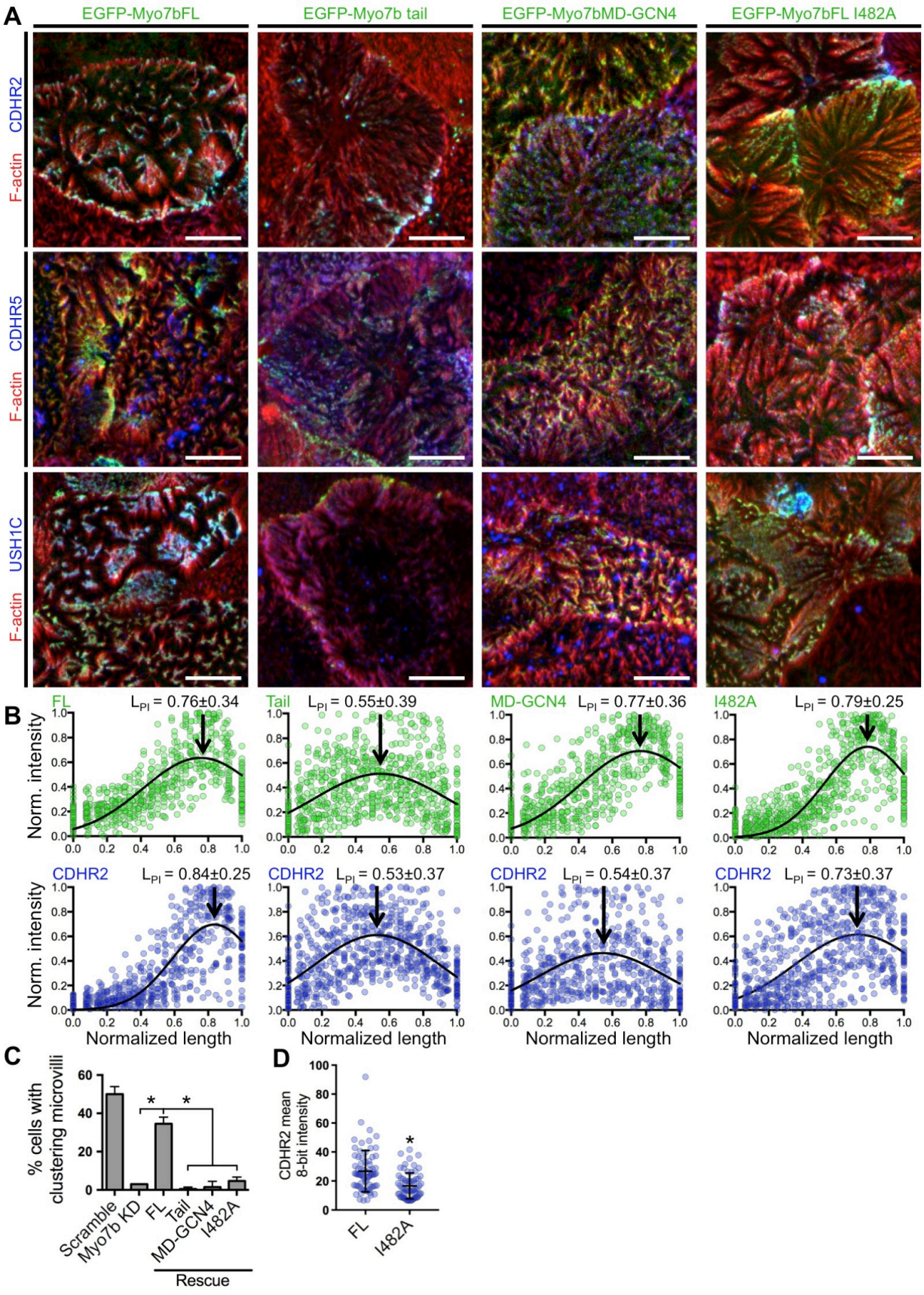
A
EGFP-Myo7bFL
EGFP-Myo7b tail
EGFP-Myo7bMD-GCN4
EGFP-Myo7bFL I482A
CDHR2
F-actin
CDHR5
F-actin
USH1C
F-actin
B
FL
L_{PI} = 0.76±0.34
Tail
L_{PI} = 0.55±0.39
MD-GCN4
L_{PI} = 0.77±0.36
I482A
L_{PI} = 0.79±0.25
CDHR2
L_{PI} = 0.84±0.25
CDHR2
L_{PI} = 0.53±0.37
CDHR2
L_{PI} = 0.54±0.37
CDHR2
L_{PI} = 0.73±0.37
Norm. intensity
Normalized length
C
% cells with clustering microvilli
Scramble
Myo7b KD
FL
Tail
MD-GCN4
I482A
Rescue
D
CDHR2 mean 8-bit intensity
FL
I482A

Figure 3-9. Motor and tail domains are required for complete rescue of Myo7b KD phenotypes. (A) Confocal images of 14 DPC Myo7b KD15 CACO-2_{BBE} cells expressing the EGFP-tagged Myo7b rescue constructs indicated (green), and stained for F-actin (red) and either CDHR2, CDHR5, or USH1C (blue). Scale bars, 5 μm. **(B)** Line scan analysis of Myo7b rescue construct signal (green) and CDHR2 intensity (blue) parallel to the microvillar axis. 0=base and 1=tip. N = 51 scans for each plot. Gaussian curve fits are marked with length at peak intensity (L_{PI}) ± distribution width (SD). **(C)** Quantification of cells with clustering microvilli expressed as a total percentage of cells. Only EGFP-positive (i.e. rescue construct-expressing) cells were scored. Bars indicate mean ± SD. N = 145 cells for FL, 194 cells for Tail, 168 cells for MD-GCN, and 164 cells for I482A. *p<0.0001, t test. **(D)** Mean 8-bit intensity measurements of CDHR2 in gain-matched images of FL rescue (24.7 ± 14.3; n = 72 cells) and I482A rescue (16.6 ± 8.8; n = 67 cells). *p<0.0001, t test. See also Figure S5.

Expression of this construct only partially rescued the distal tip enrichment of IMAC proteins (Figure 3-9 A and B, EGFP-Myo7bFL I482A). However, this mutant was unable to rescue microvillar clustering (Figure 3-9 C). To better understand this disconnect, we examined levels of CDHR2 recruitment to the BB in cells expressing EGFP-Myo7b FL vs. EGFP-Myo7bFL I482A constructs. In gain-matched images, cells expressing the uncoupling mutant exhibited significantly lower CDHR2 levels at the apical surface relative to cells expressing the WT full-length variant (Figure 3-9 D), suggesting that this mutant was unable to rescue the localization of enough CDHR2 to support microvillar clustering. These results indicate that normal Myo7b motor activity is needed for robust, efficient accumulation of CDHR2 to the tips of microvilli, to a level that supports intermicrovillar adhesion.

DISCUSSION

Myo7b plays a role in intermicrovillar adhesion

Tip localization of the IMAC is essential for its function in organizing microvillar protrusions during BB assembly (Crawley et al., 2014b). Initial studies showed that

deletion of the cytoplasmic domain of CDHR2 resulted in a loss of distal tip enrichment, and thus intermicrovillar adhesion (Crawley et al., 2014b). These data were the first to suggest that links to cytoplasmic binding partners were needed to generate and maintain the tip enrichment of IMAC components. Additionally, mice lacking the scaffolding molecule USH1C demonstrated a striking loss of Myo7b from the BB; in these cells, CDHR5 localized along the length of microvilli rather than exhibiting tip enrichment. SEM of these animals also revealed perturbations in BB morphology in regions of both small intestine and colon, further underscoring the importance of IMAC tip enrichment.

The data we present here indicate that Myo7b plays a role in promoting the distal tip enrichment of IMAC components (Figure 3-10). KD of Myo7b in CACO-2_{BBE} cells resulted in decreased microvillar clustering and disruption of BB organization (Figure 3-3 and Figure 3-4), as well as a significant loss of distal tip enrichment of several IMAC components (Figure 3-5 and Figure 3-6). We also observed decreased expression of certain IMAC components, which is most likely explained by mislocalization-induced turnover (Figure 3-5 and Figure 3-6). By concentrating IMAC components at the distal tips, Myo7b focuses the resulting adhesion capacity to a singular point along the microvillar axis; this in turn increases the probability that collisions between adjacent microvilli will lead to productive, organized tipi-like clustering. Tip localized adhesion may also play a role in unifying the length of adjacent microvilli (Crawley et al., 2014b). Although the CACO-2_{BBE} cell culture model requires days to achieve enterocyte-like differentiation, the differentiation that occurs as native enterocytes exit stem cell-containing crypts is likely complete in hours rather than days. Thus, in an *in vivo*

context, Myo7b is probably critical for targeting the IMAC to microvillar tips in a timely manner.

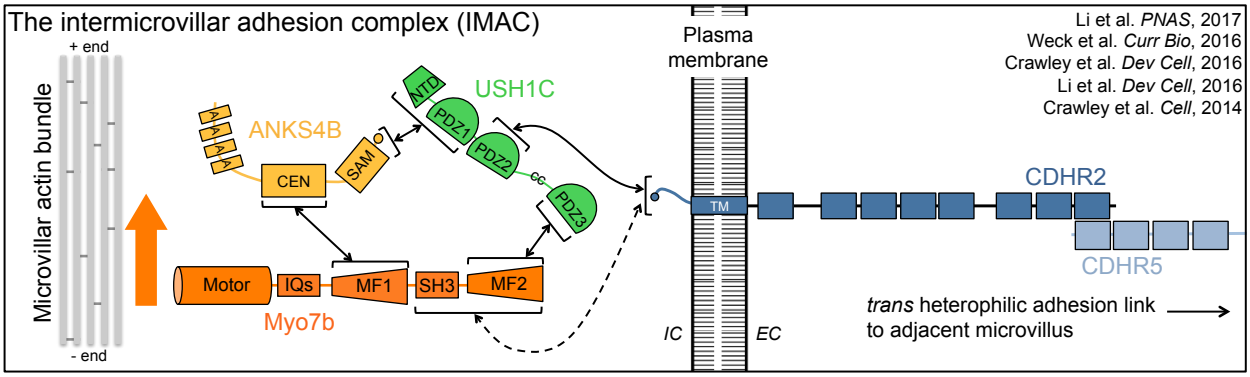

Figure 3-10. Myo7b promotes the distal tip localization of the IMAC. Schematic diagram of the extensive network of interactions within the IMAC. Papers supporting this model are listed. Adapted from (Weck et al., 2016).

Significance of Myo7b motor activity in IMAC localization

The most obvious role for Myo7b motor activity in IMAC localization and function would be in powering transport along the microvillar axis, towards the distal tips. Although the mechanical properties of Myo7b have yet to be characterized *in vitro*, several lines of evidence suggest that Myo7b is an active motor, and that motor activity contributes to cargo enrichment at microvillar tips. First, a forced dimer of Myo7b motors domains, which lacks any cargo-interacting motifs, exhibits robust targeting to microvillar tips (Figure 3-8 C). Second, mutations expected to prevent ATPase cycling or 'uncouple' (i.e. prevent) lever arm rotation abolish targeting of the forced dimer to microvillar tips (Figure 3-8 D). Third, the plus-end directed movement of Myo7b forced dimer puncta can be directly visualized in Cos-7 cell filopodia (Figure 3-8 E). Together, these data suggest that Myo7b mechanical activity is capable of driving transport out to the tips of microvilli.

Although Myo7b motor activity is sufficient for targeting this molecule to microvillar tips, the mechanisms employed by full-length, cargo-binding Myo7b molecules may be more complex. Indeed, our rescue experiments provide information on the requirements for distal tip enrichment of IMAC components and microvillar organization. Whereas full-length WT Myo7b was capable of fully rescuing both tip localization of IMAC cargoes and microvillar clustering, a Myo7b tail fragment or forced dimer of Myo7b motor domains (lacking the tail) were both unable to rescue either readout (Figure 3-9 A and D). Interestingly, a full-length Myo7b construct expressing the I482A mutation (expected to uncouple catalytic and mechanical activity) was able to target to microvillar tips and partially rescue the tip enrichment of CDHR2 (Figure 3-9 A B). These results strongly suggest that one aspect of Myo7b function could be retention of cargoes at microvillar tips, which may not require force generation. However, this mutant failed to rescue microvillar clustering (Figure 3-9 C), most likely because the amount of CDHR2 rescued in this case was significantly reduced relative to WT (Figure 3-9 D). Thus, Myo7b force generation is needed to optimize the efficiency of IMAC accumulation at the distal tips of microvilli, either by enhancing retention or by actively transporting IMAC cargoes to these sites.

How might a Myo7b mutant deficient in motor activity target to microvillar tips and partially rescue CDHR2 localization? One mechanism might involve cooperative interactions between actin binding (still active in uncoupled mutants) and tail-mediated binding partner interactions. Future studies will need to dissect how specific regions of the tail, and interactions with specific IMAC cargoes, contribute to the targeting and function of Myo7b.

Regulation of Myo7b activity

Motor proteins are subject to tight regulation to prevent unnecessary ATP hydrolysis and control both temporal and spatial activation for proper function. One common form of regulation is 'auto-inhibition', where a cargo-binding tail folds back to directly interact with the motor domain and inhibit catalytic and mechanical activity. Release of auto-inhibition typically involves cargo binding to the tail, but can also be caused by calcium-dependent light chain binding or phosphorylation. There is no direct evidence indicating that full-length Myo7b adopts an auto-inhibitory conformation. However, structural studies of closely related Myo7a have shown that the tail domain binds to and inhibits the motor domain (Sakai et al., 2015; Umeki et al., 2009; Yang et al., 2009). If Myo7b is regulated in a similar manner, our data suggest that complete release from any auto-inhibited state may also require ATPase activity and normal actin binding. Indeed, the Myo7b tail domain exhibited the most robust distal tip localization in our targeting assay (Figure 3-8 C), whereas the non-cycling full-length Myo7b mutants were unable to tip target even though they contain an intact tail domain (Figure 3-8 B). Previous studies have demonstrated that actin-binding is sufficient to relieve auto-inhibition of myosin-6, allowing for dimerization, motor clustering, and processive movement (Park et al., 2006). Myo7b may have similar requirements for exiting an auto-inhibited state and achieving full activation in cells.

MyTH4-FERM myosins as transporters in finger-like protrusions

Myo7b shares structural and functional similarities with other MyTH4-FERM myosins including Myo7a, Myo10, and Myo15, each of which has been implicated in anchoring

or transporting cargoes at/to the tips of other actin bundle-supported protrusions (Almagro et al., 2010; Belyantseva et al., 2003; Belyantseva et al., 2005; Berg and Cheney, 2002; Grati and Kachar, 2011; Manor et al., 2011; Sakai et al., 2015; Sakai et al., 2011; Tokuo and Ikebe, 2004; Yang et al., 2006; Zhang et al., 2004). Myo10 is an inducer of filopodial formation and has been implicated in the trafficking of a number of factors that play roles in the growth and stabilization of these protrusions, including VASP and integrins (Bohil et al., 2006; Tokuo and Ikebe, 2004; Zhang et al., 2004). Previous experiments with Myo10 provide compelling evidence in support of barbed-end directed transport, with direct observation of motility at the single molecule level using TIRF microscopy (Kerber et al., 2009). Myo15a also plays a role in the enrichment of specific cargoes at the ends of protrusions, in this case Whirlin (Belyantseva et al., 2005) and EPS8 (Manor et al., 2011) at the tips of stereocilia. *Shaker-2* mice lacking Myo15a are unable to enrich these cargoes at the tips of stereocilia, which are shorter as a result (Belyantseva et al., 2005; Manor et al., 2011). Myo7a, which has been investigated extensively in connection to its role in Type 1 Usher syndrome (Weil et al., 1997), is most closely related to Myo7b in domain structure and organization (Chen et al., 2001). Myo7a is highly expressed in hair cells of the vestibular and cochlear systems, where it contributes to the localization of Sans and other components of the Usher complex (CDH23 and USH1C) at upper tip-link densities (Grati and Kachar, 2011). Together, these factors are essential for tip-link assembly, positioning, and function in mechanotransduction (Pan and Zhang, 2012). Because a number of mutations that give rise to hearing loss are located in the motor domain (Weston et al., 1996), Myo7a likely uses motor activity to position or exert tension on the ends of tip-

links. Mice lacking Myo7a exhibit striking parallels in phenotype relative to the Myo7b KD CACO-2_{BBE} cell lines reported here. *Shaker-1* mice, which lack functional Myo7a, exhibit disorganized bundles of stereocilia and defects in mechanotransduction (Self et al., 1998). Loss of functional Myo7a also disrupts the localization of USH1C at upper tip-link densities (Lefevre et al., 2008). Interestingly, Myo7a contains a single α-helix and short coiled coil, which are noticeably absent in Myo7b. These domains likely mediate the robust filopodial tip targeting and cargo-induced dimerization seen in cultured cells (Sakai et al., 2011).

With our current findings, we now know that all three major classes of actin bundle-supported protrusions take advantage of MyTH4-FERM myosins for their assembly and organization. This role is conserved as Myo7 in *Dictyostelium* targets to the tips of filopodia where it plays a role in their adhesion with extracellular substrates (Tuxworth et al., 2001). The use of MyTH4-FERM myosins to mediate similar functions in diverse systems suggests structural diversification from a common ancestral gene. Indeed, phylogenetic studies indicate that a MyTH4-FERM myosin was one of three actin-based motors present in the cenancestral eukaryote (Richards and Cavalier-Smith, 2005).

Conclusions

Our studies reveal Myo7b as a MyTH4-FERM myosin that targets to the tips of microvilli and promotes the distal tip enrichment of IMAC cargoes, which are essential for normal BB assembly. Beyond the implications for understanding mechanisms of enterocyte differentiation, our results also imply that microvillar core actin bundles may support tip-

directed transport by other myosins normally found in these protrusions. Indeed, myosin-1d and myosin-5 have been show to enrich at both the distal tips and terminal web in the intestinal BB (Benesh et al., 2010; Heintzelman et al., 1994). Additional studies will be needed to determine how these motors contribute to the assembly and maintenance of microvilli. Other future experiments will need to explore the regulation of Myo7b motor and cargo binding activities. While the minimal unit sufficient for tip targeting is a dimer of Myo7b motor domains, the stoichiometry of the complex *in vivo* is unknown. The vast network of protein interactions between Myo7b and other IMAC components could support the formation of a large macromolecular complex, associated with an ensemble of Myo7b motors. Investigating molecular mechanisms of IMAC formation will further develop our understanding of the requirements for proper function and provide additional insight into conserved functions of MyTH4-FERM myosins.

CHAPTER IV

DEVELOPING AN IN-CELL RECONSTITUTION ASSAY TO STUDY IMAC ASSEMBLY AND TRANSPORT

INTRODUCTION

In the previous chapter, we showed that the motor activity of Myo7b is required for targeting WT levels of CDHR2 to the distal tips of microvilli and rescuing microvillar clustering in Myo7b KD cells (Figure 3-9). This suggests that motor activity and force generation are key properties of Myo7b that contribute to its function in brush border assembly. We also demonstrated that a forced dimer of two Myo7b motor domains was sufficient for robust targeting to the tips of microvilli (Figure 3-8 C). However, full-length Myo7b contains no dimerization domains and is predicted to be monomeric. This is in contrast to well-characterized myosin transporters that form dimers through parallel (Myo5; (Liu et al., 2006; Walker et al., 2000)) or anti-parallel coiled coil domains (Myo10; (Lu et al., 2012)). Alternatively, cargo binding to the tail domain of other monomeric myosins, such as Myo6 and Myo7a, has been shown to induce dimerization, bringing two or more motor heads together to form a processive unit (Phichith et al., 2009; Sakai et al., 2011; Yu et al., 2009). Since almost every member of the IMAC interacts with each other, there is an extensive network of interactions that could occur, resulting in a large macromolecular complex of unknown stoichiometry. Therefore, although we showed that a dimer is the minimal unit capable of targeting to the tips of

microvilli, the IMAC *in vivo* may contain several motor heads, multimerizing or oligomerizing Myo7b to enable translocation.

We have shown previously that Myo7b can directly interact with each known member of the IMAC (Crawley et al., 2014b; Crawley et al., 2016). Therefore, one or more of these cargo molecules could dimerize or multimerize Myo7b. Alternatively, multiple cargoes may be required to induce oligomerization of the motor. To test these possibilities, we needed to develop a system with a fast, clear, and easy read out for Myo7b multimerization. Rather than a biochemical or *in vitro* approach, we decided to develop an in-cell assay where monomeric versions of Myo7b are not capable of tip targeting while multimerized Myo7b robustly localizes to the tips of protrusions. This would enable us to analyze the relevance of these interactions in a cellular environment. Using cells would also allow live celling imaging, where we could get information on complex assembly, dynamics, and turnover.

Additionally, we needed to use a heterologous system that enabled precise control over the components of the IMAC that were present and able to interact. These parameters ruled out the use of intestinal and kidney epithelial cells, as all known members of the IMAC are expressed in these cells. Furthermore, these cells produce their microvillar actin-based protrusions on their apical surface in the Z plane of imaging, decreasing our spatial and temporal resolution and efficiency of quantification. We decided to use HeLa human cervical epithelial cells since they are easily transfectable, produce numerous filopodia, and should not express any of the IMAC components. Filopodia are similar to microvilli in that they are membrane protrusions that are supported by a core actin bundle, and are roughly the same size and shape. They also

provide increased resolution and easier quantitation, as they are substrate attached, positioning them in close proximity to the coverslip and in the XY plane for imaging.

However, we do not see robust tip targeting of the Myo7b MD forced dimer in filopodia (Figure 3-8 E), and needed to develop a strategy for clear localization at filopodial tips. To do this, we took advantage of the endogenous motor found at the tips of filopodial protrusions, Myo10. Full-length Myo10 contains an anti-parallel coiled coil in the neck region that enables dimerization upon release of auto-inhibition by lipid binding (Lu et al., 2012; Plantard et al., 2010; Umeki et al., 2011). Many previously published papers have demonstrated that a construct containing only the Myo10 motor domain, neck region, and anti-parallel coiled coil is capable of translocating to the tips of filopodia, independent of any cargo interactions (Bird et al., 2017; Kerber et al., 2009; Lu et al., 2012). We exploited this property of Myo10 and generated EGFP-tagged chimeric motors containing the Myo10 MD fused in frame with the Myo7b cargo-binding tail domain (strategy adapted from (Bird et al., 2017)). Therefore, these constructs have the motile properties of Myo10 but the cargo-binding interactions of Myo7b. We generated two different chimeras: one containing the anti-parallel coiled coil (Myo10MD-CC-Myo7b tail) and one without (Myo10MD-Myo7b tail) (Figure 4-1). We hypothesized that the construct containing the coiled coil would be a constitutive dimer since there would likely be no interaction between the Myo10 MD and Myo7b tail, and thus no auto-inhibition. This construct would serve as a positive control, demonstrating that a dimer of the chimeric motors would be capable of targeting to the tips of filopodia. It would also serve as a positive control for cargo binding since any interacting proteins would be translocated with the motor to filopodial tips. Conversely, we hypothesized that the

construct lacking the coiled coil would be monomeric and unable to target to the tips of filopodia in the absence of a dimerizer. We also hypothesized that upon addition of a cargo protein that mediates multimerization, the Myo10MD-Myo7b tail construct would be capable of translocation to filopodial tips, carrying the cargo responsible for multimerization with it.

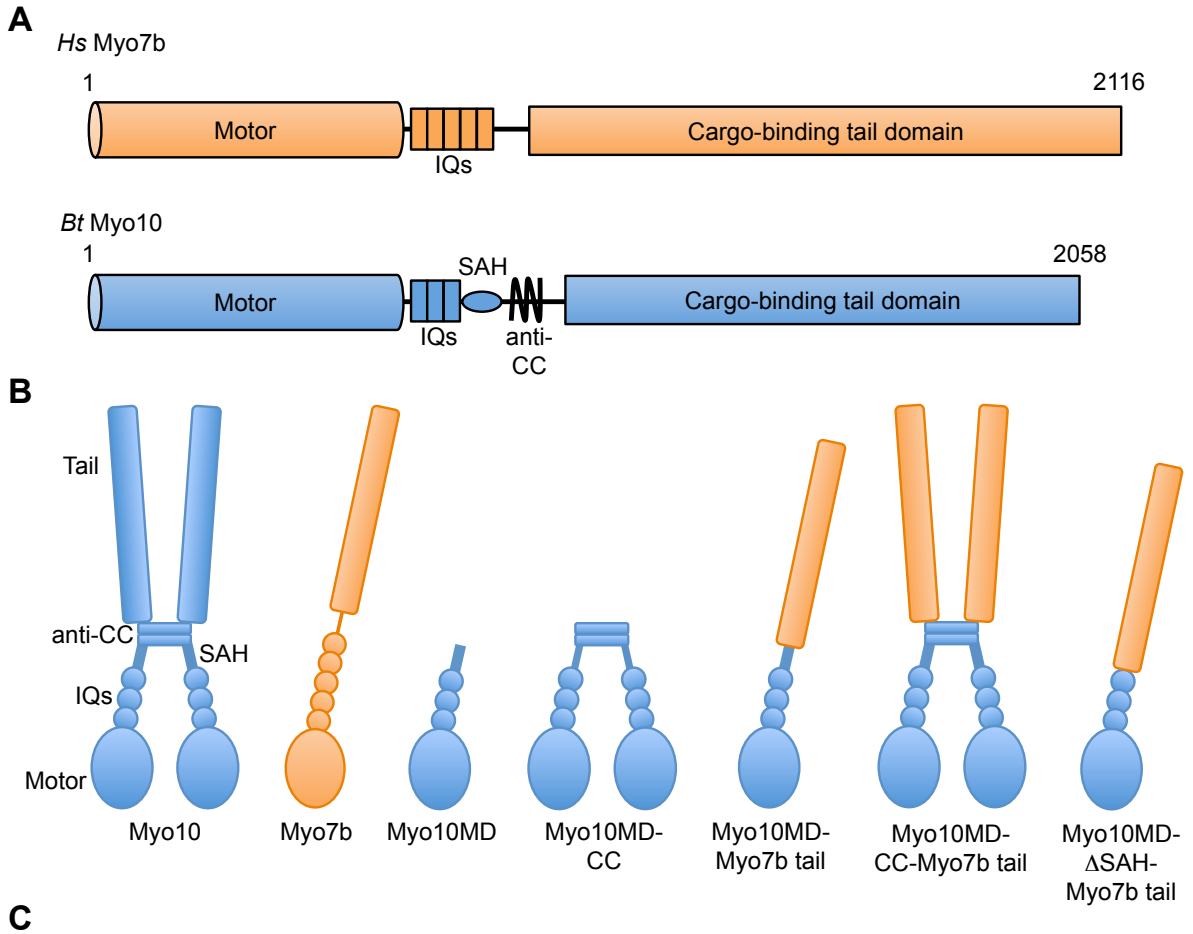

C

Tip targeting?	Myo10	Myo7b	Myo10MD	Myo10MD-CC	Myo10MD-Myo7b tail	Myo10MD-CC-Myo7b tail
Motor	✔	✗	✗	✔	Cargo dependent?	✔
Cargo	✗	✗	✗	✗	✔	✔

Figure 4-1. Construct diagrams and hypothesized outcomes. (A) Domain diagrams of Myo7b and Myo10 used to generate control constructs and chimeric motors. Refer to Figure 1-2 for more detailed diagrams. **(B)** Artistic depictions of motor constructs to indicate predicted dimerization state. **(C)** List of hypothesized outcomes for motor

constructs. Each column refers to a different construct. The first row (motor) indicates whether or not the motor is predicted to be tip targeted. The second row (cargo) shows the predicted localization of the cargo, if responsible for multimerization, when co-expressed with the motor constructs.

RESULTS

'Monomeric' Myo10-Myo7b chimera is still capable of localizing to filopodial tips

To test our hypotheses about the chimeric motors, we transfected HeLa cells with the Myo10MD-Myo7b tail, Myo10MD-CC-Myo7b tail, Myo10MD-CC positive control, or Myo10MD negative control. We re-plated cells the next day onto laminin-coated coverslips, and let them adhere for 24 hours before fixing and staining. Similarly to previously published data, the Myo10MD-CC construct targeted to the tips of filopodia while the Myo10MD negative control remained in the cytosol and showed no enrichment in filopodia (Figure 4-2 A and B). As hypothesized, the Myo10MD-CC-Myo7b tail chimera targeted to filopodial tips, similarly to the Myo10MD-CC positive control construct (Figure 4-2 C). However, the Myo10MD-Myo7b tail construct also targeted to the tips of filopodia, independently of any additional IMAC components (Figure 4-2 D). There are several explanations for why this 'monomeric' construct is capable of tip targeting. Possible reasons include (i) an IMAC component is expressed in HeLa cells facilitating oligomerization of the Myo7b tail, (ii) the Myo7b tail can interact with an unknown protein endogenously expressed in HeLa cells that multimerizes the motor, (iii) the Myo7b tail can interact with an actin-binding protein, membrane protein, or the plasma membrane, limiting diffusion and enabling processive movement, (iv) the Myo7b tail has an uncharacterized dimerization domain, and (v) there is some residual

dimerization of the Myo10MD construct that is exacerbated by fusion to the Myo7b tail. Some of these possibilities will be addressed below.

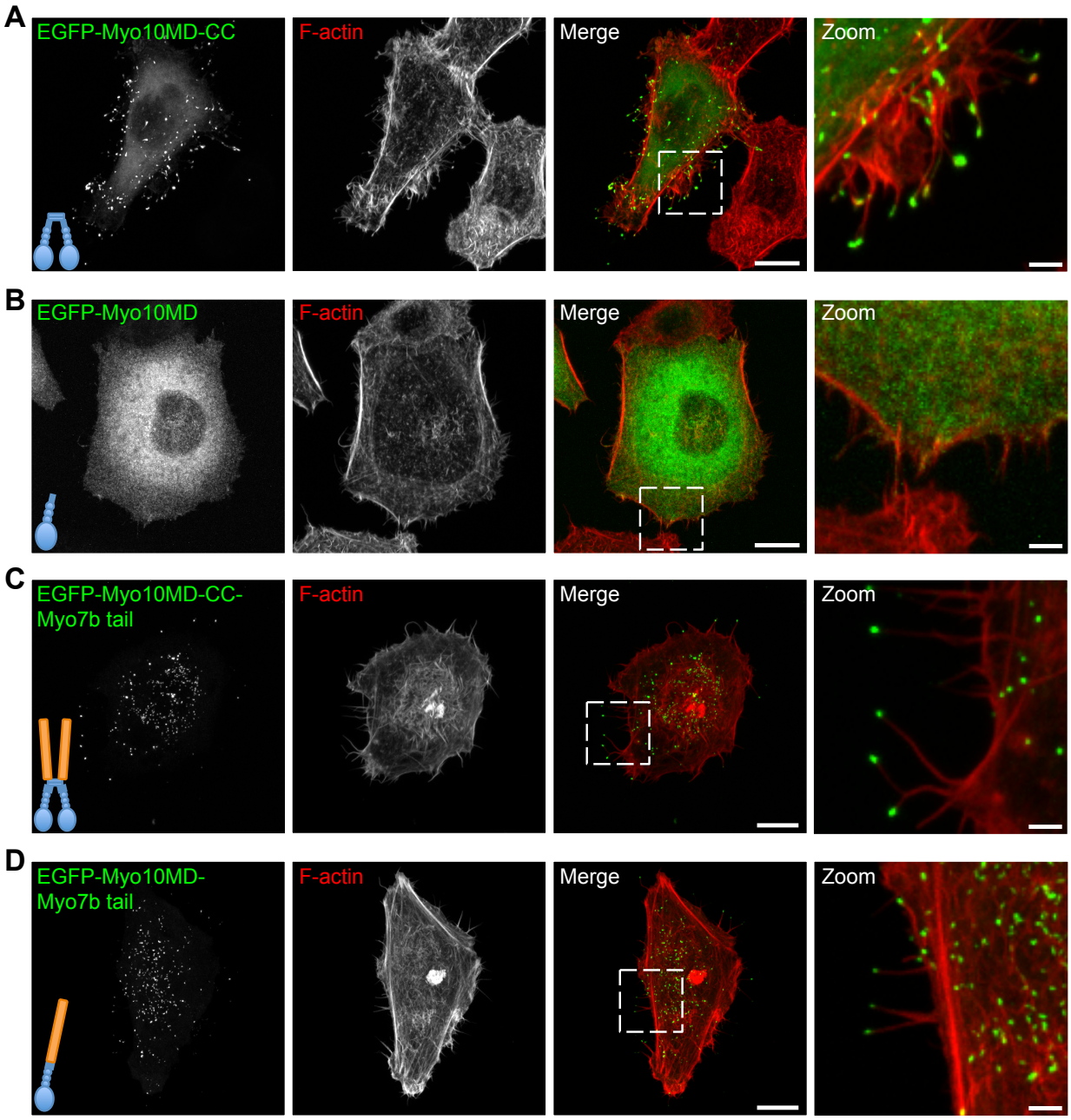

Figure 4-2. Both chimeric motors target to the distal tips of filopodia. (A-D) Confocal images of HeLa cells expressing EGFP-tagged motor constructs (green) and stained for F-actin (red). Boxed areas indicate regions in zoomed images. Scale bars, 10 μm; 2 μm in zooms.

Both chimeric motors transport the IMAC scaffolding proteins to filopodial tips

As a proof of principle, we first wanted to examine the effect of the Myo10-Myo7b chimeric motors on the localization of known binding partners. Strong evidence suggests that Myo7b can directly interact with both scaffolding proteins found in the IMAC. Indeed, crystal structures of ANKS4B and USH1C with the Myo7b tail have been solved (Li et al., 2016; Li et al., 2017; Yu et al., 2017), confirming the biochemical pull-downs published by our laboratory (Crawley et al., 2014b; Crawley et al., 2016). When expressed alone, both ANKS4B and USH1C are soluble, showing no enrichment within filopodial protrusions (Figure 4-3 A). Co-expression with the Myo10-noCC or Myo10-CC controls lacking any cargo interacting domains has no effect on the localization of the scaffolding proteins (data not shown). However, when co-expressed with either chimeric motor, both ANKS4B and USH1C become enriched at the distal tips of filopodia (Figure 4-3 B). Live cell imaging confirmed that the distal tip enrichment of IMAC components is a direct result of motor-based transport, as co-localized puncta moved together toward filopodial tips (data not shown). These data show that the Myo10-Myo7b chimeras are specifically capable of translocating cargo molecules to filopodial tips. This localization is clear and easily distinguishable, leading to a robust system to use for detecting protein-protein interactions between Myo7b and cargo proteins. Incorporation of multiple IMAC components into this system may also be used to study the contributions of individual interactions to complex formation, transport, and turnover.

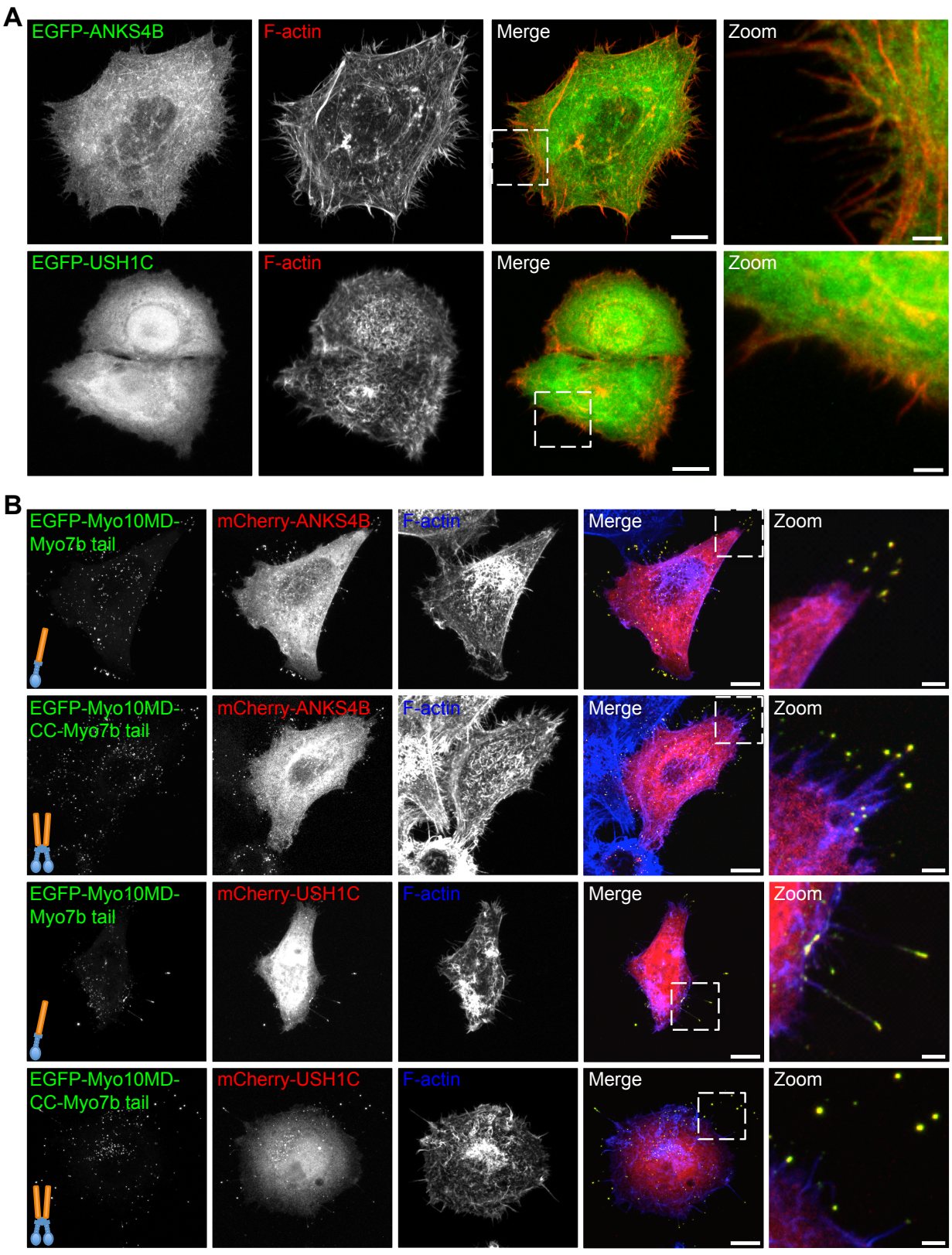

Figure 4-3. ANKS4B and USH1C co-localize with Myo10-Myo7b chimeric motors at filopodial tips. Confocal images of HeLa cells expressing: **(A)** EGFP-tagged ANKS4B

or USH1C alone (green) and stained for F-actin (red); **(B)** EGFP-tagged chimeric motor (green) and either mCherry-tagged ANKS4B or USH1C (red) with F-actin stained (blue). Boxed areas indicate regions in zoomed images. Scale bars, 10 μm; 2 μm in zooms.

USH1C is the only IMAC member expressed in HeLa cells

To address the possible reasons for targeting of the 'monomeric' chimera, we first investigated the possibility that HeLa cells express a member of the IMAC complex. Most of the components, with the exception of USH1C, are almost exclusively expressed in the digestive system and kidney (Chen et al., 2001; Goldberg et al., 2002; Johnston et al., 2004; Okazaki et al., 2002). USH1C is more ubiquitously expressed and is the most likely candidate. USH1C has been suggested to self-associate through head-tail interactions between the PDZ ligand on the C-terminus and the first PDZ domain towards the N-terminus (Adato et al., 2005; Siemens et al., 2002; Yu et al., 2017). This interaction could mediate auto-inhibition or intermolecular interactions leading to chains of higher-ordered oligomers. Additionally, it does have a predicted weak coiled coil domain between the second and third PDZ domains (see Figure 3-10). Therefore, USH1C may dimerize or multimerize, bringing Myo7b motors together to form a processive unit. To determine which components are expressed in HeLa cells, we performed Western blot analysis on whole cell lysates. In comparison to our control cells CACO-2_{BBE}, HeLa cells do not express detectable levels of ANKS4B, CDHR2, CDHR5, or Myo7b (Figure 4-4 A). We then screened for expression of USH1C in some common cell lines used in our laboratory, including LLC-PK1-CL4 kidney epithelial cells, Cos-7 kidney fibroblast cells, and B16F1 mouse melanoma cells. All cell lines expressed some level of USH1C (Figure 4-4 B). We expanded our search for a cell line

that does not express detectable levels of USH1C; however, we were unsuccessful (Figure 4-4 C). Therefore, the contribution of endogenous USH1C to the tip targeting of the 'monomeric' chimera will need to be determined.

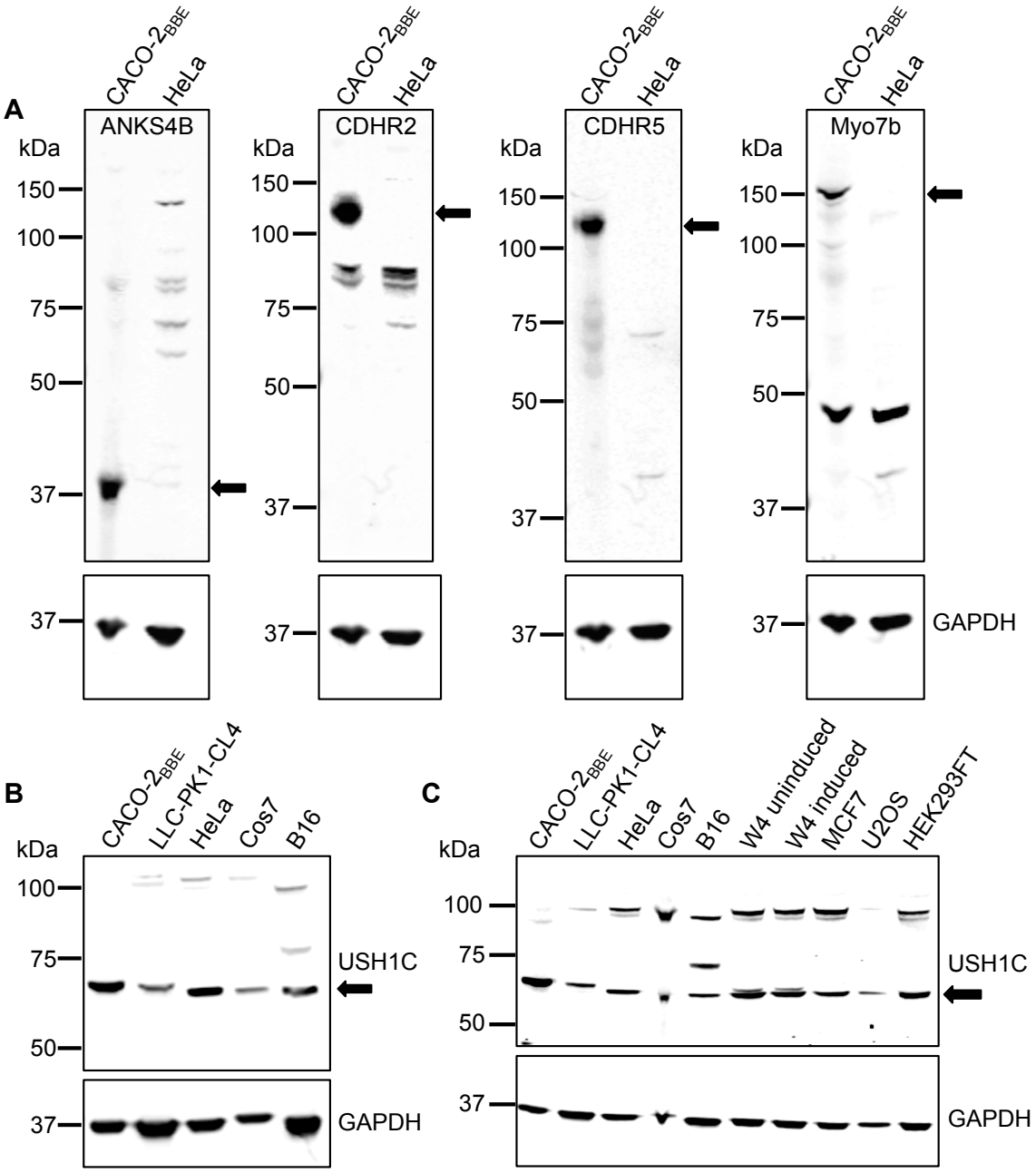

Figure 4-4. Expression of IMAC components in cultured cells. (A) Western blot analysis of endogenous ANKS4B, CDHR2, CDHR5, and Myo7b in HeLa cells compared to the positive control, CACO-2_{BBE} cells. **(B)** Western blot analysis of USH1C expression in commonly used cell lines in the laboratory. **(C)** Broader range of cell lines tested for USH1C expression by Western blot. GAPDH serves as the loading control.

Targeting of the 'monomeric' chimera is independent of USH1C

We began to characterize the role of USH1C in the in-cell reconstitution assay by staining HeLa cells for endogenous USH1C. Compared to a secondary only control, there was a detectable soluble pool of USH1C (Figure 4-5 A). To test if the endogenous USH1C could interact with the chimeric motors, we expressed the Myo10-Myo7b constructs in HeLa cells and then stained for USH1C. The USH1C localization remained unchanged compared to untransfected cells, with no enrichment of USH1C in filopodial protrusions (Figure 4-5 B). Additionally, there was no co-localization between the motors and endogenous USH1C. These data suggest that any endogenous USH1C expressed in HeLa cells does not interact with the chimeric motors and should not affect the in-cell reconstitution assay.

To further examine the role of USH1C in the localization of the 'monomeric' chimera, we utilized a point mutation, K1918E, in the Myo7b tail identified by our colleagues in (Li et al., 2017). This point mutation completely abolishes the interaction between Myo7b and USH1C, as detected by isothermal titration calorimetry. To confirm this, we introduced the K1918E mutation into the Myo10MD-CC-Myo7b tail chimeric motor. Using this construct, we were able to verify that the K1918E mutation inhibits the interaction between USH1C and Myo7b, as USH1C was not localized to the tips of filopodia with this construct (Figure 4-5 C). We next introduced this point mutation into the Myo10MD-Myo7b tail construct to test if the mutation prevents the localization of the 'monomeric' motor. Even with the K1918E mutation, the noCC chimera was still able to target to filopodial tips (Figure 4-5 D). Co-expression with USH1C confirmed that the cargo was not enriched in protrusions (Figure 4-5 D). These data suggest that although

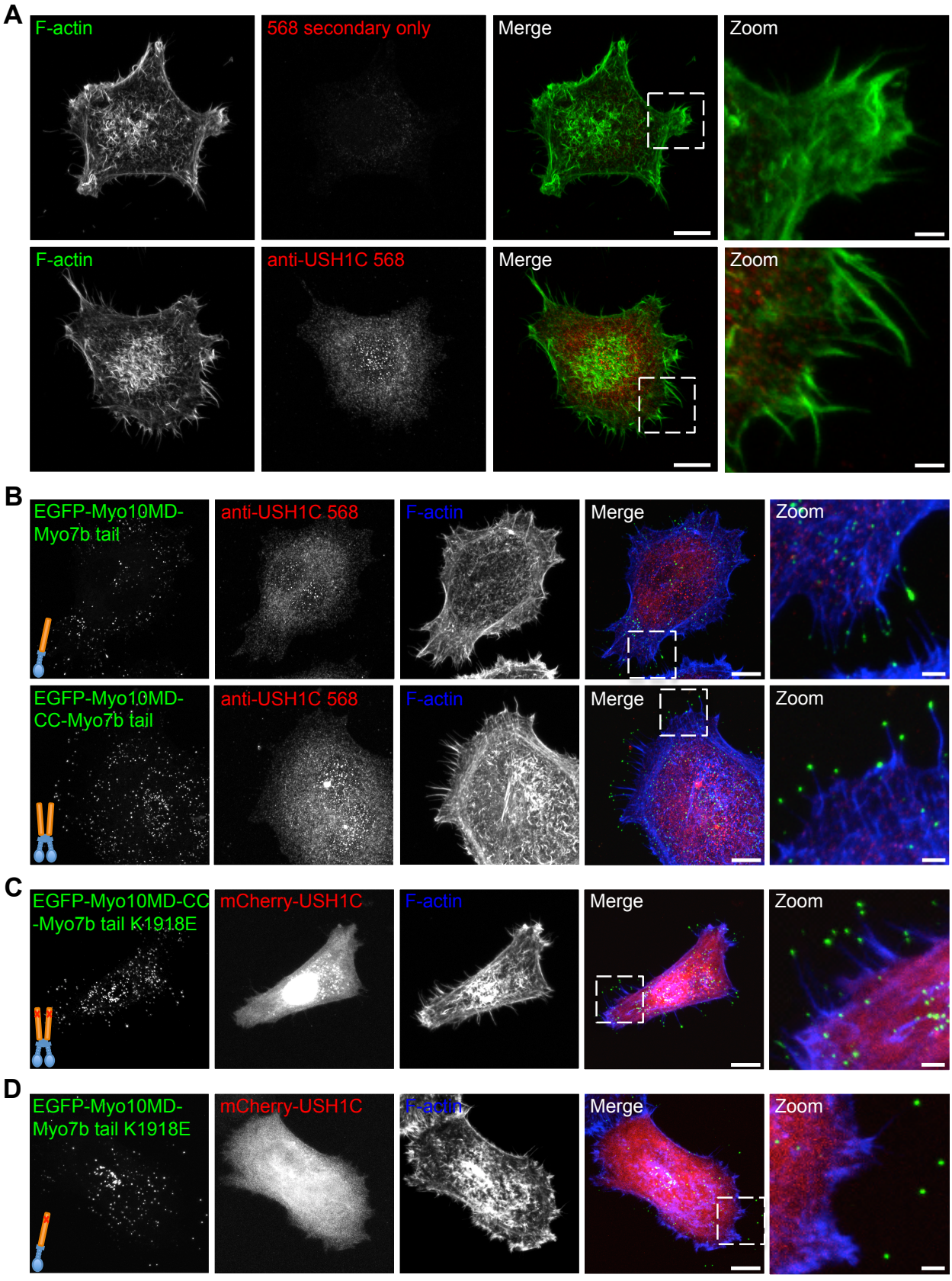
A
F-actin
568 secondary only
Merge
Zoom
F-actin
anti-USH1C 568
Merge
Zoom
B
EGFP-Myo10MD-Myo7b tail
anti-USH1C 568
F-actin
Merge
Zoom
EGFP-Myo10MD-CC-Myo7b tail
anti-USH1C 568
F-actin
Merge
Zoom
C
EGFP-Myo10MD-CC-Myo7b tail K1918E
mCherry-USH1C
F-actin
Merge
Zoom
D
EGFP-Myo10MD-Myo7b tail K1918E
mCherry-USH1C
F-actin
Merge
Zoom

Figure 4-5. Endogenous USH1C does not play a role in the targeting of the 'monomeric' motor. Confocal images of HeLa cells: **(A)** stained for F-actin (green) and secondary antibody background control or endogenous USH1C (red); **(B)** expressing either EGFP-tagged chimeric motor (green) and stained for endogenous USH1C (red) and F-actin (blue); **(C)** co-expressing the EGFP-tagged dimeric chimera (green) and mCherry-tagged USH1C (red), stained for F-actin (blue); **(D)** co-expressing the EGFP-tagged 'monomeric' chimera (green) and mCherry-tagged USH1C (red), stained for F-actin (blue). Boxed areas indicate regions in zoomed images. Scale bars, 10 μm; 2 μm in zooms.

USH1C is endogenously expressed in HeLa cells, it likely does not play a role in the localization of the 'monomeric' chimera. However, any additional experiments using this system to investigate the interactions between IMAC members should take into consideration the endogenous expression and potential contribution of USH1C.

Myo10-Myo7b chimeras enrich CDHR2 and CDHR5 at the distal tips of filopodia

We next wanted to test if Myo7b can directly interact with the adhesion molecules, CDHR2 and CDHR5. Biochemical pull-downs from our laboratory suggested that the Myo7b tail interacts with the cytoplasmic domains of the protocadherins (Crawley et al., 2014b). However, another group has shown the interaction between CDHR2 and Myo7b to be very weak, and suggested it to be physiologically irrelevant (Li et al., 2016). Expression of an EGFP-tagged CDHR2 in HeLa cells results in robust labeling of the plasma membrane, including filopodia (Figure 4-6 A). However, it is uniformly localized throughout the length of the protrusion. Upon addition of either chimeric motor, CDHR2 robustly enriches toward the distal tips of filopodia, indicating that it directly or indirectly interacts with Myo7b (Figure 4-6 B). This interaction is particularly susceptible to influence by USH1C as CDHR2 has a C-terminal PDZ ligand that binds to the second PDZ domain of USH1C (Crawley et al., 2014b; Li et al., 2016). To demonstrate that this

localization is independent of endogenous USH1C, we utilized the K1918E mutated chimeric motor and co-expressed it with CDHR2. The 'monomeric' chimera was still capable of enriching CDHR2 at the distal tips of filopodia, independently of USH1C (Figure 4-6 C).

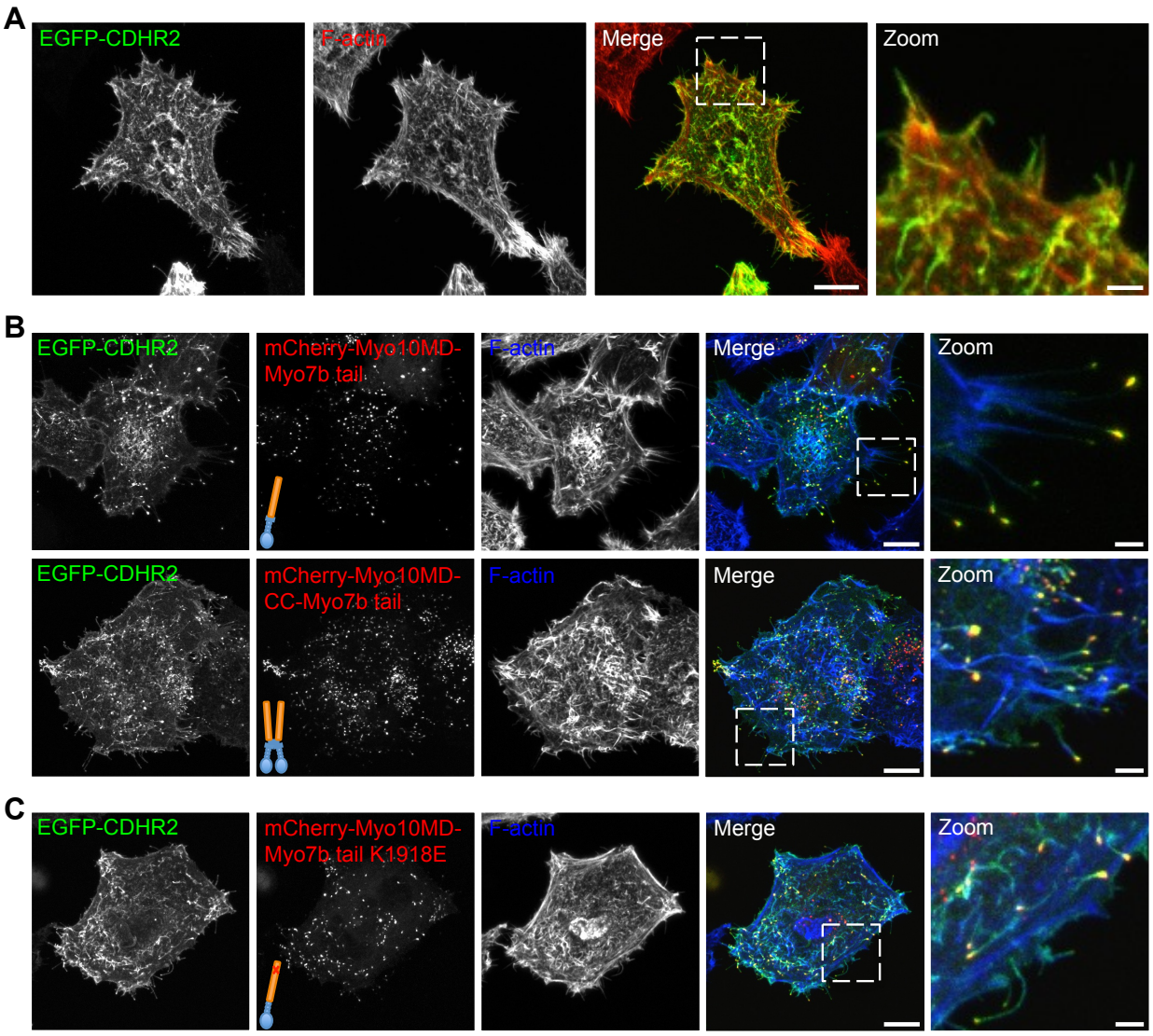

Figure 4-6. The chimeric motors transport CDHR2 to the distal tips of filopodia, independent of USH1C. Confocal images of HeLa cells expressing EGFP-tagged CDHR2 (green) and: **(A)** stained for F-actin (red); **(B)** mCherry-tagged chimeric motors (red) and stained for F-actin (blue); **(C)** mCherry-tagged 'monomeric' chimera with the K1918E mutation (red) and stained for F-actin (blue). Boxed areas indicate regions in zoomed images. Scale bars, 10 μm; 2 μm in zooms.

We next examined the localization of mCherry-tagged CDHR5 in HeLa cells. Both CDHR2 and CDHR5 are heavily post-translationally modified. While CDHR2 is efficiently trafficked to the membrane in HeLa cells, a large portion of CDHR5 gets trapped in intracellular vesicles (Figure 4-7 A). However, a fraction of CDHR5 does properly traffic to the plasma membrane. Similarly to CDHR2, it localizes within protrusions, but it is not enriched (Figure 4-7 A). However, upon addition of the Myo10-Myo7b constructs, CDHR5 becomes enriched at the distal tips of filopodia and co-localizes with the chimeric motors (Figure 4-7 B). Taken together, these results show that Myo7b can directly interact with both microvillar protocadherins.

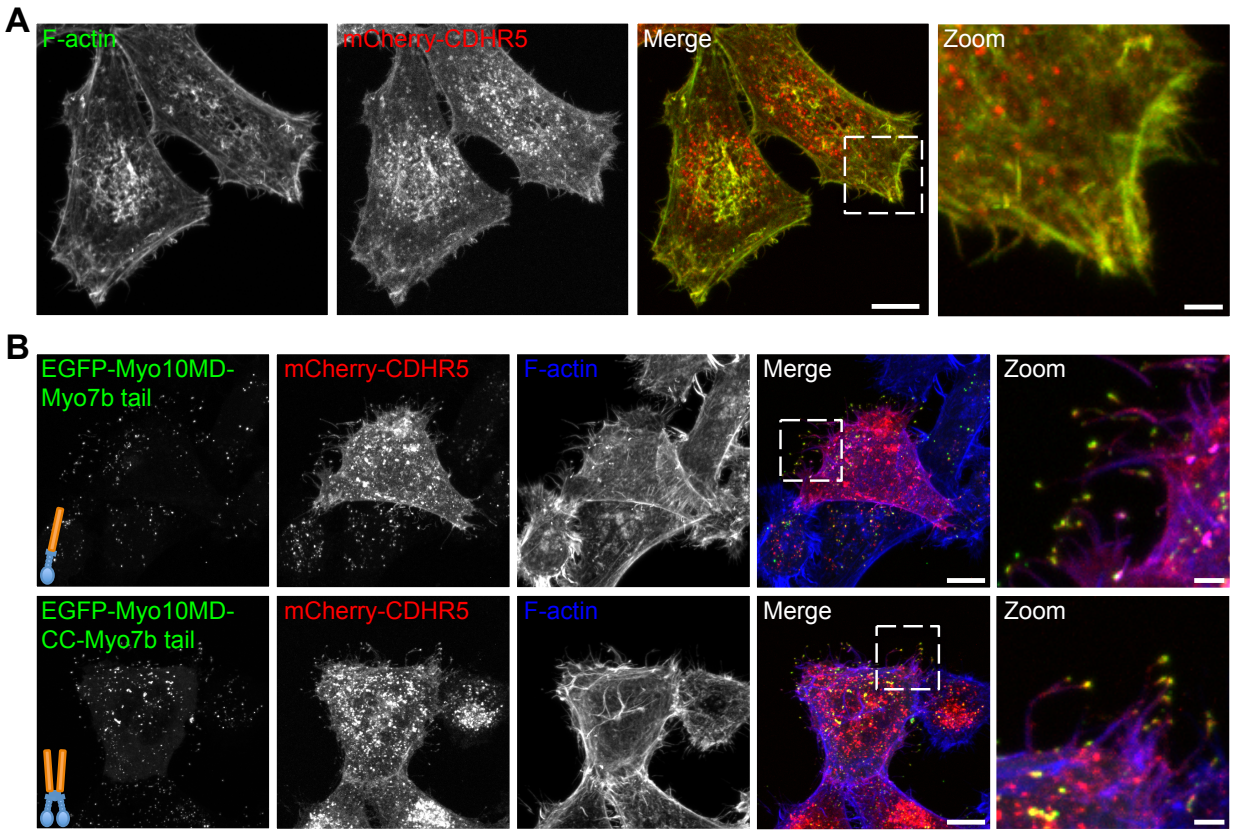

Figure 4-7. Myo10-Myo7b chimeras transport CDHR5 to the distal tips of filopodia. Confocal images of HeLa cells expressing mCherry-tagged CDHR5 (red) and: **(A)** stained for F-actin (green); **(B)** EGFP-tagged chimeric motors (green) and stained for F-actin (blue). Boxed areas indicate regions in zoomed images. Scale bars, 10 μm; 2 μm in zooms.

Residual dimerization of the Myo10 neck does not contribute to tip targeting of the 'monomeric' chimera

To eliminate the possibility of residual dimerization in the Myo10 neck region, we generated another chimeric motor containing the minimal requirements for a functional motor domain. This included just the motor domain and three IQ motifs, which are required for light chain binding and lever arm stabilization. Compared to the previous 'monomeric construct, we deleted the single α-helix (SAH) domain (Myo10MD-ΔSAH-Myo7b tail; Figure 4-1 A and B). This region is thought to act as an extension of the lever arm, leading to Myo10's large step size (Knight et al., 2005; Ropars et al., 2016). Although not predicted to dimerize, this region could be contributing to any residual targeting of the construct. However, when we expressed this construct alone in HeLa cells, it was still able to target to the distal tips of filopodia, though less efficiently (Figure 4-8 A). This is probably a result of the decreased lever arm and step size. Even with the decreased efficiency, the Myo10MD-ΔSAH-Myo7b tail chimera was still capable of translocating IMAC components to filopodial tips (Figure 4-8 B). We concluded that any dimerization of the constructs is mediated through the Myo7b tail. The remaining possible reasons for targeting of the 'monomeric' chimera still need to be explored.

DISCUSSION

In-cell reconstitution assay benefits and pitfalls

We have established an effective and robust assay to detect protein-protein interactions between the tail of Myo7b and potential binding partners in cells. Most protein-protein interactions are detected by *in vitro* approaches with purified proteins, often using

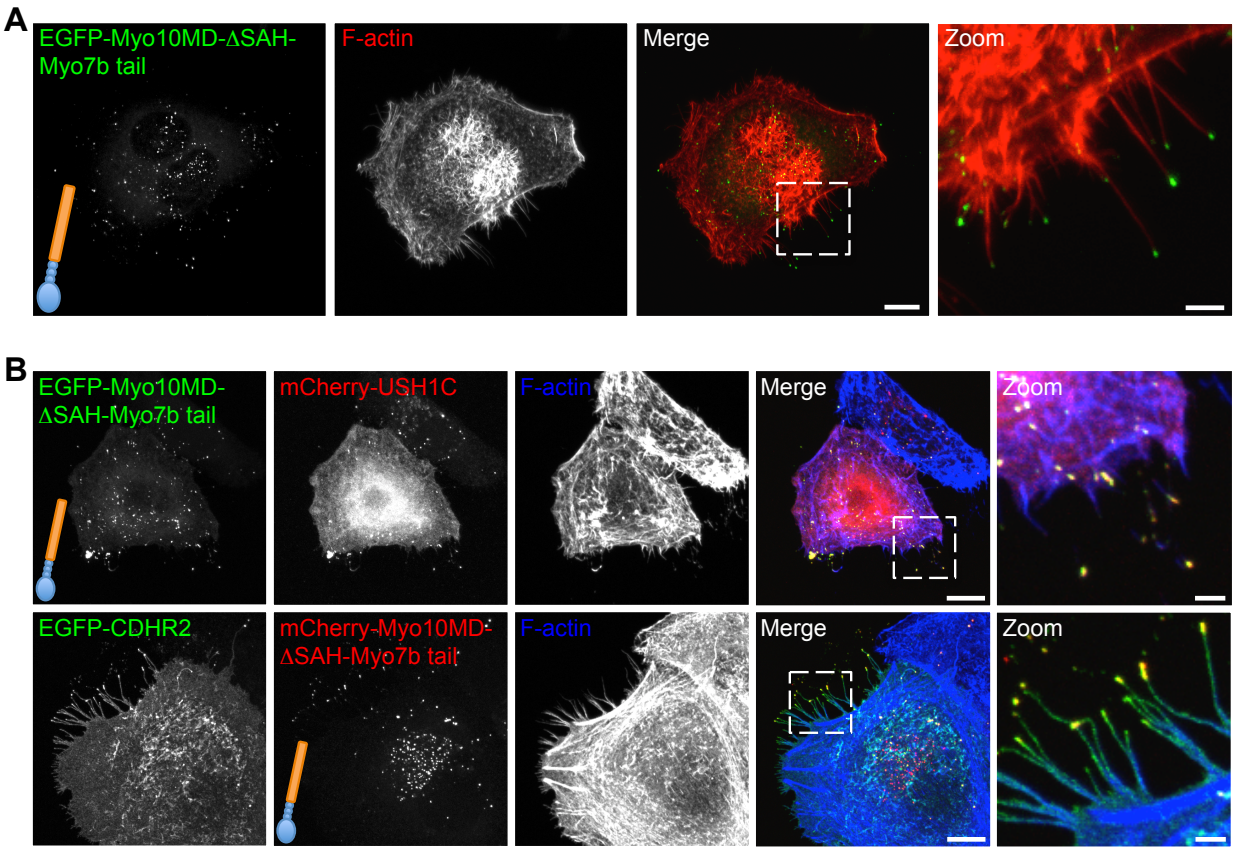

Figure 4-8. Deletion of the SAH does not affect the localization of the 'monomeric' chimera. Confocal images of HeLa cells expressing: **(A)** EGFP-tagged ΔSAH chimera (green) and stained for F-actin (red); **(B)** fluorescent protein-tagged ΔSAH chimera (as indicated) and either mCherry-tagged USH1C (red) or EGFP-tagged CDHR2 (green), and stained for F-actin (blue). Boxed areas indicate regions in zoomed images. Scale bars, 10 μm; 2 μm in zooms.

individual domains. Alternatively, biochemical pull-downs are done after cell lysis, usually with protein fragments. The power of the in-cell reconstitution assay is that it is more similar to *in vivo* conditions as the interactions are occurring and detected in a cellular environment. This technique is capable of detecting relevant interactions in cells that traditional *in vitro* structural assays cannot. Additionally, you can use full-length proteins as well as individual domains. As Myo10 is ubiquitously expressed and localizes to the tips of filopodia in numerous cell types, many available cell lines can be

employed for this assay. Overexpression of Myo10 induces filopodia formation and elongation (Berg and Cheney, 2002; Bohil et al., 2006) so even cells that do not have robust filopodia can be used. As opposed to other in-cell protein-protein techniques, such as FRET, the readout is very robust, making it easy to detect and quantify. In addition to confirming the interactions with the IMAC members, this assay could be used to identify and/or confirm new binding partners for the Myo7b tail. Additionally, deletion constructs of the Myo10-Myo7b chimeras could map which Myo7b tail domain is responsible for specific interactions.

Of course like all techniques, there are limitations to this assay. First, endogenously expressed proteins could convolute the results, even when using an exogenous system. When studying individual protein interactions, expression of both the bait and prey proteins should be analyzed in the cell line. Additionally, you cannot know for certain that all interacting proteins have been identified. For example, there could be an unidentified protein endogenously expressed in HeLa cells that can interact with both Myo7b and CDHR2, mediating the interaction between the two. These concerns are similar to other cell-based assays such as pull-downs. Another concern is the use of fluorescent proteins. These probes are typically bigger and bulkier than tags used for purification, and could interfere with protein interactions. Despite these drawbacks, the in-cell reconstitution assay will be useful for addressing several outstanding questions about IMAC biology, discussed below.

Endogenous USH1C does not interfere with our in-cell reconstitution assay

Despite expression of USH1C in HeLa cells, as detected by Western blot and immunofluorescence, it does not appear to affect any aspect of the in-cell reconstitution assay examined so far. However, all future experiments will need to consider the endogenous expression of USH1C. To get around this, experiments can take advantage of the K1918E mutation in the Myo7b tail. This specifically abolishes the interaction between Myo7b and USH1C, keeping all other known interactions in tact. However, this mutation has its own limitation in screening for new interacting partners for the second MF domain. Binding to proteins that have similar or overlapping interactions with this region may also be affected by this mutation.

Distal tip enrichment of the 'monomeric' chimera

One potential reason why the Myo10MD-Myo7b tail construct that does not contain the coiled coil domain can still target is because the tail of Myo7b can bind to an actin-binding protein, the plasma membrane, or a membrane-bound protein. Other myosins localize to the tips of protrusions through these mechanisms. These interactions have been proposed to act as a 'crutch', limiting diffusion away from the actin bundle. This enables the motor to detach and undergo its recovery stroke while staying in close proximity to the track, resulting in a processive, monomeric motor. Myo3b directly binds to espin, an actin-binding and bundling protein (Liu et al., 2016; Merritt et al., 2012). This interaction is required for the translocation of Myo3b to the tips of stereocilia and filopodia (Ebrahim et al., 2016; Liu et al., 2016; Merritt et al., 2012). Myo10 binds to both the plasma membrane and membrane-bound proteins (Almagro et al., 2010; Hirano et

al., 2011; Lai et al., 2015; Liu et al., 2012; Pi et al., 2007; Plantard et al., 2010; Umeki et al., 2011; Wei et al., 2011; Zhang et al., 2004; Zhu et al., 2007). A recent paper demonstrated that a monomeric form of Myo10, through an internal deletion of the anti-parallel coiled coil, is still capable of translocating to the tips of filopodia (Baboolal et al., 2016). Since our chimeric constructs use the Myo10 motor domain, it is feasible that any of these interactions would mediate enrichment at filopodial tips. The Myo7b cargo-binding tail domain is cytosolic when expressed in HeLa cells alone (data not shown). This would eliminate these possibilities, as it should localize to actin-rich structures or the membrane. However, a previous paper from our laboratory showed that the full-length Myo7b tail is auto-inhibited (Crawley et al., 2016), possibly preventing these interactions. Fusion of the tail to the Myo10 MD could prevent this auto-inhibition, enabling the chimera to interact with the 'crutch' molecule/s and localize to filopodial tips. In fact, the tail of the closely related motor Myo7a was shown to directly interact with membranes containing phosphatidylinositol lipids (Bahloul et al., 2010). However, this has yet to be explored for Myo7b.

Alternatively, there could be an unidentified molecule in cells that can multimerize Myo7b. This protein could be specific to HeLa cells or be more broadly expressed. As opposed to an unidentified cargo, the Myo7b tail itself could have an uncharacterized dimerization domain. This would be a novel interaction as no known myosin motor has a domain in the cargo-binding region that self-associates. Future studies should address these possibilities, and potential experiments will be discussed in the Future Directions Chapter.

Interaction between Myo7b and the microvillar protocadherins

Our experimental results suggest that Myo7b can directly interact with CDHR2 and CDHR5. The cytoplasmic domains of these protocadherins are small, limiting the possible methods of binding. Additionally, both the N- and C-terminal MF domains of Myo7b are occupied by ANKS4B and USH1C, respectively (Li et al., 2016; Li et al., 2017; Yu et al., 2017). Although it is possible for overlap, the interactions between the scaffolding proteins and Myo7b are relatively high, about 1 micro molar (Li et al., 2016; Li et al., 2017; Yu et al., 2017). This likely means that the MF domains are occupied within the IMAC, leaving only the SH3 domain available for interactions. Both CDHR2 and CDHR5 contain multiple PxxP motifs that are putative binding sites for the SH3 domain of Myo7b. Future studies will need to determine if indeed the Myo7b SH3 domain is responsible for interactions with the protocadherins. Additionally, mapping of the PxxP motif with the strongest binding to the Myo7b SH3 domain will be valuable. These details can be used to create point mutations that disrupt this interaction to elucidate its role in complex formation and function.

Although this interaction is sufficient for this assay, we know the scaffolding proteins are required for proper complex localization and function in CACO-2_{BBE} intestinal epithelial cells and *in vivo* (Crawley et al., 2014b; Crawley et al., 2016). This leads to puzzling questions about the relevance of this interaction and the biology of the complex. These systems may simply be more sensitive to perturbations than HeLa cells. Additionally, we may be missing an unidentified protein that is mediating this interaction in HeLa cells that is not present in the other systems. More interestingly, in microvillar protrusions with full-length Myo7b, the complex may require the scaffolding

proteins to regulate Myo7b activity. They may control the number of motors in a complex, requiring more than two to form a stable, functional transport unit. This is different than the in-cell reconstitution assay, as we know that Myo10 can be processive as a monomer and dimer. Alternatively, these molecules may be required for release of auto-inhibition in full-length Myo7b. Although auto-inhibition of full-length Myo7b has yet to be determined, auto-inhibition of the closely related Myo7a has been established (Sakai et al., 2015; Yang et al., 2009). The chimeric Myo10-Myo7b motor likely does not exhibit auto-inhibition, as the Myo7b tail sequence differs from the Myo10 tail. Therefore, if the scaffolds regulate auto-inhibition in some way, they would not be required for the in-cell reconstitution assay.

Using the in-cell reconstitution assay to address IMAC questions

Unfortunately, the in-cell reconstitution assay cannot be used to address the fundamental question it was originally designed for: which IMAC components are responsible for multimerizing Myo7b into a transport unit? However, it is suitable for addressing other questions about IMAC biology. First, as mentioned above, it can be used to map the interaction between Myo7b and the microvillar protocadherins. An internal deletion of the Myo7b SH3 domain or point mutations of conserved residues can be used to determine if this domain is responsible for these interactions. Additionally, point mutations of the PxxP motifs in the cytoplasmic domains of the protocadherins can be used to address the same question. Separate from the IMAC components, this assay can be used to confirm any putative binding partners identified using other assays (discussed in the Future Directions Chapter). In addition to binary

protein interactions, the assay could be used to look at more complex relationships by adding a third or fourth component of the IMAC. For instance, how does the addition of either or both of the scaffolding proteins affect the localization and function of the complex? Then, we can use point mutations to disrupt a specific interaction within the IMAC to further understand the contribution of each binary interaction to complex formation.

Finally, the assay can be used to look at protein turnover by doing fluorescence recovery after photobleaching (FRAP) experiments. Mature enterocytes maintain their brush border throughout the lifetime of the cell. However, there are constant perturbations to the system, requiring maintenance of the structure. Additionally, protein interactions are dynamic with proteins being turned over and recycled. The stability and lifetime of the IMAC and its individual components are unknown. We could begin to address these and other interesting questions by using FRAP in this assay. We can also start to define the roles of the scaffolding proteins in this system. If they are not required for the interaction between Myo7b and the protocadherins, then what affect do they have on the stability and turnover of the complex? As discussed above, they may regulate complex stoichiometry, changing the dynamics of the IMAC. Apart from the IMAC, the in-cell reconstitution assay can also be used to study other protein-protein interactions and complexes. Using the approaches described above, the assay can address a wide range of questions about complex interactions, formation, regulation, function, and lifetime.

CHAPTER V

TIP-ENRICHED ADHESION LEADS TO LENGTH MATCHING AND STABILIZATION OF ACTIN-BASED PROTRUSIONS

INTRODUCTION

In the intestine, the size of microvilli varies along the length of the intestinal tract (~1-3 μm), with the longest microvilli at the start in the duodenum and the shortest in the colon (Bastie et al., 1982; Boyne et al., 1966; Diamond et al., 1984; Fisher and Parsons, 1950; Leblond, 1981; Mayhew, 1987, 1990; Mayhew and Middleton, 1985; Stenling et al., 1984). Additionally, the length of microvilli varies along the crypt-villus axis, with the shortest microvilli at the base of crypts and the longest at the tips of villi (Brown, 1962; Leblond, 1981; Stenling and Helander, 1981; van Dongen et al., 1976). Regardless of these differences, mature enterocytes produce hundreds of microvilli that are remarkably uniform in length. This creates a flat surface of the cell, which likely helps prevent bacterial attachment. Despite knowing this for decades, how the length of microvilli is regulated is unknown and largely unstudied.

Cells regulate the size of other organelles and protrusions. Well-studied examples of this include the mitotic spindle and flagella/cilia. These organelles are thought to use a combination of mechanisms to control their length, incorporating both direct and indirect size sensing (Chan and Marshall, 2012). Direct size sensing requires a dedicated reporter molecule that provides a readout for the cell. Indirect size sensing involves measuring the functional capacity of the organelles or scaling behavior with cell size. In the absence of size sensing, cells can control size by synthesizing a limited pool

of precursor (Goehring and Hyman, 2012), discussed in further detail below for actin-based structures.

Regulation of actin structures within the cell through actin allocation is an emerging model in the field. Recent studies propose that the G-actin pool is a limiting resource and competition between F-actin networks regulate their size and density (reviewed in (Suarez and Kovar, 2016)). In yeast, inhibition of the Arp2/3 complex and its associated endocytic actin patches results in a significant increase in the formin-mediated networks, actin cables and contractile rings (Basu and Chang, 2011; Burke et al., 2014; Nakano et al., 2010). Conversely, inhibition of formins and their associated structures leads to an increase in Arp2/3 complex-mediated actin patches (Burke et al., 2014; Jose et al., 2015; Willet et al., 2015). This model also applies to insect and mammalian cell culture systems, looking at the competition for actin monomers between the Arp2/3 complex-mediated branched actin network of the lamellipodium and the formin- and/or Ena/VASP-mediated filopodial structures (Henson et al., 2015; Hotulainen and Lappalainen, 2006; Ingerman et al., 2013; Koestler et al., 2013; Murugesan et al., 2016; Rogers et al., 2003; Rotty et al., 2015; Sarmiento et al., 2008; Suraneni et al., 2015; Wu et al., 2012a; Yang et al., 2012). These studies demonstrated that inhibition or depletion of the Arp2/3 complex led to a decrease in the lamellipodial structure and an increase in filopodia formation, elongation, or retrograde flow. Indeed, using the Ls173T-W4 intestinal cell culture model where single cells are induced to form a brush border, microvillar protrusions did elongate upon treatment with an Arp2/3 complex inhibitor (Grega-Larson et al., 2015). Expanding studies to monolayer-forming systems, like CACO-2_{BBE} cells, and *in vivo* mouse models will be essential in

establishing a role for G-actin competition in mediating length control in the brush border.

The intermicrovillar adhesion complex is ideally located to control microvillar length as it is at the distal tips of these protrusions. Interestingly, components of the stereocilia tip-link complex have been shown to play a role in length regulation (Caberlotto et al., 2011a; Caberlotto et al., 2011b). Additionally, KD of CDHR2 in CACO-2_{BBE} cells resulted in microvilli with highly variable lengths, suggesting the IMAC plays a role in length uniformity (Crawley et al 2014). This could be a direct mechanism with downstream signaling activating or inhibiting actin-regulatory proteins. Changing actin dynamics within microvilli could alter the polymerization or disassembly rates of the core bundle, thereby regulating the length. Alternatively, it could be an indirect mechanism through which the adhesion acts as a physical constraint to prevent the elongation of neighboring protrusions. Freeze-etch EM images showed a dense meshwork of adhesion proteins between microvilli, revealing extensive crosslinking by the IMAC (Figure 1-3) (Crawley et al., 2014b). Linkage of the adhesion to the underlying cytoskeleton by Myo7b and lateral links formed by Myo1a could transduce the force from the membrane to the core bundle.

The IMAC is thought to mainly consist of a *trans* heterophilic interaction between CDHR2 and CDHR5 (Crawley et al., 2014b). This was demonstrated by using a bead aggregation assay, a classic technique to look at the adhesion capacity of cadherins. Large clusters of beads formed when beads coated with the extracellular domain of CDHR2 or CDHR5 were mixed together. CDHR5 did not demonstrate any homophilic adhesion, as CDHR5-coated beads alone did not aggregate. However, small clusters of

beads developed when the CDHR2 beads were mixed independently, indicating that CDHR2 is capable of a weak homophilic interaction (Crawley et al, 2014). The extent of the contribution of this homophilic adhesion to the function of the IMAC is unknown. The construct of CDHR2 previously used to abolish adhesion was a domain deletion of the first extracellular cadherin (EC) repeat (Crawley et al 2014), likely eliminating both hetero- and homophilic interactions. Little is known about the structures of the EC domains of CDHR2 and CDHR5 or how they interact in hetero- or homophilic complexes. We are currently working on these questions in collaboration with a crystallography laboratory.

In the previous chapter, we demonstrated that the chimeric Myo10-Myo7b motors are capable of directly interacting with and translocating CDHR2 and CDHR5 to the distal tips of filopodia. Knowing that CDHR2 is capable of homophilic interactions, we wanted to more closely examine cells with CDHR2 enriched at filopodial tips. Given the importance of tip targeting in the function of the IMAC, we were particularly interested in understanding the morphological impact of enriching adhesion factors at the distal tips of protrusions. Live cell imaging using TIRFM revealed bending of filopodia and adhesion between adjacent protrusions. This led to the stabilization of protrusions and length matching of adherent filopodia. Using structured illumination microscopy (SIM), we were able to show that tip enrichment of CDHR2 resulted in filopodial bundling, with two or more protrusions robustly adhering to one another. Additionally, with the greater resolution in Z, we were able to clearly see adhesion between filopodial protrusions that were standing upright, sticking up off of the dorsal surface of the cell, similarly to microvilli. Finally, we showed that induction of the interaction between the motor and

CDHR2 results in robust induction of filopodia formation and elongation. We are currently working on using this induction to study filopodial dynamics upon adhesion and the factors required for these phenotypes.

RESULTS

Tip-enrichment of CDHR2 by the Myo10-Myo7b chimeric motor leads to bending and adhesion of filopodia

Using the system developed in Chapter IV, we expressed EGFP-tagged CDHR2 alone or with mCherry-tagged Myo10MD-Myo7b tail in HeLa cells. Live cell imaging using TIRFM revealed significant morphological differences. CDHR2 only expressing cells had normal filopodial morphology with straight, highly dynamic protrusions (Figure 5-1 A; left). Conversely, filopodia in cells with tip-enriched CDHR2, resulting from co-expression with the chimeric motor, exhibited a bent morphology (Figure 5-1 A; right), sometimes leading to significant curvature (Figure 5-1 B; arrowheads). This resulted in individual protrusions colliding and adhering with neighboring filopodia (Figure 5-1 B; arrows). With time, adhesion between protrusions led to length matching. This can be seen in the time series montage in Figure 5-1 B, indicated by the arrows. An individual protrusion grows into and adheres to preexisting filopodia (45-95 sec). It continues growing along the preexisting filopodia until it reaches the distal tip (145-295 sec). Another striking phenotype was the presence of bifurcated filopodia (Figure 5-1 B; asterisk), which is rarely seen in control cells. Additionally, protrusions become stabilized with many lasting the entire length of acquisition, about 20 minutes (data not

shown). These data suggest that the tip-enrichment of CDHR2-based adhesion has significant consequences on the morphology and dynamics of filopodial protrusions.

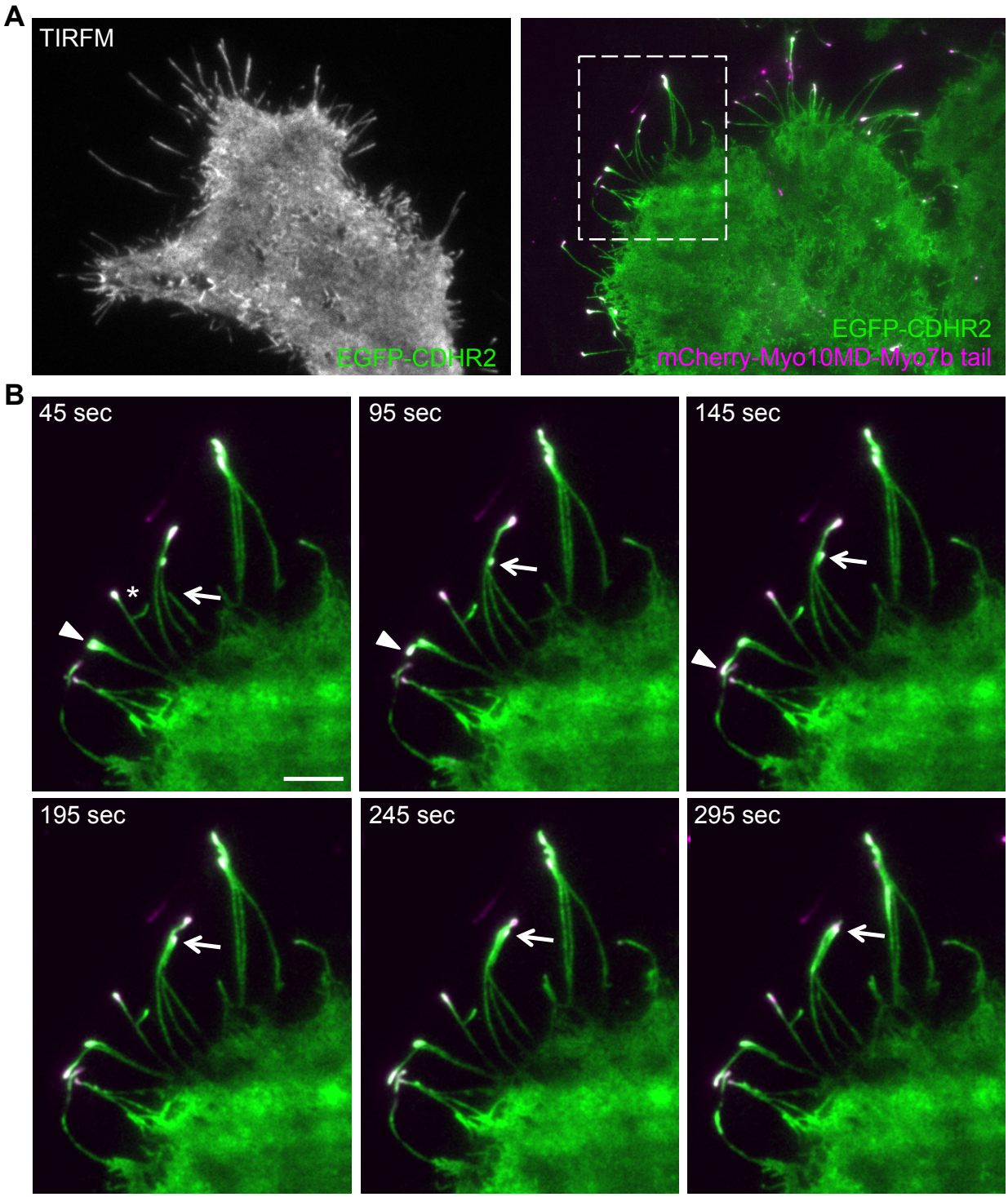

Figure 5-1. Localization of CDHR2 to protrusion tips leads to interfilopodial adhesion. (A) Single time point images from live cell TIRFM of EGFP-tagged CDHR2 (green) expressing cells alone (left) or with mCherry-tagged Myo10MD-Myo7b tail (magenta; right). **(B)** Time series montage of zoomed area in A. Arrows indicate protrusion incorporation into a bundle and subsequent length matching. Arrowheads point to significant curvature of a protrusion (~90°). Asterisk indicates bifurcation of a filopodium. Scale bar, 5 μm.

Enrichment of CDHR2 at protrusion tips results in filopodial bundling

To further examine this phenotype, we used SIM to more closely analyze fixed cells co-expressing CDHR2 and the chimeric motor for filopodial adhesion. With the increased resolution, we were able to see clear examples of adhesion between adjacent protrusions (Figure 5-2 A and B). In some cases, this led to filopodial bundling, with multiple protrusions tightly adhering to one another (Figure 5-2 A; zoom). SIM imaging of cells with low expression of the constructs revealed areas of contact were typically associated with puncta of CDHR2 (Figure 5-2 B; zoom 2, arrowheads). We also were able to see a CDHR2 adhesion link between two filopodia (Figure 5-2 B; zoom 2, arrow).

Bundling and adhesion between adjacent protrusions could lead to membrane fusion in this system. Although SIM increases our resolution to 100 nm (about the diameter of a filopodium), it does not provide information on the ultrastructure or surface topography of these protrusions. To visualize these bundles with higher resolution and confirm that the membrane surrounding individual protrusions incorporated in the bundles was not fusing, we performed SEM on HeLa cells co-expressing CDHR2 and Myo10MD-CC-Myo7b tail constructs. Cells with robust filopodial bundling were easily distinguishable, with some cells having many examples (Figure 5-2 C; left). Interestingly, although the individual bundles had different lengths, the filopodia within

each bundle were roughly the same length (Figure 5-2 C; left). Additionally, larger bundles containing 8-10 filopodia were also seen (Figure 5-2 C; right). Even in the large bundles were the filopodia the same length. Taken together, these data support the function of CDHR2 in regulating protrusion length.

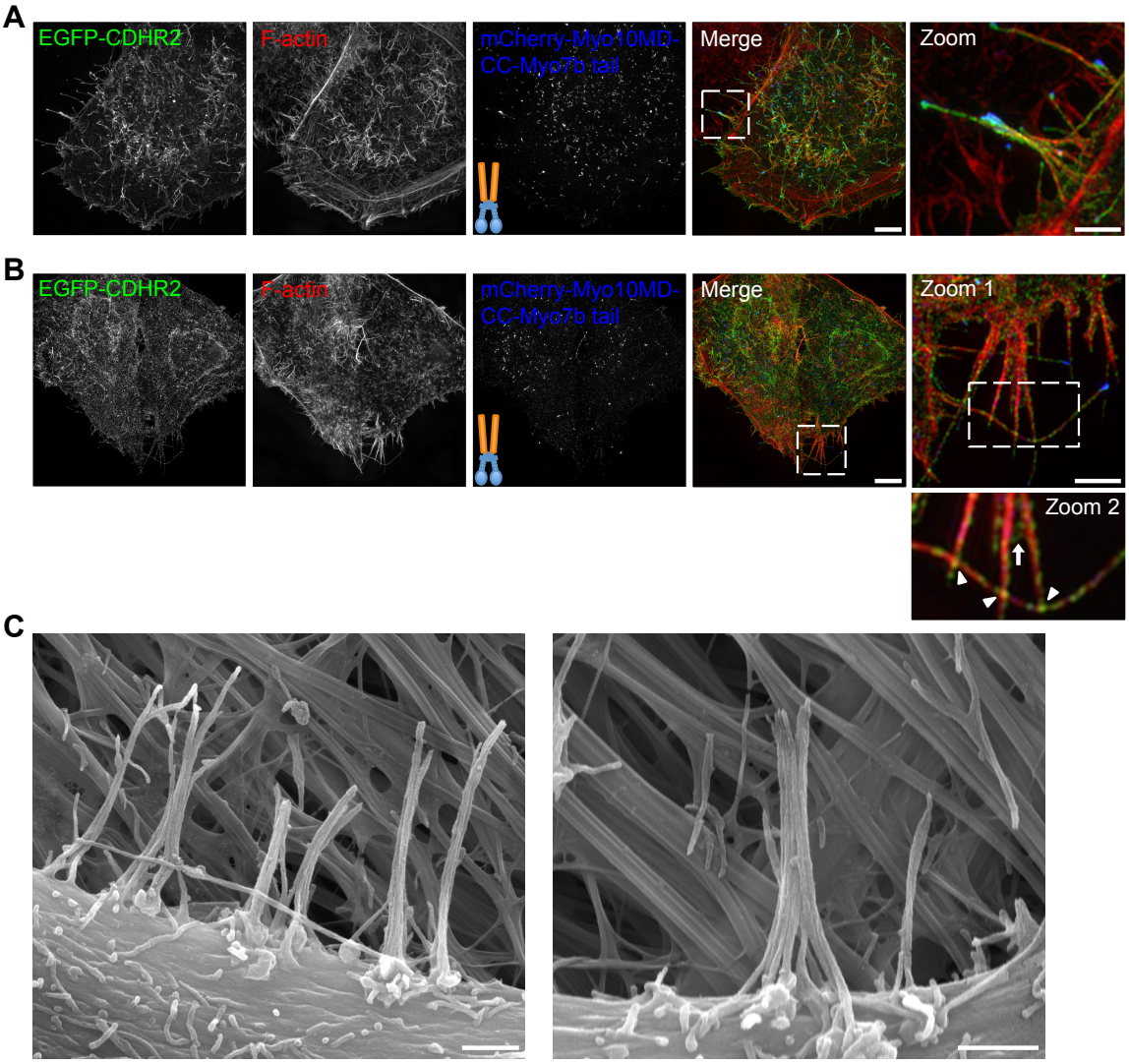

Figure 5-2. Homophilic interactions of CDHR2 drive filopodial adhesion and bundling. (A and B) SIM images of HeLa cells expressing EGFP-tagged CDHR2 (green) and mCherry-tagged Myo10MD-CC-Myo7b tail (pseudo-colored blue), stained for F-actin (pseudo-colored red). Arrowheads show CDHR2 puncta at points of contact between filopodia. Arrow indicates CDHR2 adhesion link. Boxed areas indicate regions in zoomed images. Scale bars, 5 μm; 2 μm in zooms. **(C)** SEM images of HeLa cells expressing CDHR2 and Myo10MD-CC-Myo7b tail. Scale bars, 1 μm.

In rare cases during SIM imaging we saw enlarged structures at the distal tips of filopodia (Figure 5-3 A). We were not sure if this resulted from the tip curling back on itself or a swelling of the tip, leading to a bulbous structure. Interestingly, we were able to find an example of this using SEM. We could clearly see the distal tip of the filopodia curling and adhering to itself, creating a circular structure at the end of these protrusions (Figure 5-3 B). From these data, it appears that the homophilic interaction between CDHR2 molecules can cause severe curvature of filopodia when enriched at the distal tip, resulting is self-association within an individual protrusion.

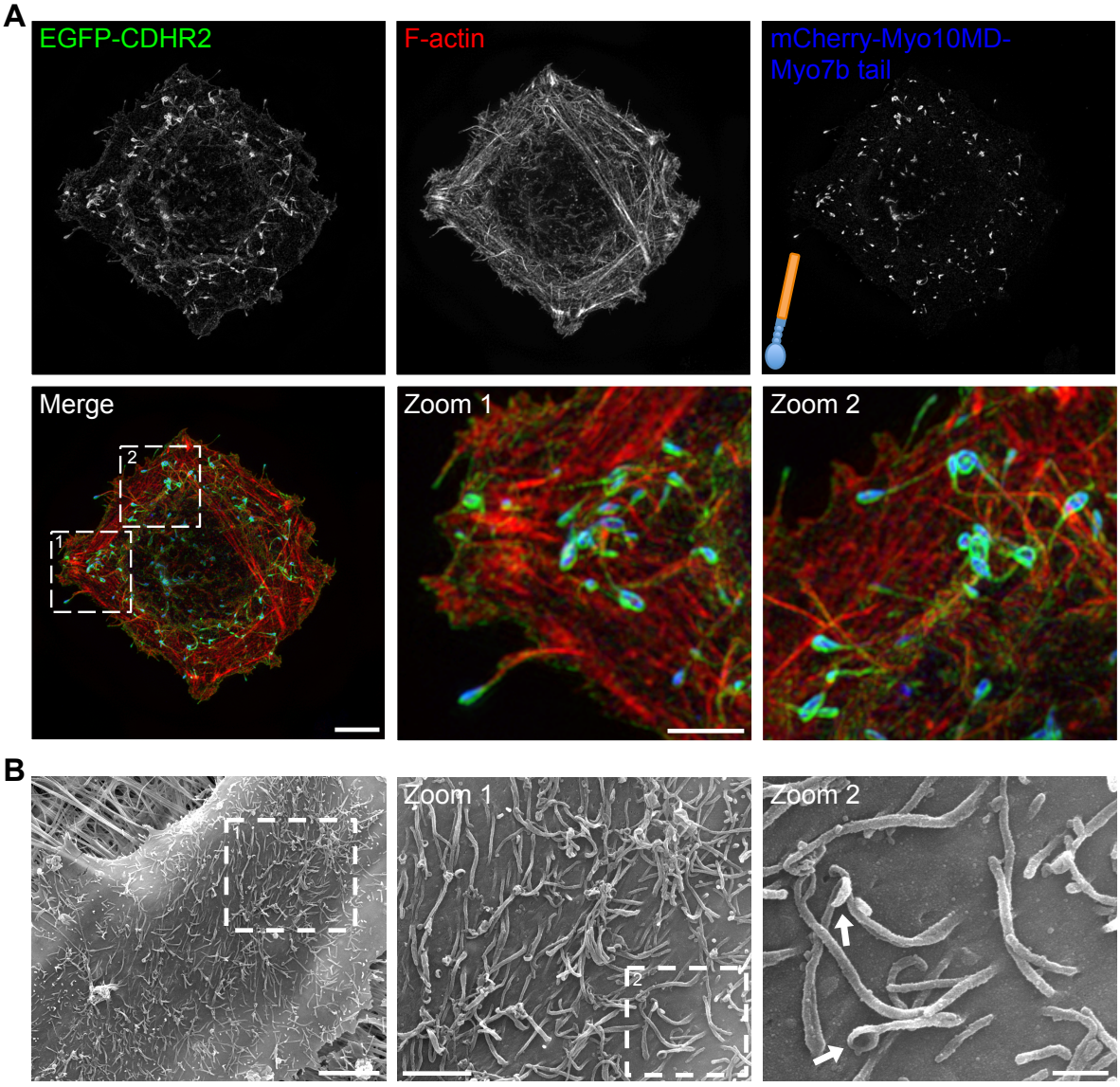

Figure 5-3. Tip-enrichment of CDHR2 can cause curling of protrusion ends. (A) SIM images of a HeLa cell expressing EGFP-tagged CDHR2 (green) and mCherry-tagged Myo10MD-Myo7b tail (pseudo-colored blue), stained for F-actin (pseudo-colored red). Scale bars, 5 μm; 2 μm in zooms. **(B)** SEM images of a HeLa cell expressing CDHR2 and Myo10MD-Myo7b tail. Arrows indicate curled ends of filopodia. Scale bars, 5 μm; 2 μm in zoom 1; 0.5 μm in zoom 2. Boxed areas indicate regions in zoomed images.

Interfilopodial adhesion results in microvilli-like tipi structures on the dorsal surface of HeLa cells

We next wanted to analyze the vertical sections of the SIM images to visualize dorsal filopodia. During brush border assembly, microvilli form tipi-like clusters on the apical surface of CACO-2_{BBE} cells (Crawley et al. 2014). Mediated by the adhesion between CDHR2 and CDHR5, these structures are thought to help organize microvillar protrusions to optimize packing. Vertical projections of SIM images revealed numerous dorsal filopodia (Figure 5-4 A). Sectioning of the X-Z plane showed multiple examples of tipi-like structures formed by adhering filopodia (Figure 5-4 B; arrows). These protrusions are specifically interacting at their distal tips. This tip adhesion is likely supporting these filopodia, enabling them to remain upright. Vertical orientation of protrusions is a key organizing principle. This allows for tight interactions along the full length of the protrusion, minimizing the free space between them and optimizing packing. Additionally, it allows for the growth and incorporation of new protrusions in an organized fashion. Adhesion specifically at the distal tip is critical for maintaining order in the structure.

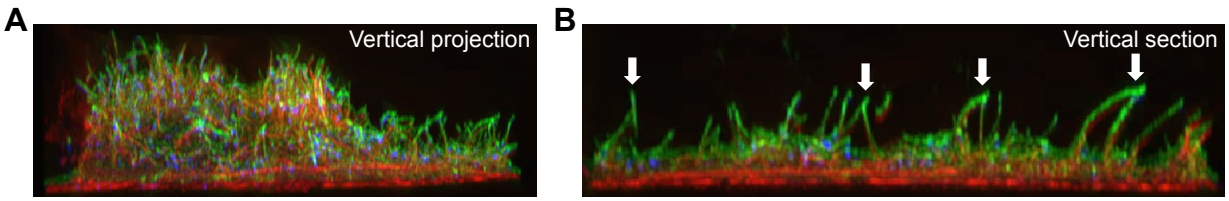

Figure 5-4. Dorsal filopodia form tipi-like structures through tip adhesion. (A) Vertical projection and **(B)** vertical section of a SIM image of a HeLa cell expressing EGFP-tagged CDHR2 (green) and mCherry-tagged Myo10MD-CC-Myo7b tail (pseudo-colored blue), stained for F-actin (pseudo-colored red). Arrows indicate tip adhesion.

Developing an inducible system to visualize adhesion events

In order to better understand the adhesion and length matching, we wanted to develop a system where we could robustly and repeatedly visualize the formation of interfilopodial adhesion. To do this, we would need temporal control over the tip enrichment of CDHR2 so we could induce the localization while imaging. This would enable us to watch in real time as CDHR2 enriches at filopodial tips and the subsequent downstream effects that lead to bundling and length matching. We decided to take advantage of the FKBP-FRB inducible heterodimerization system (Fegan et al., 2010; Putyrski and Schultz, 2012) (Figure 5-5). FKBP and FRB are small protein modules that independently bind very tightly to a rapalog (rapamycin analog). These interactions do not interfere with one another so both proteins can bind to the same rapalog molecule. Upon addition of the drug to cells, FKBP and FRB bind to the rapalog, generating a heterodimer. Fusion of these modules onto two proteins of interest will result in their heterodimerization upon rapalog addition. Therefore, we can add the drug while live cell imaging and visualize the heterodimerization and translocation of Myo10MD and CDHR2.

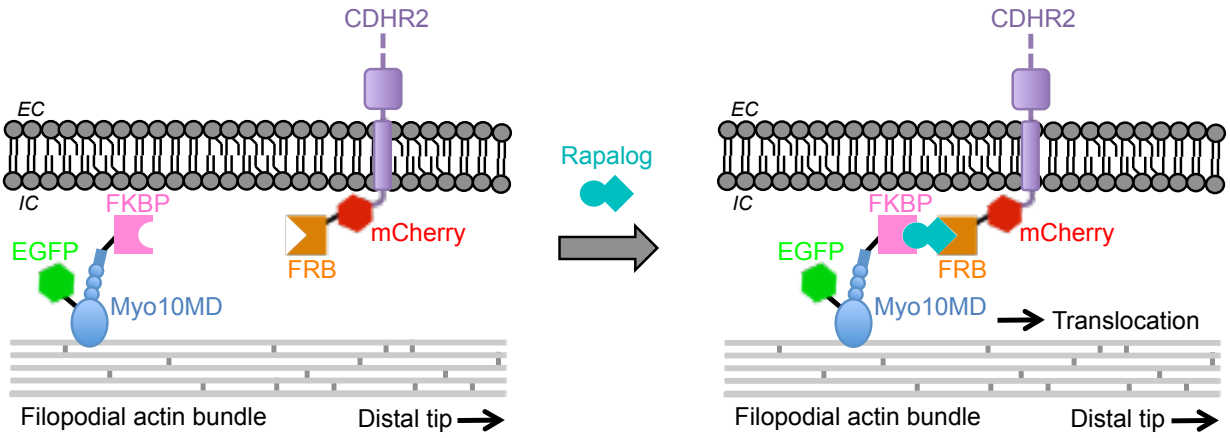

Figure 5-5. FKBP-FRB inducible heterodimerization system. Before treating the cells with rapalog, EGFP-Myo10MD-FKBP is cytosolic and CDHR2-mCherry-FRB localizes throughout the plasma membrane. Addition of the rapalog brings FKBP and FRB together, resulting in the heterodimerization of the fusion proteins. This leads to a processive unit and translocation of the complex along the filopodial actin bundle to the distal tips of the protrusion.

To utilize this system effectively, we decided to use the Myo10MD construct lacking the coiled coil. Therefore, the motor would be soluble and not tip targeted at the beginning of the assay. We fused the FKBP domain onto the C-terminus of the Myo10MD, where the cargo-binding domain is located in the full-length protein. The FRB domain was fused to the C-terminal tail of CDHR2, after the mCherry fluorescent tag. Expression of these two constructs in HeLa cells resulted in the expected localization, with the motor being soluble and CDHR2 throughout the membrane (Figure 5-6; 0 min). However, shortly after the rapalog addition (Figure 5-6; 2 min), we begin to see colocalized puncta at the distal tips of filopodia (Figure 5-6; 12 min). By 18 min, we see robust tip localization of both constructs, leading to an induction of protrusion formation and elongation. Future experiments will focus on adjusting the imaging parameters to enable longer acquisitions so we can visualize and characterize adhesion events.

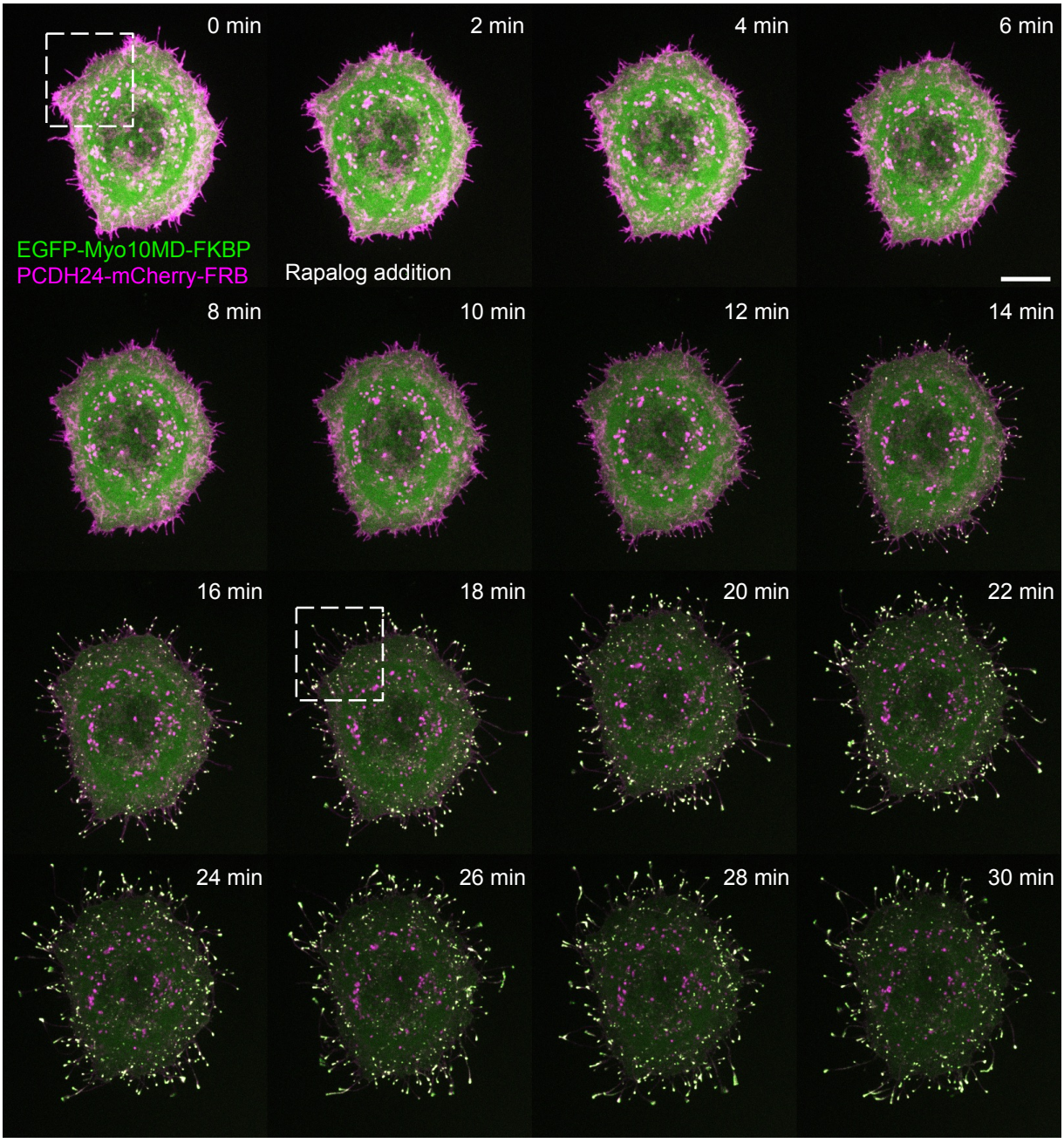
0 min
2 min
4 min
6 min
EGFP-Myo10MD-FKBP
PCDH24-mCherry-FRB
Rapalog addition
8 min
10 min
12 min
14 min
16 min
18 min
20 min
22 min
24 min
26 min
28 min
30 min

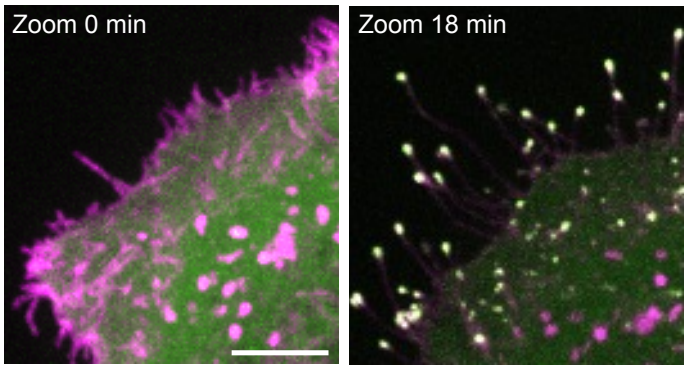
Zoom 0 min
Zoom 18 min

Figure 5-6. Induced translocation of adhesion to the distal tips of protrusions leads to robust filopodial induction and elongation. Spinning disk confocal time series montage of a HeLa cell co-expressing EGFP-Myo10MD-FKBP (green) and CDHR2-mCherry-FRB (magenta). Boxed areas indicate regions in zoomed images. Scale bar, 10 μm; 5 μm in zoom.

DISCUSSION AND FUTURE DIRECTIONS

Tip enriched adhesion impacts the morphology and dynamics of actin-based protrusions

We have shown that the distal tip enrichment of CDHR2 by the Myo10-Myo7b chimeric motor results in the bending and curving of filopodial protrusions. Through this action, filopodia come in contact with one another, leading to CDHR2-mediated adhesion. Continued growth of these protrusions causes increased adhesion along the length, resulting in bundling. Once bundled, filopodia become stabilized and long-lived. This normalizes the length of the protrusions to make them roughly the same. Additionally, it enables dorsal protrusions to orient in the vertical axis, generating tipi-like structures reminiscent of microvillar clusters. We then established an inducible approach to visualize the initiation of filopodial adhesion. This system revealed a significant effect of forcing the interaction between Myo10 and CDHR2, resulting in robust protrusion formation and elongation. Using the in-cell reconstitution assay and inducible heterodimerization, we can begin to study how the length of actin-based protrusions can be regulated by an adhesion-based mechanism.

Dissecting the roles of adhesion and the motor in filopodial induction and elongation

It is clear from Figure 5-6 that dimerizing CDHR2 to a Myo10 motor and translocating the complex to filopodial tips results in the significant induction and elongation of protrusions. However, this phenotype could be independent of adhesion, and solely a result of linking the plasma membrane to a Myo10 motor and the underlying actin cytoskeleton. Recruitment of the Myo10 motor to the membrane could be responsible for this induction and elongation. Full-length Myo10 does lead to an increase in the number and length of filopodia (Berg and Cheney, 2002; Bohil et al., 2006). Additionally, it has been suggested that Myo10 can initiate protrusion formation by bringing together actin filaments to form a bundle (Tokuo et al., 2007). Therefore, additional controls are needed to determine the mechanism of the induction and elongation. To determine the role of the adhesion, we will generate FRB fusion proteins of CDHR2 lacking the EC1 domain and entire ectodomain. The EC1 deletion will disrupt the homophilic interaction between CDHR2 molecules, and delineate the role of *trans* adhesion in generating this phenotype. The ectodomain deletion will abolish any *cis* interactions and only serve as a membrane tether for the motor. This will help determine if recruitment of Myo10 to the membrane is sufficient to drive the induction and elongation phenotype.

To control for the contribution of Myo10, we will generate FKBP fusion proteins of the Myo7bMD and Myo7bMD-GCN4 constructs (Figure 3-2 B). Although Myo7b still binds to actin, it will have less of an effect on the cytoskeleton as the Myo7b MD forced dimer does not robustly target to filopodial tips or induce protrusion formation (Figure 3-8 E). These constructs will also help determine the minimal unit of Myo7b motors

required to translocate to the tips of protrusions when bound the membrane. This could reveal interesting characteristics of the Myo7b motor. First, it will reveal if a monomer or dimer of Myo7b MDs is sufficient to tip target when bound to the membrane. A caveat to this assay is that the Myo7b motor likely prefers microvillar actin bundles. This may be the reason why the forced dimer of Myo7b MDs is unable to robustly target to filopodial tips. Another reason for this may be that the actin retrograde flow is too fast in filopodia for the Myo7b motor to efficiently target. Both of these may result in a lack of targeting of Myo7b even when bound to the membrane. To get around this, we can use the FKBP fusion protein of the ectodomain deletion of CDHR2 to tether the Myo7b-FRB motor constructs to the membrane in LLC-PK1-CL4 cells. As demonstrated in Chapter III, we know that the forced dimer of Myo7b can target to the distal tips of microvilli. We can use this to determine if a monomeric Myo7b motor bound to the membrane is also capable of localization to microvillar tips. These are relevant questions as endogenous Myo7b in the IMAC complex is bound directly or indirectly to CDHR2, a transmembrane protein, and is therefore linked to the membrane.

Mechanisms of filopodial bending and bifurcation

The significant curvature of filopodial ends that accompanies tip enrichment of CDHR2 is a striking phenotype that is rarely seen in control cells. This brings up interesting questions about CDHR2 adhesion and how it might be mediating bending of these protrusions. One possibility is the homophilic adhesion between CDHR2 molecules. Tip enrichment of CDHR2 leads to an increased local concentration of proteins. Adhesion between molecules at the end of an individual protrusion may lead to the curling.

Alternatively, the *cis* interactions may be mediating this phenotype. Although there is no direct evidence to suggest CDHR2 multimerizes, the cadherins that form stereocilia tip-links have been suggested to dimerize (Kachar et al., 2000; Tsuprun et al., 2004). Again, because of the increased concentration of proteins, these *cis* interactions may cause local deformations in the membrane, leading to bending of the filopodia as the actin bundle generates force against the membrane. Through a similar mechanism, curving of protrusions could be a result of the extreme tip localization of a transmembrane protein. However, this phenotype has not been reported in studies of Myo10 and its transmembrane cargo proteins (Almagro et al., 2010; Lai et al., 2015; Liu et al., 2012; Pi et al., 2007; Zhang et al., 2004; Zhu et al., 2007). These possibilities can be addressed using the different deletion constructs of CDHR2, discussed above. The EC1 deletion in this assay will control for the adhesion-based mechanism, while the ectodomain deletion will control for *cis* interactions. Using these constructs, we can begin to understand the mechanism/s behind filopodial bending.

Bifurcations of filopodia are also rarely seen under normal conditions. We need to verify that this is genuine bifurcation, and not a tubular outgrowth of membrane. To do this, we need to label actin filaments to confirm the presence of a bundle in both branches. We can use fixed and live cell imaging to search for examples of bifurcation to determine this. Additionally, it would be extremely informative to visualize the formation of a bifurcated filopodia using live cell imaging. This will provide us with information on how and why these structures are developing. They are likely a result of the curvature of filopodia. Bundled actin filaments are fairly stiff and do not bend easily (Bathe et al., 2008; Claessens et al., 2006; Mogilner and Rubinstein, 2005). Therefore,

when significant curvature of the membrane is induced by CDHR2, the actin bundle likely extends straight, along the original path of filopodial growth. This leaves behind a membrane bud that can then be filled actin and maintained as an outgrowth.

Adhesion-based stabilization of the IMAC

In the last chapter, we introduced the use of the in-cell reconstitution assay to address questions about IMAC protein turnover. Using this FRAP-based approach, these experiments could also be used to answer questions about the role of adhesion in complex stability. For instance, does adhesion between two adjacent filopodia stabilize Myo7b and/or CDHR2 molecules? This could be analyzed by comparing the turnover of CDHR2 and Myo7b populations at the tips of individual protrusions versus protrusions that are adhered to one another. We hypothesize that adhesion between CDHR2 molecules would stabilize these proteins and, potentially, proteins interacting with them. Additionally, we could compare the turnover of full-length CDHR2, the EC1 deletion, and a deletion of the entire ectodomain. The EC1 deletion will eliminate any *trans* interactions between CDHR2 molecules, and we can test the role of this adhesion in protein turnover. A deletion of the entire ectodomain would abolish any *cis* interactions. Stereocilia cadherins have been shown to dimerize in cis (Kachar et al., 2000; Tsuprun et al., 2004). It is likely that the microvillar protocadherins also form dimers or trimers. The role of these *cis* interactions in mediating complex formation and adhesion are unknown.

Length regulation by adhesion

Although the homophilic adhesion of CDHR2 resulted in an interesting phenotype, the relevance of this interaction *in vivo* is questionable. KD of CDHR5 in CACO-2_{BBE} cells led to significant defects in brush border assembly, indicating that CDHR2 may not be sufficient (Crawley et al., 2014b). However, this needs to be confirmed *in vivo* with a CDHR5 KO mouse model. Additionally, because the CDHR2 and CDHR5 heterophilic interaction is much stronger than the CDHR2 homophilic interaction, the main population of linkages in the brush border likely consists of heterophilic interactions. Therefore, we would like to incorporate CDHR5 into the in-cell reconstitution assay and inducible system with CDHR2. This will help us begin to characterize the roles of each type of adhesion. With the increased strength of the heterophilic interaction, we would hypothesize that the adhesion between filopodia would be more robust. However, the effect on length regulation is more convoluted. If there are signaling mechanisms downstream of CDHR2 that are specifically regulated by homophilic adhesion, introduction of CDHR5 into the system could disrupt the length control. Alternatively, if adhesion is acting a physical constraint on the growth of neighboring protrusions, stronger adhesion may lead to tighter control of the length.

One method of length control is a direct mechanism that involves downstream signaling pathways. These effector proteins would regulate actin dynamics to ultimately control protrusion length, and may include but are not limited to actin nucleators, elongators, cappers, and bundlers. For this model to apply to our system, the effector molecule/s would have to be present in both microvillar and filopodial protrusions. Both finger-like actin-based protrusions have a dense plaque at the plus-end of the actin

bundle, known as the tip complex (Mooseker and Tilney, 1975; Svitkina et al., 2003). One shared protein, Eps8, has been localized to the distal tips of all three finger-like protrusions: stereocilia, microvilli, and filopodia (Behlouli et al., 2014; Croce et al., 2004; Disanza et al., 2004; Manor et al., 2011; Tocchetti et al., 2010; Zampini et al., 2011). Shared proteins between microvilli and filopodia may be mediating the downstream effects of CDHR2 adhesion on length regulation. Identifying possible downstream effectors of CDHR2 will be key to determining the mechanism of length regulation.

Another possible model of length control is through an indirect, physical mechanism. By tightly adhering protrusions together, they cannot physically outgrow their neighbors. Tension on the system through adhesion applies a force on the protrusions. This force prevents the elongation of one protrusion past its neighbor, likely by acting on the underlying actin bundle to prevent its growth. This also makes an argument for why CDHR2 alone cannot mediate length matching. First, because the adhesion is not focused at the tips, there is not enough localized force generated to alter actin dynamics. Additionally, the motor may play a key role in transmitting the tension from the links and membrane to the underlying actin cytoskeleton.

To test actin dynamics experimentally, we could again utilize FRAP to trace the movement of EGFP-tagged β-actin through the filopodial protrusion. Alternatively, we could use a photo-convertible fluorescent protein, such as mEos2, fused to β-actin. Photo-conversion of a small segment of the filopodial bundle would enable us to visualize treadmilling. Kymograph analysis would provide us direct measurements of retrograde flow. If actin dynamics are altered by adhesion between filopodia, we would hypothesize that treadmilling is slower in bundled filopodia. By comparing the rates of

actin flow between individual and bundled protrusions, we can begin to understand the role of adhesion in length control. Another experiment to test the role of adhesion on length control, would be to treat cells with calcium chelating agents like BAPTA or EGTA. These have been used extensively in the stereocilia literature to study tip-links. Additionally, our laboratory has shown the interaction between CDHR2 and CDHR5 is calcium-dependent (Crawley et al., 2014b). This approach could be used in the in-cell reconstitution assay and CACO-2_{BBE} monolayers, as well as *in vivo* using mouse intestinal tissue. If it is controlling protrusion length, disruption of adhesion should result in the loss of length uniformity. However, these experiments will not determine whether actin dynamics are regulated directly or indirectly by adhesion. Future experiments should focus on distinguishing between these two models of length regulation.

CHAPTER VI

FUTURE DIRECTIONS AND CONCLUSION

In addition to the future directions discussed in Chapter V, many questions still remain about the formation and function of Myo7b and the IMAC in the brush border. Many of these include identifying new components of the brush border and interactions with other proteins. However, basic questions about Myo7b motility still need to be addressed. We will discuss future experiments using a range of *in vitro* and *in vivo* methods that can begin to answer these questions.

In vitro analysis of Myo7b and reconstitution of transport

Purified proteins and *in vitro* experiments have been used for kinetic analyses of Myo7b (Henn and De La Cruz, 2005; Yang et al., 2005). However, these studies used motor domain only constructs and no assays examining motile properties were performed. Therefore, the motility of Myo7b should be investigated using recombinant protein and *in vitro* motility assays. Using Sf9 insect cells, Myo7b constructs can be expressed and purified. Initial experiments should include motor domain, forced dimer, and full-length constructs, using a HaloTag for fluorescent labeling. Sliding filament assays and single-molecule motility assays should be performed, providing information on the duty ratio, landing rate, and run length. Additionally, similarly to Myo7a, negative stain EM can be used to visualize the conformation of full-length Myo7b (Sakai et al., 2015; Yang et al.,

2009). Based on the structure and similarities to Myo7a, we would hypothesize that Myo7b is also monomeric in solution and adopts a folded, auto-inhibited state.

In vitro experiments can also be used to study complex formation, requirements for processive movement, and effects of different cargo proteins on myosin motility (Heym et al., 2013; Sckolnick et al., 2013; Sladewski et al., 2013; Wu et al., 2006). Assuming that full-length Myo7b alone is not processive *in vitro*, we could incorporate cargo molecules to try to reconstitute Myo7b-dependent transport. Addition of the scaffolding proteins into this assay could provide experimental evidence for the role of these proteins in Myo7b multimerization and processivity. To add even more complexity to the system, lipid vesicles as cargo have been introduced into these assays (McIntosh et al., 2015; Nelson et al., 2014). The cytoplasmic domains of CDHR2 and CDHR5 can be conjugated to synthetic lipid vesicles to enable their use as cargoes. Additionally, to recapitulate *cis* dimers of these proteins, the cytoplasmic domains can be dimerized using a GCN4 leucine zipper or GST-tag.

Multimerization of Myo7b and additional binding partners

Although we have tried to address how Myo7b is multimerized into a transport unit, we have been unsuccessful. Future studies should first focus on determining if the Myo7b tail is mediating self-association and targeting of the ‘monomeric’ chimera. To do so, co-transfections of the chimeras with Myo7b tail fragments should be analyzed for co-localization at filopodial tips, potentially indicating an interaction. This may also lead to a dominant negative effect, as association of motors with fragments that cannot bind to actin may prevent tip targeting. Additionally, biochemical pull-downs with different tail

fragments could be used to test this hypothesis. Alternatively, to identify novel cargo molecules that may be mediating targeting of the 'monomeric' chimera or multimerization, a proteomic approach may be used. We could use the BioID2 system to biotinylate proteins in close proximity to the Myo7b tail in HeLa cells, purify them using streptavidin beads, and submit them for mass spectrometry analysis. This could also be done in fully differentiated CACO-2_{BBE} cells to confirm any potential hits or to see if these cargo proteins are also expressed in intestinal epithelial cells.

In addition to identifying proteins that may act as dimerizers, the possibility of additional Myo7b cargo molecules remains an open question. This is a particularly interesting question as it may play critical roles in several aspects of these studies. First, from Chapter III, expressing the tail domain alone when endogenous Myo7b is present results in robust tip targeting (Figure 3-8 C). Therefore, the tail domain contains some targeting information through interactions with cargo molecules. These cargoes include but are not limited to the IMAC. Additionally, a mutation in full-length Myo7b that is predicted to prevent lever arm rotation and force generation is still able to partially rescue the localization of the IMAC in CACO-2_{BBE} Myo7b KD cells (Figure 3-9). This suggests that the motor activity is involved but not required for the localization of Myo7b, and an alternate targeting mechanism may exist. Cooperative interactions between actin binding by the motor domain and cargo binding by the tail domain may be mediating this force-independent targeting. In addition, Myo7b may also be able to interact with another tip-enriched protein that aids in rescuing the localization. Potential binding partners include proteins that are proposed to participate in the formation of the electron-dense foci present at the plus-ends of parallel actin-based protrusions, known

as the tip complex (Mooseker and Tilney, 1975; Rzadzinska et al., 2004; Svitkina et al., 2003). This complex is likely comprised of proteins that spatially and temporally control actin polymerization, as this is the site of actin monomer addition (Mooseker et al., 1982; Pollard and Mooseker, 1981).

This mechanism of targeting may also be why the 'monomeric' chimera from Chapter IV can target to the distal tips of filopodia. Microvillar and filopodial protrusions may share components of the tip complexes or other tip-enriched proteins. If this is the case, localization of the 'monomeric' motor could occur through two mechanisms. First, if the binding partner only interacts with the plus-end of actin filaments and not along the length, the 'monomeric' chimera may target through a passive mechanism, not involving motor activity. Alternatively, if the binding partner can interact with actin along the entire filament, the 'monomeric' motor may use it as a crutch to move processively along the bundle, as considered in the Discussion of Chapter IV.

Furthermore, the idea of other binding proteins at protrusion tips also connects back to possible downstream effectors of adhesion for length regulation. If indeed, there are shared components of the tip complex between microvilli and filopodia, these could be mediating the adhesion-dependent length control mechanism seen in both protrusions. Given the localization of the fast growing plus-ends of actin at the distal tip, as mentioned above, these proteins could be key regulators of actin dynamics. Proteins we know localize to the tips of filopodia include actin nucleators (Applewhite et al., 2007; Hansen and Mullins, 2010; Lebrand et al., 2004; Pellegrin and Mellor, 2005; Schirenbeck et al., 2005a; Schirenbeck et al., 2005b; Tokuo and Ikebe, 2004), membrane bending proteins (Disanza et al., 2013; Nakagawa et al., 2003), and

signaling proteins (Almagro et al., 2010; Hirano et al., 2011; Lai et al., 2015; Liu et al., 2012; Pi et al., 2007; Wei et al., 2011; Zhang et al., 2004; Zhu et al., 2007). However, the microvillar tip complex remains largely uncharacterized.

Identification of potential tip complex proteins has already begun in our laboratory. One known protein that localizes to the distal tips of all three finger-like protrusions is epidermal growth factor receptor kinase substrate 8, Eps8 (Behlouli et al., 2014; Croce et al., 2004; Disanza et al., 2006; Manor et al., 2011; Tocchetti et al., 2010; Zampini et al., 2011). It controls the length of these protrusions through its actin bundling and capping activities (Disanza et al., 2004; Hertzog et al., 2010). Its localization in microvilli is extremely specific to the distal tips where it promotes microvillar elongation (Postema et al., 2018). A current graduate student, Isabella Gaeta, is working on using Eps8 to identify other proteins at the plus-ends of microvillar actin bundles.

Function of Myo7b *in vivo*

We recently obtained a constitutive Myo7b KO mouse model and have begun to characterize the effect of Myo7b loss on brush border formation *in vivo*. Preliminary data suggests that loss of Myo7b results in decreased expression of the IMAC components CDHR5 and USH1C (Figure 6-1). This occurs in both brush border forming organs, the intestine (Figure 6-1 A) and kidney (Figure 6-1 B). Additionally, the distal tip enrichment of these proteins is lost. Contrast enhanced images of the Myo7b KO tissue shows diffuse localization of Myo7b cargo molecules (Figure 6-1; zoom insets). Line scan analyses confirm both of these observations (Figure 6-1). Also, brush borders of Myo7b

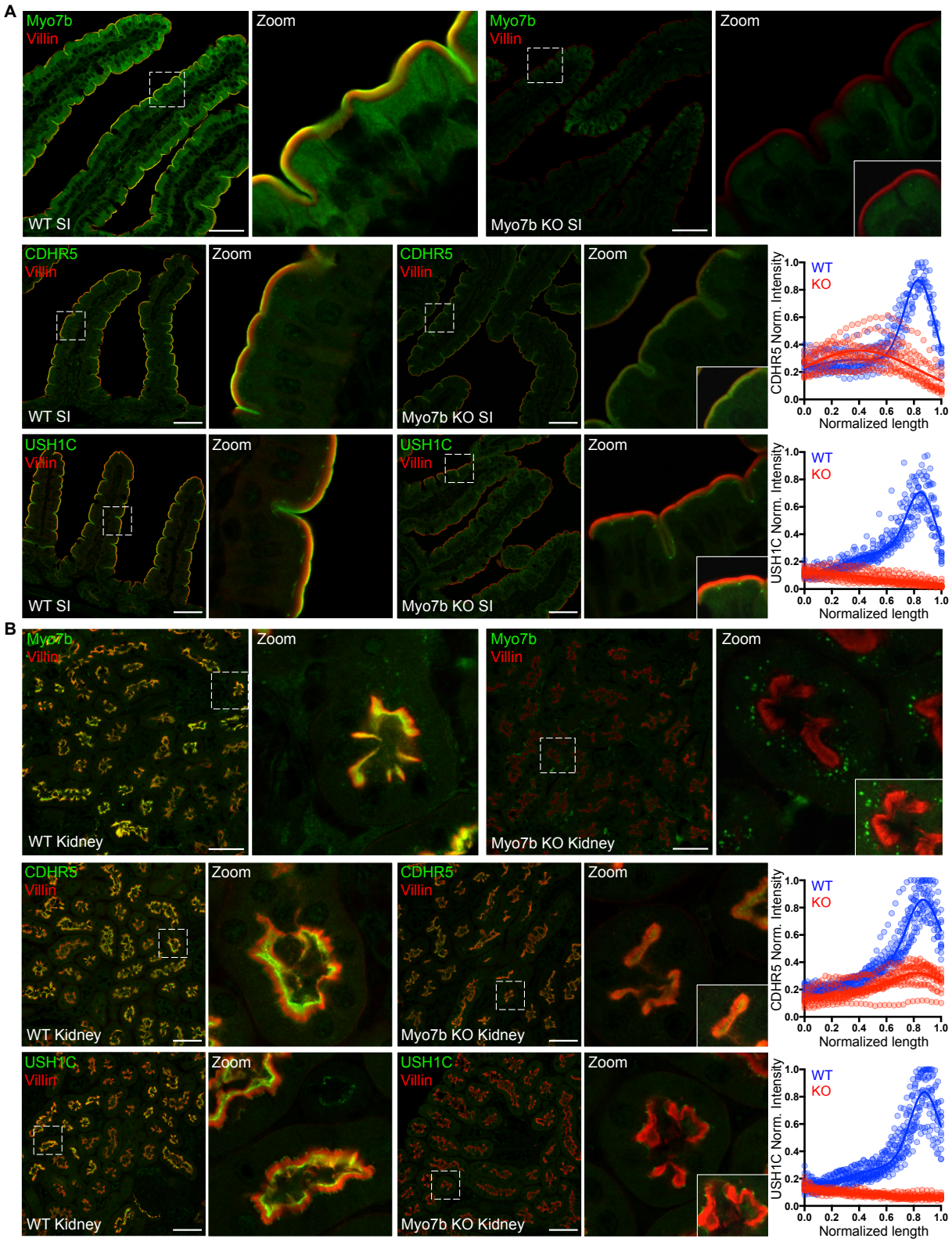
A
Myo7b
Villin
Zoom
WT SI
Myo7b KO SI
CDHR5
USH1C
CDHR5 Norm. Intensity
USH1C Norm. Intensity
WT
KO
Normalized length
B
WT Kidney
Myo7b KO Kidney

Figure 6-1. KO of Myo7b results in decreased expression and loss of distal tip enrichment of CDHR5 and USH1C. Confocal images of **(A)** small intestine or **(B)** kidney tissue stained for Myo7b, CDHR5 or USH1C (green) and villin (red) to label the brush border. Boxed areas indicate regions in zoomed images. Insets in zoom show contrast enhanced images. Scale bars, 50 μm. Line scans of IMAC component intensities parallel to the microvillar axis in WT (blue) and Myo7b KO (red) tissue; 0 = base and 1 = tip. n = 10 line scans with Gaussian curve fits.

KO mice appear shorter than WT controls, although more thorough quantitation is required.

To look for defects in brush border morphology, we used SEM to visualize the surface of tissue from the colon. Loss of Myo7b results in severe perturbations to brush border formation and organization (Figure 6-2). Similarly to the USH1C KO mouse (Crawley et al., 2014b), some colonocytes lacked brush borders entirely, which occurred in a mosaic fashion (Figure 6-2). Cells surrounding these bare regions displayed shorter and splayed protrusions (Figure 6-2). Linkages can still be seen between adjacent microvilli, consistent with the immunofluorescence and USH1C KO mouse (Crawley et al., 2014b). Additional experiments are required to quantify changes in mircovillar length and density, proposed below.

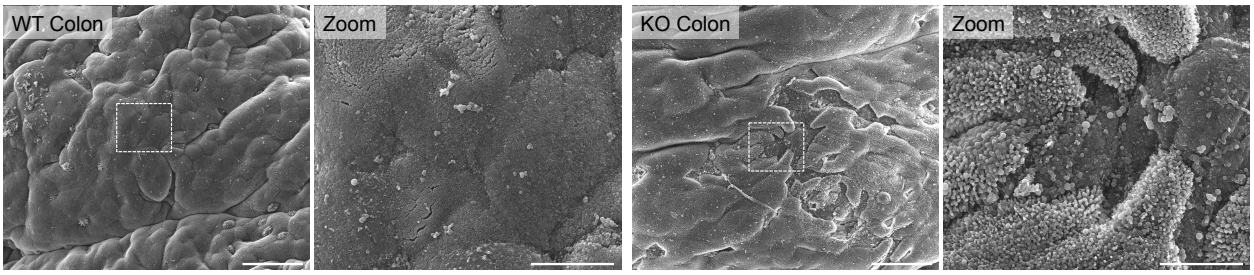

Figure 6-2. Loss of Myo7b disrupts brush border formation *in vivo*. SEM images of WT (left images) and Myo7b KO (right images) colonic tissue. Boxed areas indicate regions in zoomed images. Scale bars, 20 μm; 5 μm in zooms.

Future experiments are needed to further understand the role of Myo7b in brush border formation *in vivo*. These experiments include localizing other apical domain and brush border markers to characterize defects in establishing polarity, such as alkaline phosphatase, sucrose isomaltase, ezrin, and E-cadherin. Tissues should also be examined for proliferation and differentiation defects, as USH1C KO mice have decreased Ki-67+ cells in the colon (Crawley et al., 2014b). Additional experiments should include transmission electron microscopy (TEM) to visualize ultrastructural details of the brush border, including microvillar and actin structure. Precise measurements of microvillar length and spacing between protrusions can be made. Immunogold labeling can be used localize CDHR2 and CDHR5 linkages along the microvillar axis (Crawley et al., 2014b). Relationships between the core actin bundle and surrounding plasma membrane can be analyzed, i.e. loss of crosslinking, membrane lifting, microvillar fusion, etc. Additionally, details of the terminal web and changes in its organization can be seen via TEM. Orthogonal cross sections through the brush border can be used to measure microvillar density, as well as the number and organization of actin filaments in the bundle.

Finally, as previously used by our laboratory (Benesh et al., 2010; McConnell et al., 2011), isolation of the brush border from mouse intestinal tissue and shotgun mass spectrometry can be used to identify proteins that reside in this domain. The quantitative nature of this method enables direct comparison between WT and KO mice for differences in peptide counts, which are directly related to the abundance of a protein. This will enable a more precise measurement of the loss of expression and/or localization of the IMAC components. It will provide a more comprehensive list of

proteins affected by the loss of Myo7b. Additionally, compensatory mechanisms can be examined by looking at any proteins that are upregulated in the KO mice. It may also be used to help identify other potential cargo molecules of Myo7b.

Distinguishing the roles of homo- and heterophilic adhesion

A remaining question surrounding the microvillar protocadherins is the differential roles of homophilic and heterophilic adhesion in brush border assembly and function. However, we would need to be able to distinguish between these two interactions to address this question. These interactions likely overlap so specific structural details of both interactions will be required. Through a collaboration with the Sotomayer laboratory, we are working on solving the crystal structures of these interactions. They have previously reported the structure of the heterophilic interaction between PCDH15 and CDHR23, which form an 'extended handshake' involving the first and second EC domains (Sotomayor et al., 2012). Once this information is obtained, we can begin to differentiate between these types of adhesion. One approach would include doing KD rescue experiments with CDHR2 in CACO-2_{BBE} cells to see if we could rescue length uniformity, microvillar clustering, or brush border formation by overexpressing a mutant that is still capable of homophilic but not heterophilic intereactions. Additionally, characterization of a CDHR5 KO mouse may address this question. If homophilic interactions of CDHR2 form *in vivo* and function in brush border assembly, we would hypothesize that linkages would still be formed and maintained in the absence of CDHR5. This KO mouse model can be characterized using all of the assays described above for the Myo7b KO mouse.

Mechanotransduction in the intestine

An additional and relatively unexplored mechanism for signaling in the intestine is mechanotransduction. Fluid flow of luminal contents puts shear stress on enterocytes present on the villus surface (Ishikawa et al., 2011; Lentle and Janssen, 2008). Indeed, a recent study using CACO-2_{BBE} cells demonstrated that intestinal microvilli are capable of sensing shear force, triggering an increase in autophagy (Kim et al., 2017). This study also showed a diminished response when CDHR2 was knocked down, suggesting it may play a direct role in mechanosensation. However, this could be indirect as KD of CDHR2 results in decreased microvillar density (Crawley et al., 2014b), which is also involved in this response (Kim et al., 2017). Using an alternative cell culture model, placental trophoblasts, another study showed that fluid shear stress triggers microvilli formation (Miura et al., 2015). This is mediated by the transient receptor potential, vanilloid family type-6 (TRPV6) calcium ion channel. Flow-induced calcium influx results in the phosphorylation of Akt, leading to phosphorylation and activation of ezrin, a membrane-actin crosslinker (Miura et al., 2015). Taken together, these data suggest a role for microvillar protrusions in mechanotransduction. They also bring up the possibility of CDHR2 being a mechanosensor and the use of mechanosensation to regulate actin-based protrusions.

Given these data, it is tempting to postulate a direct mechanism of microvillar length control through mechanotransduction. Interestingly, this model of coupling mechanotranduction to F-actin polymerization and protrusion stability has been proposed in stereocilia (Caberlotto et al., 2011a; Caberlotto et al., 2011b; Velez-Ortega et al., 2017). Similarities between the IMAC and stereocilia tip-link composition and

structure support this idea. The tip-link complex of consists of similar adhesion, scaffolding, and motor proteins, with USH1C being shared between them. However, unlike microvilli, stereocilia have a staircase pattern, with each row of protrusions being a different height. In this system, deflections of the hair bundle are sensed by tension on the tip-links, leading to mechanotransduction, depolarization of the cell, and downstream signaling. This is mediated by a direct interaction between TMC1 and 2 with the cytoplasmic domain of PCDH15, which is thought to control gating through force transduction (Beurg et al., 2015; Maeda et al., 2014). It is not known if microvilli contain a mechanotransduction channel. However, if it does, the IMAC may play a similar role in this system. Future experiments should focus on identifying and localizing potential mechanotransduction channels in the brush border.

Conclusions

The work presented here shows that Myo7b plays an essential role in microvillar clustering and brush border formation through its function in localizing the IMAC to the distal tips of microvilli (Chapter III). Additionally, we have established an in-cell reconstitution assay that can be used to address questions about protein interactions within the IMAC and their roles in complex formation, function, and turnover (Chapter IV). Finally, we have begun to characterize the morphological effects of tip-enriched adhesion on actin-based protrusions (Chapter V). Initial experiments suggest adhesion at the distal tips regulates the stability and length of these protrusions. Future experiments discussed in this section will be critical in further understanding the role of Myo7b in the brush border and the mechanism regulating length uniformity of microvilli.

REFERENCES

Adamek, N., Coluccio, L.M., and Geeves, M.A. (2008). Calcium sensitivity of the cross-bridge cycle of Myo1c, the adaptation motor in the inner ear. Proceedings of the National Academy of Sciences of the United States of America *105*, 5710-5715.

Adato, A., Michel, V., Kikkawa, Y., Reiners, J., Alagramam, K.N., Weil, D., Yonekawa, H., Wolfrum, U., El-Amraoui, A., and Petit, C. (2005). Interactions in the network of Usher syndrome type 1 proteins. Human molecular genetics *14*, 347-356.

Almagro, S., Durmort, C., Chervin-Petinot, A., Heyraud, S., Dubois, M., Lambert, O., Maillefaud, C., Hewat, E., Schaal, J.P., Huber, P.*, et al.* (2010). The motor protein myosin-X transports VE-cadherin along filopodia to allow the formation of early endothelial cell-cell contacts. Molecular and cellular biology *30*, 1703-1717.

Altman, D., Sweeney, H.L., and Spudich, J.A. (2004). The mechanism of myosin VI translocation and its load-induced anchoring. Cell *116*, 737-749.

Ameen, N., and Apodaca, G. (2007). Defective CFTR apical endocytosis and enterocyte brush border in myosin VI-deficient mice. Traffic *8*, 998-1006.

Anderson, D.W., Probst, F.J., Belyantseva, I.A., Fridell, R.A., Beyer, L., Martin, D.M., Wu, D., Kachar, B., Friedman, T.B., Raphael, Y.*, et al.* (2000). The motor and tail regions of myosin XV are critical for normal structure and function of auditory and vestibular hair cells. Human molecular genetics *9*, 1729-1738.

Antonellis, P.J., Pollock, L.M., Chou, S.W., Hassan, A., Geng, R., Chen, X., Fuchs, E., Alagramam, K.N., Auer, M., and McDermott, B.M., Jr. (2014). ACF7 is a hair-bundle antecedent, positioned to integrate cuticular plate actin and somatic tubulin. The Journal of neuroscience : the official journal of the Society for Neuroscience *34*, 305-312.

Applewhite, D.A., Barzik, M., Kojima, S., Svitkina, T.M., Gertler, F.B., and Borisy, G.G. (2007). Ena/VASP proteins have an anti-capping independent function in filopodia formation. Molecular biology of the cell *18*, 2579-2591.

Arjonen, A., Kaukonen, R., Mattila, E., Rouhi, P., Hognas, G., Sihto, H., Miller, B.W., Morton, J.P., Bucher, E., Taimen, P.*, et al.* (2014). Mutant p53-associated myosin-X upregulation promotes breast cancer invasion and metastasis. The Journal of clinical investigation *124*, 1069-1082.

Aschenbrenner, L., Naccache, S.N., and Hasson, T. (2004). Uncoated endocytic vesicles require the unconventional myosin, Myo6, for rapid transport through actin barriers. Molecular biology of the cell *15*, 2253-2263.

Assad, J.A., Shepherd, G.M., and Corey, D.P. (1991). Tip-link integrity and mechanical transduction in vertebrate hair cells. Neuron *7*, 985-994.

Avenarius, M.R., Krey, J.F., Dumont, R.A., Morgan, C.P., Benson, C.B., Vijayakumar, S., Cunningham, C.L., Scheffer, D.I., Corey, D.P., Muller, U.*, et al.* (2017). Heterodimeric capping protein is required for stereocilia length and width regulation. The Journal of cell biology *216*, 3861-3881.

Baboolal, T.G., Mashanov, G.I., Nenasheva, T.A., Peckham, M., and Molloy, J.E. (2016). A Combination of Diffusion and Active Translocation Localizes Myosin 10 to the Filopodial Tip. The Journal of biological chemistry.

Bahloul, A., Michel, V., Hardelin, J.P., Nouaille, S., Hoos, S., Houdusse, A., England, P., and Petit, C. (2010). Cadherin-23, myosin VIIa and harmonin, encoded by Usher syndrome type I genes, form a ternary complex and interact with membrane phospholipids. Human molecular genetics *19*, 3557-3565.

Barker, N., van Es, J.H., Kuipers, J., Kujala, P., van den Born, M., Cozijnsen, M., Haegebarth, A., Korving, J., Begthel, H., Peters, P.J.*, et al.* (2007). Identification of stem cells in small intestine and colon by marker gene Lgr5. Nature *449*, 1003-1007.

Bartles, J.R., Zheng, L., Li, A., Wierda, A., and Chen, B. (1998). Small espin: a third actin-bundling protein and potential forked protein ortholog in brush border microvilli. The Journal of cell biology *143*, 107-119.

Bastie, M.J., Balas, D., Laval, J., Senegas-Balas, F., Bertrand, C., Frexinos, J., and Ribet, A. (1982). Histological variations of jejunal and ileal mucosa on days 8 and 15 after hypophysectomy in rat: morphometrical analysis on light and electron microscopy. Acta anatomica *112*, 321-337.

Basu, R., and Chang, F. (2011). Characterization of dip1p reveals a switch in Arp2/3-dependent actin assembly for fission yeast endocytosis. Current biology : CB *21*, 905-916.

Bathe, M., Heussinger, C., Claessens, M.M., Bausch, A.R., and Frey, E. (2008). Cytoskeletal bundle mechanics. Biophysical journal *94*, 2955-2964.

Batters, C., Arthur, C.P., Lin, A., Porter, J., Geeves, M.A., Milligan, R.A., Molloy, J.E., and Coluccio, L.M. (2004a). Myo1c is designed for the adaptation response in the inner ear. The EMBO journal *23*, 1433-1440.

Batters, C., Wallace, M.I., Coluccio, L.M., and Molloy, J.E. (2004b). A model of stereocilia adaptation based on single molecule mechanical studies of myosin I. Philosophical transactions of the Royal Society of London Series B, Biological sciences *359*, 1895-1905.

Bear, J.E., Svitkina, T.M., Krause, M., Schafer, D.A., Loureiro, J.J., Strasser, G.A., Maly, I.V., Chaga, O.Y., Cooper, J.A., Borisy, G.G.*, et al.* (2002). Antagonism between Ena/VASP proteins and actin filament capping regulates fibroblast motility. Cell *109*, 509-521.

Behlouli, A., Bonnet, C., Abdi, S., Bouaita, A., Lelli, A., Hardelin, J.P., Schietroma, C., Rous, Y., Louha, M., Cheknane, A.*, et al.* (2014). EPS8, encoding an actin-binding protein of cochlear hair cell stereocilia, is a new causal gene for autosomal recessive profound deafness. Orphanet journal of rare diseases *9*, 55.

Belyantseva, I.A., Boger, E.T., and Friedman, T.B. (2003). Myosin XVa localizes to the tips of inner ear sensory cell stereocilia and is essential for staircase formation of the hair bundle. Proceedings of the National Academy of Sciences of the United States of America *100*, 13958-13963.

Belyantseva, I.A., Boger, E.T., Naz, S., Frolenkov, G.I., Sellers, J.R., Ahmed, Z.M., Griffith, A.J., and Friedman, T.B. (2005). Myosin-XVa is required for tip localization of whirlin and differential elongation of hair-cell stereocilia. Nature cell biology *7*, 148-156.

Bement, W.M., Hasson, T., Wirth, J.A., Cheney, R.E., and Mooseker, M.S. (1994). Identification and overlapping expression of multiple unconventional myosin genes in vertebrate cell types. Proceedings of the National Academy of Sciences of the United States of America *91*, 6549-6553.

Benesh, A.E., Nambiar, R., McConnell, R.E., Mao, S., Tabb, D.L., and Tyska, M.J. (2010). Differential localization and dynamics of class I myosins in the enterocyte microvillus. Molecular biology of the cell *21*, 970-978.

Berg, J.S., and Cheney, R.E. (2002). Myosin-X is an unconventional myosin that undergoes intrafilopodial motility. Nature cell biology *4*, 246-250.

Berg, J.S., Derfler, B.H., Pennisi, C.M., Corey, D.P., and Cheney, R.E. (2000). Myosin-X, a novel myosin with pleckstrin homology domains, associates with regions of dynamic actin. Journal of cell science *113 Pt 19*, 3439-3451.

Beurg, M., Xiong, W., Zhao, B., Muller, U., and Fettiplace, R. (2015). Subunit determination of the conductance of hair-cell mechanotransducer channels. Proceedings of the National Academy of Sciences of the United States of America *112*, 1589-1594.

Bird, J.E., Barzik, M., Drummond, M.C., Sutton, D.C., Goodman, S.M., Morozko, E.L., Cole, S.M., Boukhvalova, A.K., Skidmore, J., Syam, D.*, et al.* (2017). Harnessing molecular motors for nanoscale pulldown in live cells. Molecular biology of the cell *28*, 463-475.

Bird, J.E., Takagi, Y., Billington, N., Strub, M.P., Sellers, J.R., and Friedman, T.B. (2014). Chaperone-enhanced purification of unconventional myosin 15, a molecular motor specialized for stereocilia protein trafficking. Proceedings of the National Academy of Sciences of the United States of America *111*, 12390-12395.

Bitner-Glindzicz, M., Lindley, K.J., Rutland, P., Blaydon, D., Smith, V.V., Milla, P.J., Hussain, K., Furth-Lavi, J., Cosgrove, K.E., Shepherd, R.M.*, et al.* (2000). A recessive

contiguous gene deletion causing infantile hyperinsulinism, enteropathy and deafness identifies the Usher type 1C gene. Nature genetics *26*, 56-60.

Boeda, B., El-Amraoui, A., Bahloul, A., Goodyear, R., Daviet, L., Blanchard, S., Perfettini, I., Fath, K.R., Shorte, S., Reiners, J.*, et al.* (2002). Myosin VIIa, harmonin and cadherin 23, three Usher I gene products that cooperate to shape the sensory hair cell bundle. The EMBO journal *21*, 6689-6699.

Bohil, A.B., Robertson, B.W., and Cheney, R.E. (2006). Myosin-X is a molecular motor that functions in filopodia formation. Proceedings of the National Academy of Sciences of the United States of America *103*, 12411-12416.

Bolz, H., von Brederlow, B., Ramirez, A., Bryda, E.C., Kutsche, K., Nothwang, H.G., Seeliger, M., del, C.S.C.M., Vila, M.C., Molina, O.P.*, et al.* (2001). Mutation of CDH23, encoding a new member of the cadherin gene family, causes Usher syndrome type 1D. Nature genetics *27*, 108-112.

Bork, J.M., Peters, L.M., Riazuddin, S., Bernstein, S.L., Ahmed, Z.M., Ness, S.L., Polomeno, R., Ramesh, A., Schloss, M., Srisailpathy, C.R.*, et al.* (2001). Usher syndrome 1D and nonsyndromic autosomal recessive deafness DFNB12 are caused by allelic mutations of the novel cadherin-like gene CDH23. American journal of human genetics *68*, 26-37.

Bose, A., Robida, S., Furcinitti, P.S., Chawla, A., Fogarty, K., Corvera, S., and Czech, M.P. (2004). Unconventional myosin Myo1c promotes membrane fusion in a regulated exocytic pathway. Molecular and cellular biology *24*, 5447-5458.

Boyne, R., Fell, B.F., and Robb, I. (1966). The surface area of the intestinal mucosa in the lactating rat. The Journal of physiology *183*, 570-575.

Brawley, C.M., and Rock, R.S. (2009). Unconventional myosin traffic in cells reveals a selective actin cytoskeleton. Proceedings of the National Academy of Sciences of the United States of America *106*, 9685-9690.

Bretscher, A., and Weber, K. (1979). Villin: the major microfilament-associated protein of the intestinal microvillus. Proceedings of the National Academy of Sciences of the United States of America *76*, 2321-2325.

Bretscher, A., and Weber, K. (1980). Fimbrin, a new microfilament-associated protein present in microvilli and other cell surface structures. The Journal of cell biology *86*, 335-340.

Brown, A.L., Jr. (1962). Microvilli of the human jejunal epithelial cell. The Journal of cell biology *12*, 623-627.

Burke, T.A., Christensen, J.R., Barone, E., Suarez, C., Sirotkin, V., and Kovar, D.R. (2014). Homeostatic actin cytoskeleton networks are regulated by assembly factor competition for monomers. Current biology : CB *24*, 579-585.

Buss, F., and Kendrick-Jones, J. (2011). Multifunctional myosin VI has a multitude of cargoes. Proceedings of the National Academy of Sciences of the United States of America *108*, 5927-5928.

Caberlotto, E., Michel, V., de Monvel, J.B., and Petit, C. (2011a). Coupling of the mechanotransduction machinery and F-actin polymerization in the cochlear hair bundles. Bioarchitecture *1*, 169-174.

Caberlotto, E., Michel, V., Foucher, I., Bahloul, A., Goodyear, R.J., Pepermans, E., Michalski, N., Perfettini, I., Alegria-Prevot, O., Chardenoux, S.*, et al.* (2011b). Usher type 1G protein sans is a critical component of the tip-link complex, a structure controlling actin polymerization in stereocilia. Proceedings of the National Academy of Sciences of the United States of America *108*, 5825-5830.

Cao, R., Chen, J., Zhang, X., Zhai, Y., Qing, X., Xing, W., Zhang, L., Malik, Y.S., Yu, H., and Zhu, X. (2014). Elevated expression of myosin X in tumours contributes to breast cancer aggressiveness and metastasis. British journal of cancer *111*, 539-550.

Chan, Y.H., and Marshall, W.F. (2012). How cells know the size of their organelles. Science *337*, 1186-1189.

Chen, L., Janetopoulos, C., Huang, Y.E., Iijima, M., Borleis, J., and Devreotes, P.N. (2003). Two phases of actin polymerization display different dependencies on PI(3,4,5)P3 accumulation and have unique roles during chemotaxis. Molecular biology of the cell *14*, 5028-5037.

Chen, T., Hubbard, A., Murtazina, R., Price, J., Yang, J., Cha, B., Sarker, R., and Donowitz, M. (2014). Myosin VI mediates the movement of NHE3 down the microvillus in intestinal epithelial cells. Journal of cell science *127*, 3535-3545.

Chen, Z.Y., Hasson, T., Zhang, D.S., Schwender, B.J., Derfler, B.H., Mooseker, M.S., and Corey, D.P. (2001). Myosin-VIIb, a novel unconventional myosin, is a constituent of microvilli in transporting epithelia. Genomics *72*, 285-296.

Chou, S.W., Hwang, P., Gomez, G., Fernando, C.A., West, M.C., Pollock, L.M., Lin-Jones, J., Burnside, B., and McDermott, B.M., Jr. (2011). Fascin 2b is a component of stereocilia that lengthens actin-based protrusions. PloS one *6*, e14807.

Claessens, M.M., Bathe, M., Frey, E., and Bausch, A.R. (2006). Actin-binding proteins sensitively mediate F-actin bundle stiffness. Nature materials *5*, 748-753.

Crawley, S.W., Mooseker, M.S., and Tyska, M.J. (2014a). Shaping the intestinal brush border. The Journal of cell biology *207*, 441-451.

Crawley, S.W., Shifrin, D.A., Jr., Grega-Larson, N.E., McConnell, R.E., Benesh, A.E., Mao, S., Zheng, Y., Zheng, Q.Y., Nam, K.T., Millis, B.A.*, et al.* (2014b). Intestinal brush border assembly driven by protocadherin-based intermicrovillar adhesion. Cell *157*, 433-446.

Crawley, S.W., Weck, M.L., Grega-Larson, N.E., Shifrin, D.A., Jr., and Tyska, M.J. (2016). ANKS4B Is Essential for Intermicrovillar Adhesion Complex Formation. Developmental cell *36*, 190-200.

Croce, A., Cassata, G., Disanza, A., Gagliani, M.C., Tacchetti, C., Malabarba, M.G., Carlier, M.F., Scita, G., Baumeister, R., and Di Fiore, P.P. (2004). A novel actin barbed-end-capping activity in EPS-8 regulates apical morphogenesis in intestinal cells of Caenorhabditis elegans. Nature cell biology *6*, 1173-1179.

Dai, J., Ting-Beall, H.P., Hochmuth, R.M., Sheetz, M.P., and Titus, M.A. (1999). Myosin I contributes to the generation of resting cortical tension. Biophysical journal *77*, 1168-1176.

Delprat, B., Michel, V., Goodyear, R., Yamasaki, Y., Michalski, N., El-Amraoui, A., Perfettini, I., Legrain, P., Richardson, G., Hardelin, J.P.*, et al.* (2005). Myosin XVa and whirlin, two deafness gene products required for hair bundle growth, are located at the stereocilia tips and interact directly. Human molecular genetics *14*, 401-410.

Diamond, J.M., Karasov, W.H., Cary, C., Enders, D., and Yung, R. (1984). Effect of dietary carbohydrate on monosaccharide uptake by mouse small intestine in vitro. The Journal of physiology *349*, 419-440.

Disanza, A., Bisi, S., Winterhoff, M., Milanesi, F., Ushakov, D.S., Kast, D., Marighetti, P., Romet-Lemonne, G., Muller, H.M., Nickel, W.*, et al.* (2013). CDC42 switches IRSp53 from inhibition of actin growth to elongation by clustering of VASP. The EMBO journal *32*, 2735-2750.

Disanza, A., Carlier, M.F., Stradal, T.E., Didry, D., Frittoli, E., Confalonieri, S., Croce, A., Wehland, J., Di Fiore, P.P., and Scita, G. (2004). Eps8 controls actin-based motility by capping the barbed ends of actin filaments. Nature cell biology *6*, 1180-1188.

Disanza, A., Mantoani, S., Hertzog, M., Gerboth, S., Frittoli, E., Steffen, A., Berhoerster, K., Kreienkamp, H.J., Milanesi, F., Di Fiore, P.P.*, et al.* (2006). Regulation of cell shape by Cdc42 is mediated by the synergic actin-bundling activity of the Eps8-IRSp53 complex. Nature cell biology *8*, 1337-1347.

Drummond, M.C., Barzik, M., Bird, J.E., Zhang, D.S., Lechene, C.P., Corey, D.P., Cunningham, L.L., and Friedman, T.B. (2015). Live-cell imaging of actin dynamics reveals mechanisms of stereocilia length regulation in the inner ear. Nature communications *6*, 6873.

Ebrahim, S., Avenarius, M.R., Grati, M., Krey, J.F., Windsor, A.M., Sousa, A.D., Ballesteros, A., Cui, R., Millis, B.A., Salles, F.T.*, et al.* (2016). Stereocilia-staircase spacing is influenced by myosin III motors and their cargoes espin-1 and espin-like. Nature communications *7*, 10833.

Fang, Q., Indzhykulian, A.A., Mustapha, M., Riordan, G.P., Dolan, D.F., Friedman, T.B., Belyantseva, I.A., Frolenkov, G.I., Camper, S.A., and Bird, J.E. (2015). The 133-kDa N-

terminal domain enables myosin 15 to maintain mechanotransducing stereocilia and is essential for hearing. eLife *4*.

Fawley, J., and Gourlay, D.M. (2016). Intestinal alkaline phosphatase: a summary of its role in clinical disease. The Journal of surgical research *202*, 225-234.

Fegan, A., White, B., Carlson, J.C., and Wagner, C.R. (2010). Chemically controlled protein assembly: techniques and applications. Chemical reviews *110*, 3315-3336.

Fisher, R.B., and Parsons, D.S. (1950). The gradient of mucosal surface area in the small intestine of the rat. Journal of anatomy *84*, 272-282.

Francis, S.P., Krey, J.F., Krystofiak, E.S., Cui, R., Nanda, S., Xu, W., Kachar, B., Barr-Gillespie, P.G., and Shin, J.B. (2015). A short splice form of Xin-actin binding repeat containing 2 (XIRP2) lacking the Xin repeats is required for maintenance of stereocilia morphology and hearing function. The Journal of neuroscience : the official journal of the Society for Neuroscience *35*, 1999-2014.

Franck, Z., Footer, M., and Bretscher, A. (1990). Microinjection of villin into cultured cells induces rapid and long-lasting changes in cell morphology but does not inhibit cytokinesis, cell motility, or membrane ruffling. The Journal of cell biology *111*, 2475-2485.

Friedman, T.B., Liang, Y., Weber, J.L., Hinnant, J.T., Barber, T.D., Winata, S., Arhya, I.N., and Asher, J.H., Jr. (1995). A gene for congenital, recessive deafness DFNB3 maps to the pericentromeric region of chromosome 17. Nature genetics *9*, 86-91.

Gibbs, D., Azarian, S.M., Lillo, C., Kitamoto, J., Klomp, A.E., Steel, K.P., Libby, R.T., and Williams, D.S. (2004). Role of myosin VIIa and Rab27a in the motility and localization of RPE melanosomes. Journal of cell science *117*, 6473-6483.

Goehring, N.W., and Hyman, A.A. (2012). Organelle growth control through limiting pools of cytoplasmic components. Current biology : CB *22*, R330-339.

Goldberg, M., Wei, M., Tycko, B., Falikovich, I., and Warburton, D. (2002). Identification and expression analysis of the human mu-protocadherin gene in fetal and adult kidneys. American journal of physiology Renal physiology *283*, F454-463.

Grati, M., and Kachar, B. (2011). Myosin VIIa and sans localization at stereocilia upper tip-link density implicates these Usher syndrome proteins in mechanotransduction. Proceedings of the National Academy of Sciences of the United States of America *108*, 11476-11481.

Grega-Larson, N.E., Crawley, S.W., Erwin, A.L., and Tyska, M.J. (2015). Cordon bleu promotes the assembly of brush border microvilli. Molecular biology of the cell *26*, 3803-3815.

Grega-Larson, N.E., Crawley, S.W., and Tyska, M.J. (2016). Impact of cordon-bleu expression on actin cytoskeleton architecture and dynamics. Cytoskeleton (Hoboken).

Grimm-Gunter, E.M., Revenu, C., Ramos, S., Hurbain, I., Smyth, N., Ferrary, E., Louvard, D., Robine, S., and Rivero, F. (2009). Plastin 1 binds to keratin and is required for terminal web assembly in the intestinal epithelium. Molecular biology of the cell *20*, 2549-2562.

Haithcock, J., Billington, N., Choi, K., Fordham, J., Sellers, J.R., Stafford, W.F., White, H., and Forgacs, E. (2011). The kinetic mechanism of mouse myosin VIIA. The Journal of biological chemistry *286*, 8819-8828.

Hansen, S.D., and Mullins, R.D. (2010). VASP is a processive actin polymerase that requires monomeric actin for barbed end association. The Journal of cell biology *191*, 571-584.

Hasson, T., Heintzelman, M.B., Santos-Sacchi, J., Corey, D.P., and Mooseker, M.S. (1995). Expression in cochlea and retina of myosin VIIa, the gene product defective in Usher syndrome type 1B. Proceedings of the National Academy of Sciences of the United States of America *92*, 9815-9819.

Hegan, P.S., Giral, H., Levi, M., and Mooseker, M.S. (2012). Myosin VI is required for maintenance of brush border structure, composition, and membrane trafficking functions in the intestinal epithelial cell. Cytoskeleton (Hoboken) *69*, 235-251.

Heintzelman, M.B., Hasson, T., and Mooseker, M.S. (1994). Multiple unconventional myosin domains of the intestinal brush border cytoskeleton. Journal of cell science *107 (Pt 12)*, 3535-3543.

Helander, H.F., and Fandriks, L. (2014). Surface area of the digestive tract - revisited. Scandinavian journal of gastroenterology *49*, 681-689.

Henn, A., and De La Cruz, E.M. (2005). Vertebrate myosin VIIb is a high duty ratio motor adapted for generating and maintaining tension. The Journal of biological chemistry *280*, 39665-39676.

Henson, J.H., Yeterian, M., Weeks, R.M., Medrano, A.E., Brown, B.L., Geist, H.L., Pais, M.D., Oldenbourg, R., and Shuster, C.B. (2015). Arp2/3 complex inhibition radically alters lamellipodial actin architecture, suspended cell shape, and the cell spreading process. Molecular biology of the cell *26*, 887-900.

Hertzog, M., Milanesi, F., Hazelwood, L., Disanza, A., Liu, H., Perlade, E., Malabarba, M.G., Pasqualato, S., Maiolica, A., Confalonieri, S.*, et al.* (2010). Molecular basis for the dual function of Eps8 on actin dynamics: bundling and capping. PLoS biology *8*, e1000387.

Heym, R.G., Zimmermann, D., Edelmann, F.T., Israel, L., Okten, Z., Kovar, D.R., and Niessing, D. (2013). In vitro reconstitution of an mRNA-transport complex reveals

mechanisms of assembly and motor activation. The Journal of cell biology *203*, 971-984.

Hirano, Y., Hatano, T., Takahashi, A., Toriyama, M., Inagaki, N., and Hakoshima, T. (2011). Structural basis of cargo recognition by the myosin-X MyTH4-FERM domain. The EMBO journal *30*, 2734-2747.

Hirokawa, N., Tilney, L.G., Fujiwara, K., and Heuser, J.E. (1982). Organization of actin, myosin, and intermediate filaments in the brush border of intestinal epithelial cells. The Journal of cell biology *94*, 425-443.

Holt, J.R., Gillespie, S.K., Provance, D.W., Shah, K., Shokat, K.M., Corey, D.P., Mercer, J.A., and Gillespie, P.G. (2002). A chemical-genetic strategy implicates myosin-1c in adaptation by hair cells. Cell *108*, 371-381.

Homma, K., and Ikebe, M. (2005). Myosin X is a high duty ratio motor. The Journal of biological chemistry *280*, 29381-29391.

Hotulainen, P., and Lappalainen, P. (2006). Stress fibers are generated by two distinct actin assembly mechanisms in motile cells. The Journal of cell biology *173*, 383-394.

Houdusse, A., and Cohen, C. (1995). Target sequence recognition by the calmodulin superfamily: implications from light chain binding to the regulatory domain of scallop myosin. Proceedings of the National Academy of Sciences of the United States of America *92*, 10644-10647.

Ingerman, E., Hsiao, J.Y., and Mullins, R.D. (2013). Arp2/3 complex ATP hydrolysis promotes lamellipodial actin network disassembly but is dispensable for assembly. The Journal of cell biology *200*, 619-633.

Inoue, A., and Ikebe, M. (2003). Characterization of the motor activity of mammalian myosin VIIA. The Journal of biological chemistry *278*, 5478-5487.

Insall, R.H., and Weiner, O.D. (2001). PIP3, PIP2, and cell movement--similar messages, different meanings? Developmental cell *1*, 743-747.

Ishikawa, T., Sato, T., Mohit, G., Imai, Y., and Yamaguchi, T. (2011). Transport phenomena of microbial flora in the small intestine with peristalsis. Journal of theoretical biology *279*, 63-73.

Johnston, A.M., Naselli, G., Niwa, H., Brodnicki, T., Harrison, L.C., and Gonez, L.J. (2004). Harp (harmonin-interacting, ankyrin repeat-containing protein), a novel protein that interacts with harmonin in epithelial tissues. Genes to cells : devoted to molecular & cellular mechanisms *9*, 967-982.

Jose, M., Tollis, S., Nair, D., Mitteau, R., Velours, C., Massoni-Laporte, A., Royou, A., Sibarita, J.B., and McCusker, D. (2015). A quantitative imaging-based screen reveals

the exocyst as a network hub connecting endocytosis and exocytosis. Molecular biology of the cell *26*, 2519-2534.

Kachar, B., Parakkal, M., Kurc, M., Zhao, Y., and Gillespie, P.G. (2000). High-resolution structure of hair-cell tip links. Proceedings of the National Academy of Sciences of the United States of America *97*, 13336-13341.

Kambara, T., Rhodes, T.E., Ikebe, R., Yamada, M., White, H.D., and Ikebe, M. (1999). Functional significance of the conserved residues in the flexible hinge region of the myosin motor domain. The Journal of biological chemistry *274*, 16400-16406.

Kazmierczak, P., Sakaguchi, H., Tokita, J., Wilson-Kubalek, E.M., Milligan, R.A., Muller, U., and Kachar, B. (2007). Cadherin 23 and protocadherin 15 interact to form tip-link filaments in sensory hair cells. Nature *449*, 87-91.

Kerber, M.L., Jacobs, D.T., Campagnola, L., Dunn, B.D., Yin, T., Sousa, A.D., Quintero, O.A., and Cheney, R.E. (2009). A novel form of motility in filopodia revealed by imaging myosin-X at the single-molecule level. Current biology : CB *19*, 967-973.

Khubchandani, S.R., Vohra, P., Chitale, A.R., and Sidana, P. (2011). Microvillous inclusion disease--an ultrastructural diagnosis: with a review of the literature. Ultrastructural pathology *35*, 87-91.

Kim, S.W., Ehrman, J., Ahn, M.R., Kondo, J., Lopez, A.A.M., Oh, Y.S., Kim, X.H., Crawley, S.W., Goldenring, J.R., Tyska, M.J.*, et al.* (2017). Shear stress induces noncanonical autophagy in intestinal epithelial monolayers. Molecular biology of the cell *28*, 3043-3056.

Kitajiri, S., Sakamoto, T., Belyantseva, I.A., Goodyear, R.J., Stepanyan, R., Fujiwara, I., Bird, J.E., Riazuddin, S., Riazuddin, S., Ahmed, Z.M.*, et al.* (2010). Actin-bundling protein TRIOBP forms resilient rootlets of hair cell stereocilia essential for hearing. Cell *141*, 786-798.

Knight, P.J., Thirumurugan, K., Xu, Y., Wang, F., Kalverda, A.P., Stafford, W.F., 3rd, Sellers, J.R., and Peckham, M. (2005). The predicted coiled-coil domain of myosin 10 forms a novel elongated domain that lengthens the head. The Journal of biological chemistry *280*, 34702-34708.

Koestler, S.A., Steffen, A., Nemethova, M., Winterhoff, M., Luo, N., Holleboom, J.M., Krupp, J., Jacob, S., Vinzenz, M., Schur, F.*, et al.* (2013). Arp2/3 complex is essential for actin network treadmilling as well as for targeting of capping protein and cofilin. Molecular biology of the cell *24*, 2861-2875.

Kros, C.J., Marcotti, W., van Netten, S.M., Self, T.J., Libby, R.T., Brown, S.D., Richardson, G.P., and Steel, K.P. (2002). Reduced climbing and increased slipping adaptation in cochlear hair cells of mice with Myo7a mutations. Nature neuroscience *5*, 41-47.

Kurima, K., Ebrahim, S., Pan, B., Sedlacek, M., Sengupta, P., Millis, B.A., Cui, R., Nakanishi, H., Fujikawa, T., Kawashima, Y.*, et al.* (2015). TMC1 and TMC2 Localize at the Site of Mechanotransduction in Mammalian Inner Ear Hair Cell Stereocilia. Cell reports *12*, 1606-1617.

Kuroda, T.S., and Fukuda, M. (2005). Functional analysis of Slac2-c/MyRIP as a linker protein between melanosomes and myosin VIIa. The Journal of biological chemistry *280*, 28015-28022.

Kwon, M., Bagonis, M., Danuser, G., and Pellman, D. (2015). Direct Microtubule-Binding by Myosin-10 Orients Centrosomes toward Retraction Fibers and Subcortical Actin Clouds. Developmental cell *34*, 323-337.

Lai, M., Guo, Y., Ma, J., Yu, H., Zhao, D., Fan, W., Ju, X., Sheikh, M.A., Malik, Y.S., Xiong, W.*, et al.* (2015). Myosin X regulates neuronal radial migration through interacting with N-cadherin. Frontiers in cellular neuroscience *9*, 326.

Leblond, C.P. (1981). The life history of cells in renewing systems. The American journal of anatomy *160*, 114-158.

Lebrand, C., Dent, E.W., Strasser, G.A., Lanier, L.M., Krause, M., Svitkina, T.M., Borisy, G.G., and Gertler, F.B. (2004). Critical role of Ena/VASP proteins for filopodia formation in neurons and in function downstream of netrin-1. Neuron *42*, 37-49.

Lefevre, G., Michel, V., Weil, D., Lepelletier, L., Bizard, E., Wolfrum, U., Hardelin, J.P., and Petit, C. (2008). A core cochlear phenotype in USH1 mouse mutants implicates fibrous links of the hair bundle in its cohesion, orientation and differential growth. Development *135*, 1427-1437.

Lentle, R.G., and Janssen, P.W. (2008). Physical characteristics of digesta and their influence on flow and mixing in the mammalian intestine: a review. Journal of comparative physiology B, Biochemical, systemic, and environmental physiology *178*, 673-690.

Li, J., He, Y., Lu, Q., and Zhang, M. (2016). Mechanistic Basis of Organization of the Harmonin/USH1C-Mediated Brush Border Microvilli Tip-Link Complex. Developmental cell *36*, 179-189.

Li, J., He, Y., Weck, M.L., Lu, Q., Tyska, M.J., and Zhang, M. (2017). Structure of Myo7b/USH1C complex suggests a general PDZ domain binding mode by MyTH4-FERM myosins. Proceedings of the National Academy of Sciences of the United States of America *114*, E3776-E3785.

Liang, Y., Wang, A., Belyantseva, I.A., Anderson, D.W., Probst, F.J., Barber, T.D., Miller, W., Touchman, J.W., Jin, L., Sullivan, S.L.*, et al.* (1999). Characterization of the human and mouse unconventional myosin XV genes responsible for hereditary deafness DFNB3 and shaker 2. Genomics *61*, 243-258.

Liu, H., Li, J., Raval, M.H., Yao, N., Deng, X., Lu, Q., Nie, S., Feng, W., Wan, J., Yengo, C.M.*, et al.* (2016). Myosin III-mediated cross-linking and stimulation of actin bundling activity of Espin. eLife *5*.

Liu, J., Taylor, D.W., Krementsova, E.B., Trybus, K.M., and Taylor, K.A. (2006). Three-dimensional structure of the myosin V inhibited state by cryoelectron tomography. Nature *442*, 208-211.

Liu, X., Ondek, B., and Williams, D.S. (1998). Mutant myosin VIIa causes defective melanosome distribution in the RPE of shaker-1 mice. Nature genetics *19*, 117-118.

Liu, X., Udovichenko, I.P., Brown, S.D., Steel, K.P., and Williams, D.S. (1999). Myosin VIIa participates in opsin transport through the photoreceptor cilium. The Journal of neuroscience : the official journal of the Society for Neuroscience *19*, 6267-6274.

Liu, X.Z., Walsh, J., Mburu, P., Kendrick-Jones, J., Cope, M.J., Steel, K.P., and Brown, S.D. (1997a). Mutations in the myosin VIIA gene cause non-syndromic recessive deafness. Nature genetics *16*, 188-190.

Liu, X.Z., Walsh, J., Tamagawa, Y., Kitamura, K., Nishizawa, M., Steel, K.P., and Brown, S.D. (1997b). Autosomal dominant non-syndromic deafness caused by a mutation in the myosin VIIA gene. Nature genetics *17*, 268-269.

Liu, Y., Peng, Y., Dai, P.G., Du, Q.S., Mei, L., and Xiong, W.C. (2012). Differential regulation of myosin X movements by its cargoes, DCC and neogenin. Journal of cell science *125*, 751-762.

Loomis, P.A., Zheng, L., Sekerkova, G., Changyaleket, B., Mugnaini, E., and Bartles, J.R. (2003). Espin cross-links cause the elongation of microvillus-type parallel actin bundles in vivo. The Journal of cell biology *163*, 1045-1055.

Lopes, V.S., Ramalho, J.S., Owen, D.M., Karl, M.O., Strauss, O., Futter, C.E., and Seabra, M.C. (2007). The ternary Rab27a-Myrip-Myosin VIIa complex regulates melanosome motility in the retinal pigment epithelium. Traffic *8*, 486-499.

Lu, Q., Ye, F., Wei, Z., Wen, Z., and Zhang, M. (2012). Antiparallel coiled-coil-mediated dimerization of myosin X. Proceedings of the National Academy of Sciences of the United States of America *109*, 17388-17393.

Maeda, R., Kindt, K.S., Mo, W., Morgan, C.P., Erickson, T., Zhao, H., Clemens-Grisham, R., Barr-Gillespie, P.G., and Nicolson, T. (2014). Tip-link protein protocadherin 15 interacts with transmembrane channel-like proteins TMC1 and TMC2. Proceedings of the National Academy of Sciences of the United States of America *111*, 12907-12912.

Maerker, T., van Wijk, E., Overlack, N., Kersten, F.F., McGee, J., Goldmann, T., Sehn, E., Roepman, R., Walsh, E.J., Kremer, H.*, et al.* (2008). A novel Usher protein network

at the periciliary reloading point between molecular transport machineries in vertebrate photoreceptor cells. Human molecular genetics *17*, 71-86.

Mallavarapu, A., and Mitchison, T. (1999). Regulated actin cytoskeleton assembly at filopodium tips controls their extension and retraction. The Journal of cell biology *146*, 1097-1106.

Manor, U., Disanza, A., Grati, M., Andrade, L., Lin, H., Di Fiore, P.P., Scita, G., and Kachar, B. (2011). Regulation of stereocilia length by myosin XVa and whirlin depends on the actin-regulatory protein Eps8. Current biology : CB *21*, 167-172.

Maroux, S., Coudrier, E., Feracci, H., Gorvel, J.P., and Louvard, D. (1988). Molecular organization of the intestinal brush border. Biochimie *70*, 1297-1306.

Mayhew, T.M. (1987). Quantitative ultrastructural study on the responses of microvilli along the small bowel to fasting. Journal of anatomy *154*, 237-243.

Mayhew, T.M. (1990). Striated brush border of intestinal absorptive epithelial cells: stereological studies on microvillous morphology in different adaptive states. Journal of electron microscopy technique *16*, 45-55.

Mayhew, T.M., and Middleton, C. (1985). Crypts, villi and microvilli in the small intestine of the rat. A stereological study of their variability within and between animals. Journal of anatomy *141*, 1-17.

Mburu, P., Liu, X.Z., Walsh, J., Saw, D., Jr., Cope, M.J., Gibson, F., Kendrick-Jones, J., Steel, K.P., and Brown, S.D. (1997). Mutation analysis of the mouse myosin VIIA deafness gene. Genes and function *1*, 191-203.

Mburu, P., Mustapha, M., Varela, A., Weil, D., El-Amraoui, A., Holme, R.H., Rump, A., Hardisty, R.E., Blanchard, S., Coimbra, R.S.*, et al.* (2003). Defects in whirlin, a PDZ domain molecule involved in stereocilia elongation, cause deafness in the whirler mouse and families with DFNB31. Nature genetics *34*, 421-428.

Mburu, P., Romero, M.R., Hilton, H., Parker, A., Townsend, S., Kikkawa, Y., and Brown, S.D. (2010). Gelsolin plays a role in the actin polymerization complex of hair cell stereocilia. PloS one *5*, e11627.

McConnell, R.E., Benesh, A.E., Mao, S., Tabb, D.L., and Tyska, M.J. (2011). Proteomic analysis of the enterocyte brush border. American journal of physiology Gastrointestinal and liver physiology *300*, G914-926.

McConnell, R.E., Higginbotham, J.N., Shifrin, D.A., Jr., Tabb, D.L., Coffey, R.J., and Tyska, M.J. (2009). The enterocyte microvillus is a vesicle-generating organelle. The Journal of cell biology *185*, 1285-1298.

McConnell, R.E., and Tyska, M.J. (2007). Myosin-1a powers the sliding of apical membrane along microvillar actin bundles. The Journal of cell biology *177*, 671-681.

McGee, J., Goodyear, R.J., McMillan, D.R., Stauffer, E.A., Holt, J.R., Locke, K.G., Birch, D.G., Legan, P.K., White, P.C., Walsh, E.J.*, et al.* (2006). The very large G-protein-coupled receptor VLGR1: a component of the ankle link complex required for the normal development of auditory hair bundles. The Journal of neuroscience : the official journal of the Society for Neuroscience *26*, 6543-6553.

McIntosh, B.B., Holzbaur, E.L., and Ostap, E.M. (2015). Control of the initiation and termination of kinesin-1-driven transport by myosin-Ic and nonmuscle tropomyosin. Current biology : CB *25*, 523-529.

McNally, E.M., Bravo-Zehnder, M.M., and Leinwand, L.A. (1991). Identification of sequences necessary for the association of cardiac myosin subunits. The Journal of cell biology *113*, 585-590.

Merritt, R.C., Manor, U., Salles, F.T., Grati, M., Dose, A.C., Unrath, W.C., Quintero, O.A., Yengo, C.M., and Kachar, B. (2012). Myosin IIIB uses an actin-binding motif in its espin-1 cargo to reach the tips of actin protrusions. Current biology : CB *22*, 320-325.

Michalski, N., Michel, V., Bahloul, A., Lefevre, G., Barral, J., Yagi, H., Chardenoux, S., Weil, D., Martin, P., Hardelin, J.P.*, et al.* (2007). Molecular characterization of the ankle-link complex in cochlear hair cells and its role in the hair bundle functioning. The Journal of neuroscience : the official journal of the Society for Neuroscience *27*, 6478-6488.

Miura, S., Sato, K., Kato-Negishi, M., Teshima, T., and Takeuchi, S. (2015). Fluid shear triggers microvilli formation via mechanosensitive activation of TRPV6. Nature communications *6*, 8871.

Mogilner, A., and Rubinstein, B. (2005). The physics of filopodial protrusion. Biophysical journal *89*, 782-795.

Montgomery, R.K., Carlone, D.L., Richmond, C.A., Farilla, L., Kranendonk, M.E., Henderson, D.E., Baffour-Awuah, N.Y., Ambruzs, D.M., Fogli, L.K., Algra, S.*, et al.* (2011). Mouse telomerase reverse transcriptase (mTert) expression marks slowly cycling intestinal stem cells. Proceedings of the National Academy of Sciences of the United States of America *108*, 179-184.

Mooseker, M.S., and Cheney, R.E. (1995). Unconventional myosins. Annual review of cell and developmental biology *11*, 633-675.

Mooseker, M.S., Pollard, T.D., and Wharton, K.A. (1982). Nucleated polymerization of actin from the membrane-associated ends of microvillar filaments in the intestinal brush border. The Journal of cell biology *95*, 223-233.

Mooseker, M.S., and Tilney, L.G. (1975). Organization of an actin filament-membrane complex. Filament polarity and membrane attachment in the microvilli of intestinal epithelial cells. The Journal of cell biology *67*, 725-743.

Morgan, C.P., Krey, J.F., Grati, M., Zhao, B., Fallen, S., Kannan-Sundhari, A., Liu, X.Z., Choi, D., Muller, U., and Barr-Gillespie, P.G. (2016). PDZD7-MYO7A complex identified in enriched stereocilia membranes. eLife *5*.

Murugesan, S., Hong, J., Yi, J., Li, D., Beach, J.R., Shao, L., Meinhardt, J., Madison, G., Wu, X., Betzig, E.*, et al.* (2016). Formin-generated actomyosin arcs propel T cell receptor microcluster movement at the immune synapse. The Journal of cell biology *215*, 383-399.

Nagy, S., Ricca, B.L., Norstrom, M.F., Courson, D.S., Brawley, C.M., Smithback, P.A., and Rock, R.S. (2008). A myosin motor that selects bundled actin for motility. Proceedings of the National Academy of Sciences of the United States of America *105*, 9616-9620.

Nakagawa, H., Miki, H., Nozumi, M., Takenawa, T., Miyamoto, S., Wehland, J., and Small, J.V. (2003). IRSp53 is colocalised with WAVE2 at the tips of protruding lamellipodia and filopodia independently of Mena. Journal of cell science *116*, 2577-2583.

Nakano, K., Kuwayama, H., Kawasaki, M., Numata, O., and Takaine, M. (2010). GMF is an evolutionarily developed Adf/cofilin-super family protein involved in the Arp2/3 complex-mediated organization of the actin cytoskeleton. Cytoskeleton (Hoboken) *67*, 373-382.

Nambiar, R., McConnell, R.E., and Tyska, M.J. (2009). Control of cell membrane tension by myosin-I. Proceedings of the National Academy of Sciences of the United States of America *106*, 11972-11977.

Narayanan, P., Chatterton, P., Ikeda, A., Ikeda, S., Corey, D.P., Ervasti, J.M., and Perrin, B.J. (2015). Length regulation of mechanosensitive stereocilia depends on very slow actin dynamics and filament-severing proteins. Nature communications *6*, 6855.

Nelson, S.R., Trybus, K.M., and Warshaw, D.M. (2014). Motor coupling through lipid membranes enhances transport velocities for ensembles of myosin Va. Proceedings of the National Academy of Sciences of the United States of America *111*, E3986-3995.

Nishio, M., Watanabe, K., Sasaki, J., Taya, C., Takasuga, S., Iizuka, R., Balla, T., Yamazaki, M., Watanabe, H., Itoh, R.*, et al.* (2007). Control of cell polarity and motility by the PtdIns(3,4,5)P3 phosphatase SHIP1. Nature cell biology *9*, 36-44.

Novak, K.D., Peterson, M.D., Reedy, M.C., and Titus, M.A. (1995). Dictyostelium myosin I double mutants exhibit conditional defects in pinocytosis. The Journal of cell biology *131*, 1205-1221.

O'Shea, E.K., Klemm, J.D., Kim, P.S., and Alber, T. (1991). X-ray structure of the GCN4 leucine zipper, a two-stranded, parallel coiled coil. Science *254*, 539-544.

Odronitz, F., and Kollmar, M. (2007). Drawing the tree of eukaryotic life based on the analysis of 2,269 manually annotated myosins from 328 species. Genome biology *8*, R196.

Ohta, K., Higashi, R., Sawaguchi, A., and Nakamura, K. (2012). Helical arrangement of filaments in microvillar actin bundles. Journal of structural biology *177*, 513-519.

Okazaki, N., Takahashi, N., Kojima, S., Masuho, Y., and Koga, H. (2002). Protocadherin LKC, a new candidate for a tumor suppressor of colon and liver cancers, its association with contact inhibition of cell proliferation. Carcinogenesis *23*, 1139-1148.

Pan, B., Geleoc, G.S., Asai, Y., Horwitz, G.C., Kurima, K., Ishikawa, K., Kawashima, Y., Griffith, A.J., and Holt, J.R. (2013). TMC1 and TMC2 are components of the mechanotransduction channel in hair cells of the mammalian inner ear. Neuron *79*, 504-515.

Pan, L., Yan, J., Wu, L., and Zhang, M. (2009). Assembling stable hair cell tip link complex via multidentate interactions between harmonin and cadherin 23. Proceedings of the National Academy of Sciences of the United States of America *106*, 5575-5580.

Pan, L., and Zhang, M. (2012). Structures of usher syndrome 1 proteins and their complexes. Physiology *27*, 25-42.

Park, H., Ramamurthy, B., Travaglia, M., Safer, D., Chen, L.Q., Franzini-Armstrong, C., Selvin, P.R., and Sweeney, H.L. (2006). Full-length myosin VI dimerizes and moves processively along actin filaments upon monomer clustering. Molecular cell *21*, 331-336.

Pellegrin, S., and Mellor, H. (2005). The Rho family GTPase Rif induces filopodia through mDia2. Current biology : CB *15*, 129-133.

Peng, A.W., Belyantseva, I.A., Hsu, P.D., Friedman, T.B., and Heller, S. (2009). Twinfilin 2 regulates actin filament lengths in cochlear stereocilia. The Journal of neuroscience : the official journal of the Society for Neuroscience *29*, 15083-15088.

Perrin, B.J., Strandjord, D.M., Narayanan, P., Henderson, D.M., Johnson, K.R., and Ervasti, J.M. (2013). beta-Actin and fascin-2 cooperate to maintain stereocilia length. The Journal of neuroscience : the official journal of the Society for Neuroscience *33*, 8114-8121.

Phichith, D., Travaglia, M., Yang, Z., Liu, X., Zong, A.B., Safer, D., and Sweeney, H.L. (2009). Cargo binding induces dimerization of myosin VI. Proceedings of the National Academy of Sciences of the United States of America *106*, 17320-17324.

Pi, X., Ren, R., Kelley, R., Zhang, C., Moser, M., Bohil, A.B., Divito, M., Cheney, R.E., and Patterson, C. (2007). Sequential roles for myosin-X in BMP6-dependent filopodial extension, migration, and activation of BMP receptors. The Journal of cell biology *179*, 1569-1582.

Pickles, J.O., Comis, S.D., and Osborne, M.P. (1984). Cross-links between stereocilia in the guinea pig organ of Corti, and their possible relation to sensory transduction. Hearing research *15*, 103-112.

Planelles-Herrero, V.J., Blanc, F., Sirigu, S., Sirkia, H., Clause, J., Sourigues, Y., Johnsrud, D.O., Amigues, B., Cecchini, M., Gilbert, S.P.*, et al.* (2016). Myosin MyTH4-FERM structures highlight important principles of convergent evolution. Proceedings of the National Academy of Sciences of the United States of America *113*, E2906-2915.

Plantard, L., Arjonen, A., Lock, J.G., Nurani, G., Ivaska, J., and Stromblad, S. (2010). PtdIns(3,4,5)P(3) is a regulator of myosin-X localization and filopodia formation. Journal of cell science *123*, 3525-3534.

Pollard, T.D., and Mooseker, M.S. (1981). Direct measurement of actin polymerization rate constants by electron microscopy of actin filaments nucleated by isolated microvillus cores. The Journal of cell biology *88*, 654-659.

Postema, M.P., Grega-Larson, N.E., Neininger, A.C., and Tyska, M.J. (2018). IRTKS elongates epithelial microvilli using EPS8-dependent and independent mechanisms. In Current Biology: under review.

Powell, A.E., Wang, Y., Li, Y., Poulin, E.J., Means, A.L., Washington, M.K., Higginbotham, J.N., Juchheim, A., Prasad, N., Levy, S.E.*, et al.* (2012). The pan-ErbB negative regulator Lrig1 is an intestinal stem cell marker that functions as a tumor suppressor. Cell *149*, 146-158.

Probst, F.J., Fridell, R.A., Raphael, Y., Saunders, T.L., Wang, A., Liang, Y., Morell, R.J., Touchman, J.W., Lyons, R.H., Noben-Trauth, K.*, et al.* (1998). Correction of deafness in shaker-2 mice by an unconventional myosin in a BAC transgene. Science *280*, 1444-1447.

Prost, J., Barbetta, C., and Joanny, J.F. (2007). Dynamical control of the shape and size of stereocilia and microvilli. Biophysical journal *93*, 1124-1133.

Putyrski, M., and Schultz, C. (2012). Protein translocation as a tool: The current rapamycin story. FEBS letters *586*, 2097-2105.

Revenu, C., Ubelmann, F., Hurbain, I., El-Marjou, F., Dingli, F., Loew, D., Delacour, D., Gilet, J., Brot-Laroche, E., Rivero, F.*, et al.* (2012). A new role for the architecture of microvillar actin bundles in apical retention of membrane proteins. Molecular biology of the cell *23*, 324-336.

Riazuddin, S., Belyantseva, I.A., Giese, A.P., Lee, K., Indzhykulian, A.A., Nandamuri, S.P., Yousaf, R., Sinha, G.P., Lee, S., Terrell, D.*, et al.* (2012). Alterations of the CIB2 calcium- and integrin-binding protein cause Usher syndrome type 1J and nonsyndromic deafness DFNB48. Nature genetics *44*, 1265-1271.

Ricca, B.L., and Rock, R.S. (2010). The stepping pattern of myosin X is adapted for processive motility on bundled actin. Biophysical journal *99*, 1818-1826.

Richards, T.A., and Cavalier-Smith, T. (2005). Myosin domain evolution and the primary divergence of eukaryotes. Nature *436*, 1113-1118.

Rogers, S.L., Wiedemann, U., Stuurman, N., and Vale, R.D. (2003). Molecular requirements for actin-based lamella formation in Drosophila S2 cells. The Journal of cell biology *162*, 1079-1088.

Ropars, V., Yang, Z., Isabet, T., Blanc, F., Zhou, K., Lin, T., Liu, X., Hissier, P., Samazan, F., Amigues, B.*, et al.* (2016). The myosin X motor is optimized for movement on actin bundles. Nature communications *7*, 12456.

Rotty, J.D., Wu, C., Haynes, E.M., Suarez, C., Winkelman, J.D., Johnson, H.E., Haugh, J.M., Kovar, D.R., and Bear, J.E. (2015). Profilin-1 serves as a gatekeeper for actin assembly by Arp2/3-dependent and -independent pathways. Developmental cell *32*, 54-67.

Rzadzinska, A.K., Schneider, M.E., Davies, C., Riordan, G.P., and Kachar, B. (2004). An actin molecular treadmill and myosins maintain stereocilia functional architecture and self-renewal. The Journal of cell biology *164*, 887-897.

Sakai, T., Jung, H.S., Sato, O., Yamada, M.D., You, D.J., Ikebe, R., and Ikebe, M. (2015). Structure and Regulation of the Movement of Human Myosin VIIA. The Journal of biological chemistry *290*, 17587-17598.

Sakai, T., Umeki, N., Ikebe, R., and Ikebe, M. (2011). Cargo binding activates myosin VIIA motor function in cells. Proceedings of the National Academy of Sciences of the United States of America *108*, 7028-7033.

Salles, F.T., Merritt, R.C., Jr., Manor, U., Dougherty, G.W., Sousa, A.D., Moore, J.E., Yengo, C.M., Dose, A.C., and Kachar, B. (2009). Myosin IIIa boosts elongation of stereocilia by transporting espin 1 to the plus ends of actin filaments. Nature cell biology *11*, 443-450.

Sangiorgi, E., and Capecchi, M.R. (2008). Bmi1 is expressed in vivo in intestinal stem cells. Nature genetics *40*, 915-920.

Sarmiento, C., Wang, W., Dovas, A., Yamaguchi, H., Sidani, M., El-Sibai, M., Desmarais, V., Holman, H.A., Kitchen, S., Backer, J.M.*, et al.* (2008). WASP family members and formin proteins coordinate regulation of cell protrusions in carcinoma cells. The Journal of cell biology *180*, 1245-1260.

Sasaki, N., Ohkura, R., and Sutoh, K. (2003). Dictyostelium myosin II mutations that uncouple the converter swing and ATP hydrolysis cycle. Biochemistry *42*, 90-95.

Sasaki, N., Shimada, T., and Sutoh, K. (1998). Mutational analysis of the switch II loop of Dictyostelium myosin II. The Journal of biological chemistry *273*, 20334-20340.

Sato, T., van Es, J.H., Snippert, H.J., Stange, D.E., Vries, R.G., van den Born, M., Barker, N., Shroyer, N.F., van de Wetering, M., and Clevers, H. (2011). Paneth cells constitute the niche for Lgr5 stem cells in intestinal crypts. Nature *469*, 415-418.

Scheffer, D.I., Zhang, D.S., Shen, J., Indzhykulian, A., Karavitaki, K.D., Xu, Y.J., Wang, Q., Lin, J.J., Chen, Z.Y., and Corey, D.P. (2015). XIRP2, an actin-binding protein essential for inner ear hair-cell stereocilia. Cell reports *10*, 1811-1818.

Schirenbeck, A., Arasada, R., Bretschneider, T., Schleicher, M., and Faix, J. (2005a). Formins and VASPs may co-operate in the formation of filopodia. Biochemical Society transactions *33*, 1256-1259.

Schirenbeck, A., Bretschneider, T., Arasada, R., Schleicher, M., and Faix, J. (2005b). The Diaphanous-related formin dDia2 is required for the formation and maintenance of filopodia. Nature cell biology *7*, 619-625.

Schneider, M.E., Belyantseva, I.A., Azevedo, R.B., and Kachar, B. (2002). Rapid renewal of auditory hair bundles. Nature *418*, 837-838.

Sckolnick, M., Krementsova, E.B., Warshaw, D.M., and Trybus, K.M. (2013). More than just a cargo adapter, melanophilin prolongs and slows processive runs of myosin Va. The Journal of biological chemistry *288*, 29313-29322.

Self, T., Mahony, M., Fleming, J., Walsh, J., Brown, S.D., and Steel, K.P. (1998). Shaker-1 mutations reveal roles for myosin VIIA in both development and function of cochlear hair cells. Development *125*, 557-566.

Self, T., Sobe, T., Copeland, N.G., Jenkins, N.A., Avraham, K.B., and Steel, K.P. (1999). Role of myosin VI in the differentiation of cochlear hair cells. Developmental biology *214*, 331-341.

Senften, M., Schwander, M., Kazmierczak, P., Lillo, C., Shin, J.B., Hasson, T., Geleoc, G.S., Gillespie, P.G., Williams, D., Holt, J.R.*, et al.* (2006). Physical and functional interaction between protocadherin 15 and myosin VIIa in mechanosensory hair cells. The Journal of neuroscience : the official journal of the Society for Neuroscience *26*, 2060-2071.

Shifrin, D.A., Jr., McConnell, R.E., Nambiar, R., Higginbotham, J.N., Coffey, R.J., and Tyska, M.J. (2012). Enterocyte microvillus-derived vesicles detoxify bacterial products and regulate epithelial-microbial interactions. Current biology : CB *22*, 627-631.

Shimada, T., Sasaki, N., Ohkura, R., and Sutoh, K. (1997). Alanine scanning mutagenesis of the switch I region in the ATPase site of Dictyostelium discoideum myosin II. Biochemistry *36*, 14037-14043.

Shin, J.B., Longo-Guess, C.M., Gagnon, L.H., Saylor, K.W., Dumont, R.A., Spinelli, K.J., Pagana, J.M., Wilmarth, P.A., David, L.L., Gillespie, P.G.*, et al.* (2010). The R109H variant of fascin-2, a developmentally regulated actin crosslinker in hair-cell stereocilia, underlies early-onset hearing loss of DBA/2J mice. The Journal of neuroscience : the official journal of the Society for Neuroscience *30*, 9683-9694.

Siemens, J., Kazmierczak, P., Reynolds, A., Sticker, M., Littlewood-Evans, A., and Muller, U. (2002). The Usher syndrome proteins cadherin 23 and harmonin form a complex by means of PDZ-domain interactions. Proceedings of the National Academy of Sciences of the United States of America *99*, 14946-14951.

Sladewski, T.E., Bookwalter, C.S., Hong, M.S., and Trybus, K.M. (2013). Single-molecule reconstitution of mRNA transport by a class V myosin. Nature structural & molecular biology *20*, 952-957.

Slepecky, N., and Chamberlain, S.C. (1985). Immunoelectron microscopic and immunofluorescent localization of cytoskeletal and muscle-like contractile proteins in inner ear sensory hair cells. Hearing research *20*, 245-260.

Sotomayor, M., Weihofen, W.A., Gaudet, R., and Corey, D.P. (2012). Structure of a force-conveying cadherin bond essential for inner-ear mechanotransduction. Nature *492*, 128-132.

Stauffer, E.A., Scarborough, J.D., Hirono, M., Miller, E.D., Shah, K., Mercer, J.A., Holt, J.R., and Gillespie, P.G. (2005). Fast adaptation in vestibular hair cells requires myosin-1c activity. Neuron *47*, 541-553.

Stenling, R., Hagg, E., and Falkmer, S. (1984). Stereological studies on the rat small intestinal epithelium. III. Effects of short-term alloxan diabetes. Virchows Archiv B, Cell pathology including molecular pathology *47*, 263-270.

Stenling, R., and Helander, H.F. (1981). Stereological studies on the small intestinal epithelium of the rat. 1. The absorptive cells of the normal duodenum and jejunum. Cell and tissue research *217*, 11-21.

Suarez, C., and Kovar, D.R. (2016). Internetwork competition for monomers governs actin cytoskeleton organization. Nature reviews Molecular cell biology *17*, 799-810.

Sun, Y., Sato, O., Ruhnow, F., Arsenault, M.E., Ikebe, M., and Goldman, Y.E. (2010). Single-molecule stepping and structural dynamics of myosin X. Nature structural & molecular biology *17*, 485-491.

Suraneni, P., Fogelson, B., Rubinstein, B., Noguera, P., Volkmann, N., Hanein, D., Mogilner, A., and Li, R. (2015). A mechanism of leading-edge protrusion in the absence of Arp2/3 complex. Molecular biology of the cell *26*, 901-912.

Svitkina, T.M., Bulanova, E.A., Chaga, O.Y., Vignjevic, D.M., Kojima, S., Vasiliev, J.M., and Borisy, G.G. (2003). Mechanism of filopodia initiation by reorganization of a dendritic network. The Journal of cell biology *160*, 409-421.

Takeda, N., Jain, R., LeBoeuf, M.R., Wang, Q., Lu, M.M., and Epstein, J.A. (2011). Interconversion between intestinal stem cell populations in distinct niches. Science *334*, 1420-1424.

Taylor, R., Bullen, A., Johnson, S.L., Grimm-Gunter, E.M., Rivero, F., Marcotti, W., Forge, A., and Daudet, N. (2015). Absence of plastin 1 causes abnormal maintenance of hair cell stereocilia and a moderate form of hearing loss in mice. Human molecular genetics *24*, 37-49.

Tian, C., Liu, X.Z., Han, F., Yu, H., Longo-Guess, C., Yang, B., Lu, C., Yan, D., and Zheng, Q.Y. (2010). Ush1c gene expression levels in the ear and eye suggest different roles for Ush1c in neurosensory organs in a new Ush1c knockout mouse. Brain research *1328*, 57-70.

Tilney, L.G., Cotanche, D.A., and Tilney, M.S. (1992). Actin filaments, stereocilia and hair cells of the bird cochlea. VI. How the number and arrangement of stereocilia are determined. Development *116*, 213-226.

Tilney, L.G., and DeRosier, D.J. (1986). Actin filaments, stereocilia, and hair cells of the bird cochlea. IV. How the actin filaments become organized in developing stereocilia and in the cuticular plate. Developmental biology *116*, 119-129.

Tilney, L.G., Egelman, E.H., DeRosier, D.J., and Saunder, J.C. (1983). Actin filaments, stereocilia, and hair cells of the bird cochlea. II. Packing of actin filaments in the stereocilia and in the cuticular plate and what happens to the organization when the stereocilia are bent. The Journal of cell biology *96*, 822-834.

Tilney, L.G., and Saunders, J.C. (1983). Actin filaments, stereocilia, and hair cells of the bird cochlea. I. Length, number, width, and distribution of stereocilia of each hair cell are related to the position of the hair cell on the cochlea. The Journal of cell biology *96*, 807-821.

Tilney, L.G., Tilney, M.S., and Cotanche, D.A. (1988). Actin filaments, stereocilia, and hair cells of the bird cochlea. V. How the staircase pattern of stereociliary lengths is generated. The Journal of cell biology *106*, 355-365.

Tilney, L.G., Tilney, M.S., Saunders, J.S., and DeRosier, D.J. (1986). Actin filaments, stereocilia, and hair cells of the bird cochlea. III. The development and differentiation of hair cells and stereocilia. Developmental biology *116*, 100-118.

Tocchetti, A., Soppo, C.B., Zani, F., Bianchi, F., Gagliani, M.C., Pozzi, B., Rozman, J., Elvert, R., Ehrhardt, N., Rathkolb, B.*, et al.* (2010). Loss of the actin remodeler Eps8 causes intestinal defects and improved metabolic status in mice. PloS one *5*, e9468.

Tokuo, H., and Ikebe, M. (2004). Myosin X transports Mena/VASP to the tip of filopodia. Biochemical and biophysical research communications *319*, 214-220.

Tokuo, H., Mabuchi, K., and Ikebe, M. (2007). The motor activity of myosin-X promotes actin fiber convergence at the cell periphery to initiate filopodia formation. The Journal of cell biology *179*, 229-238.

Tsuprun, V., Goodyear, R.J., and Richardson, G.P. (2004). The structure of tip links and kinocilial links in avian sensory hair bundles. Biophysical journal *87*, 4106-4112.

Tuxworth, R.I., Weber, I., Wessels, D., Addicks, G.C., Soll, D.R., Gerisch, G., and Titus, M.A. (2001). A role for myosin VII in dynamic cell adhesion. Current biology : CB *11*, 318-329.

Tyska, M.J., Mackey, A.T., Huang, J.D., Copeland, N.G., Jenkins, N.A., and Mooseker, M.S. (2005). Myosin-1a is critical for normal brush border structure and composition. Molecular biology of the cell *16*, 2443-2457.

Tyska, M.J., and Mooseker, M.S. (2002). MYO1A (brush border myosin I) dynamics in the brush border of LLC-PK1-CL4 cells. Biophysical journal *82*, 1869-1883.

Umeki, N., Jung, H.S., Sakai, T., Sato, O., Ikebe, R., and Ikebe, M. (2011). Phospholipid-dependent regulation of the motor activity of myosin X. Nature structural & molecular biology *18*, 783-788.

Umeki, N., Jung, H.S., Watanabe, S., Sakai, T., Li, X.D., Ikebe, R., Craig, R., and Ikebe, M. (2009). The tail binds to the head-neck domain, inhibiting ATPase activity of myosin VIIA. Proceedings of the National Academy of Sciences of the United States of America *106*, 8483-8488.

Vallance, B.A., Chan, C., Robertson, M.L., and Finlay, B.B. (2002). Enteropathogenic and enterohemorrhagic Escherichia coli infections: emerging themes in pathogenesis and prevention. Canadian journal of gastroenterology = Journal canadien de gastroenterologie *16*, 771-778.

van Dongen, J.M., Visser, W.J., Daems, W.T., and Galjaard, H. (1976). The relation between cell proliferation, differentiation and ultrastructural development in rat intestinal epithelium. Cell and tissue research *174*, 183-199.

Velez-Ortega, A.C., Freeman, M.J., Indzhykulian, A.A., Grossheim, J.M., and Frolenkov, G.I. (2017). Mechanotransduction current is essential for stability of the transducing stereocilia in mammalian auditory hair cells. eLife *6*.

Verpy, E., Leibovici, M., Zwaenepoel, I., Liu, X.Z., Gal, A., Salem, N., Mansour, A., Blanchard, S., Kobayashi, I., Keats, B.J.*, et al.* (2000). A defect in harmonin, a PDZ domain-containing protein expressed in the inner ear sensory hair cells, underlies Usher syndrome type 1C. Nature genetics *26*, 51-55.

Vignjevic, D., Kojima, S., Aratyn, Y., Danciu, O., Svitkina, T., and Borisy, G.G. (2006). Role of fascin in filopodial protrusion. The Journal of cell biology *174*, 863-875.

Walker, M.L., Burgess, S.A., Sellers, J.R., Wang, F., Hammer, J.A., 3rd, Trinick, J., and Knight, P.J. (2000). Two-headed binding of a processive myosin to F-actin. Nature *405*, 804-807.

Wang, A., Liang, Y., Fridell, R.A., Probst, F.J., Wilcox, E.R., Touchman, J.W., Morton, C.C., Morell, R.J., Noben-Trauth, K., Camper, S.A.*, et al.* (1998). Association of unconventional myosin MYO15 mutations with human nonsyndromic deafness DFNB3. Science *280*, 1447-1451.

Watanabe, S., Ikebe, R., and Ikebe, M. (2006). Drosophila myosin VIIA is a high duty ratio motor with a unique kinetic mechanism. The Journal of biological chemistry *281*, 7151-7160.

Wayt, J., and Bretscher, A. (2014). Cordon Bleu serves as a platform at the basal region of microvilli, where it regulates microvillar length through its WH2 domains. Molecular biology of the cell *25*, 2817-2827.

Weber, K.L., Sokac, A.M., Berg, J.S., Cheney, R.E., and Bement, W.M. (2004). A microtubule-binding myosin required for nuclear anchoring and spindle assembly. Nature *431*, 325-329.

Weck, M.L., Crawley, S.W., Stone, C.R., and Tyska, M.J. (2016). Myosin-7b Promotes Distal Tip Localization of the Intermicrovillar Adhesion Complex. Current biology : CB.

Wei, Z., Yan, J., Lu, Q., Pan, L., and Zhang, M. (2011). Cargo recognition mechanism of myosin X revealed by the structure of its tail MyTH4-FERM tandem in complex with the DCC P3 domain. Proceedings of the National Academy of Sciences of the United States of America *108*, 3572-3577.

Weil, D., Blanchard, S., Kaplan, J., Guilford, P., Gibson, F., Walsh, J., Mburu, P., Varela, A., Levilliers, J., Weston, M.D.*, et al.* (1995). Defective myosin VIIA gene responsible for Usher syndrome type 1B. Nature *374*, 60-61.

Weil, D., El-Amraoui, A., Masmoudi, S., Mustapha, M., Kikkawa, Y., Laine, S., Delmaghani, S., Adato, A., Nadifi, S., Zina, Z.B.*, et al.* (2003). Usher syndrome type I G (USH1G) is caused by mutations in the gene encoding SANS, a protein that associates with the USH1C protein, harmonin. Human molecular genetics *12*, 463-471.

Weil, D., Kussel, P., Blanchard, S., Levy, G., Levi-Acobas, F., Drira, M., Ayadi, H., and Petit, C. (1997). The autosomal recessive isolated deafness, DFNB2, and the Usher 1B syndrome are allelic defects of the myosin-VIIA gene. Nature genetics *16*, 191-193.

Wells, A.L., Lin, A.W., Chen, L.Q., Safer, D., Cain, S.M., Hasson, T., Carragher, B.O., Milligan, R.A., and Sweeney, H.L. (1999). Myosin VI is an actin-based motor that moves backwards. Nature *401*, 505-508.

Weston, M.D., Kelley, P.M., Overbeck, L.D., Wagenaar, M., Orten, D.J., Hasson, T., Chen, Z.Y., Corey, D., Mooseker, M., Sumegi, J.*, et al.* (1996). Myosin VIIA mutation screening in 189 Usher syndrome type 1 patients. American journal of human genetics *59*, 1074-1083.

Willet, A.H., McDonald, N.A., Bohnert, K.A., Baird, M.A., Allen, J.R., Davidson, M.W., and Gould, K.L. (2015). The F-BAR Cdc15 promotes contractile ring formation through the direct recruitment of the formin Cdc12. The Journal of cell biology *208*, 391-399.

Wilson, W., Scott, R.B., Pinto, A., and Robertson, M.A. (2001). Intractable diarrhea in a newborn infant: microvillous inclusion disease. Canadian journal of gastroenterology = Journal canadien de gastroenterologie *15*, 61-64.

Woolner, S., O'Brien, L.L., Wiese, C., and Bement, W.M. (2008). Myosin-10 and actin filaments are essential for mitotic spindle function. The Journal of cell biology *182*, 77-88.

Wu, C., Asokan, S.B., Berginski, M.E., Haynes, E.M., Sharpless, N.E., Griffith, J.D., Gomez, S.M., and Bear, J.E. (2012a). Arp2/3 is critical for lamellipodia and response to extracellular matrix cues but is dispensable for chemotaxis. Cell *148*, 973-987.

Wu, L., Pan, L., Wei, Z., and Zhang, M. (2011). Structure of MyTH4-FERM domains in myosin VIIa tail bound to cargo. Science *331*, 757-760.

Wu, L., Pan, L., Zhang, C., and Zhang, M. (2012b). Large protein assemblies formed by multivalent interactions between cadherin23 and harmonin suggest a stable anchorage structure at the tip link of stereocilia. The Journal of biological chemistry *287*, 33460-33471.

Wu, X., Sakamoto, T., Zhang, F., Sellers, J.R., and Hammer, J.A., 3rd (2006). In vitro reconstitution of a transport complex containing Rab27a, melanophilin and myosin Va. FEBS letters *580*, 5863-5868.

Yan, J., Pan, L., Chen, X., Wu, L., and Zhang, M. (2010). The structure of the harmonin/sans complex reveals an unexpected interaction mode of the two Usher syndrome proteins. Proceedings of the National Academy of Sciences of the United States of America *107*, 4040-4045.

Yang, C., and Svitkina, T. (2011). Filopodia initiation: focus on the Arp2/3 complex and formins. Cell adhesion & migration *5*, 402-408.

Yang, Q., Zhang, X.F., Pollard, T.D., and Forscher, P. (2012). Arp2/3 complex-dependent actin networks constrain myosin II function in driving retrograde actin flow. The Journal of cell biology *197*, 939-956.

Yang, Y., Baboolal, T.G., Siththanandan, V., Chen, M., Walker, M.L., Knight, P.J., Peckham, M., and Sellers, J.R. (2009). A FERM domain autoregulates Drosophila

myosin 7a activity. Proceedings of the National Academy of Sciences of the United States of America *106*, 4189-4194.

Yang, Y., Kovacs, M., Sakamoto, T., Zhang, F., Kiehart, D.P., and Sellers, J.R. (2006). Dimerized Drosophila myosin VIIa: a processive motor. Proceedings of the National Academy of Sciences of the United States of America *103*, 5746-5751.

Yang, Y., Kovacs, M., Xu, Q., Anderson, J.B., and Sellers, J.R. (2005). Myosin VIIB from Drosophila is a high duty ratio motor. The Journal of biological chemistry *280*, 32061-32068.

Yu, C., Feng, W., Wei, Z., Miyanoiri, Y., Wen, W., Zhao, Y., and Zhang, M. (2009). Myosin VI undergoes cargo-mediated dimerization. Cell *138*, 537-548.

Yu, I.M., Planelles-Herrero, V.J., Sourigues, Y., Moussaoui, D., Sirkia, H., Kikuti, C., Stroebel, D., Titus, M.A., and Houdusse, A. (2017). Myosin 7 and its adaptors link cadherins to actin. Nature communications *8*, 15864.

Zampini, V., Ruttiger, L., Johnson, S.L., Franz, C., Furness, D.N., Waldhaus, J., Xiong, H., Hackney, C.M., Holley, M.C., Offenhauser, N.*, et al.* (2011). Eps8 regulates hair bundle length and functional maturation of mammalian auditory hair cells. PLoS biology *9*, e1001048.

Zhang, H., Berg, J.S., Li, Z., Wang, Y., Lang, P., Sousa, A.D., Bhaskar, A., Cheney, R.E., and Stromblad, S. (2004). Myosin-X provides a motor-based link between integrins and the cytoskeleton. Nature cell biology *6*, 523-531.

Zhao, B., Wu, Z., and Muller, U. (2016). Murine Fam65b forms ring-like structures at the base of stereocilia critical for mechanosensory hair cell function. eLife *5*.

Zhao, Y., Yamoah, E.N., and Gillespie, P.G. (1996). Regeneration of broken tip links and restoration of mechanical transduction in hair cells. Proceedings of the National Academy of Sciences of the United States of America *93*, 15469-15474.

Zhu, X.J., Wang, C.Z., Dai, P.G., Xie, Y., Song, N.N., Liu, Y., Du, Q.S., Mei, L., Ding, Y.Q., and Xiong, W.C. (2007). Myosin X regulates netrin receptors and functions in axonal path-finding. Nature cell biology *9*, 184-192.